Design and Locomotion Studies of a Miniature Centipede-Inspired Robot

Design and Locomotion Studies of a Miniature Centipede-Inspired Robot

A dissertation presented

by

Katie Lynn Hoffman

to

The School of Engineering and Applied Sciences

in partial fulfillment of the requirements

for the degree of

Doctor of Philosophy

in the subject of

Engineering Sciences

Harvard University

Cambridge, Massachusetts

May 2013

Dissertation Advisor:
Professor Robert J. Wood

Author:
Katie Lynn Hoffman

Design and Locomotion Studies of a Miniature Centipede-Inspired Robot

Abstract

Many applications, such as search and rescue missions, hazardous environment exploration, and surveillance, call for miniature robots capable of agile locomotion in a variety of unpredictable environments. Recent advances in meso-scale fabrication techniques and an understanding of biological insect locomotion have enabled the creation of multiple miniature legged robots to meet this demand. Nearly all insect-scale legged robots take inspiration from rigid-body hexapods; however, another unique body morphology found in nature is that of the centipede, characterized by its many legs and flexible body. These characteristics are expected to offer performance benefits in terms of agility, stability, robustness, and adaptability.

This thesis presents the design of a millirobot with many legs and a passively flexible backbone, both novel qualities for a robot at this scale. A modular hybrid-dynamic model of the horizontal plane motion effectively predicts locomotion trends on flat terrain and provides guidance in choosing design parameters for centipede-inspired millirobots. This millirobot demonstrates the use of body undulations similar to those of its biological counterpart, which are shown to enhance straight-line locomotion by increasing speed. These undulations arise passively, reducing the number of required actuators and simplifying control. A turning strategy is developed to enable

an n-segment millirobot to perform a variety of maneuvers with only two independent drive signals. An experimental robustness study illustrates graceful degradation of locomotion performance, as opposed to immediate failure, in the presence of appendage damage, demonstrating an advantage to a many-legged design. Finally, the passively flexible body and many legs are shown to provide increased ground contact and stability when traversing obstacles, resulting in faster speeds over rough terrain compared to similar millirobots with rigid bodies and/or only six legs. These results suggest this millirobot design could result in improved performance for miniature legged robots as well as provide insight into biological locomotion at small scales.

Contents

Acknowledgments

I'd like to thank my advisor, Prof. Rob Wood, for giving me immense freedom in my research, creating a collaborative and fun work environment, and providing excellent guidance over the course of this work. I'd also like to thank him for always having something encouraging to say even on those days that it seemed like nothing was working and, of course, for reading all of my paper drafts, most of which were at least a couple of pages over the limit.

I'd like to acknowledge my committee members, Prof. Robert Howe and Prof. Andrew Biewener, for their diverse and insightful comments regarding the content of this thesis. Thanks also to Prof. Radhika Nagpal for her guidance on a semester-long research project and continuous feedback on my work as well as Prof. Keith Buffinton and Prof. Charles Knisely for their advice and encouragement throughout the years beginning back in my days at Bucknell.

Thank you to my parents, John and Carla, siblings, Maggie and Eston, and the countless other family members that have been supportive during this process. My niece Hayley's excitement for the robots presented in this thesis has been much appreciated, and I hope her enthusiasm for robots never fades. Despite her inability to read, I'd like to thank my energetic boxer, Daisy, for being overly excited to see me on my numerous trips to PA. I'd also like to thank my best friend, Danielle Mattern, for always answering my phone calls, even when she was fully aware it would result in an hour-long discussion about my latest grad school-related crisis. Of which there were a few.

Some of the most rewarding parts of this experience have been the opportunity to work with dedicated and enthusiastic researchers and the friendships I've formed with

the former and current members of the Harvard Microrobotics Lab. I'd like to thank all of the members and alumni of the Harvard Microrobotics Lab and specifically mention Dr. Ben Finio, Dr. Peter Whitney, Dr. Pratheev Sreetheran, and Dr. Andy Baisch for their own contributions to meso-scale fabrication and robotics and their friendship over the past five years. Thanks to Mike Smith and his ability to fix anything and Hetchen Ehrenfeld for helping with many purchasing and travel arrangements.

Thank you to the National Science Foundation Graduate Research Fellowship Program and the National Defense Science and Engineering Graduate Fellowship program for funding this work.

Finally, this thesis would not be complete without thanking the centipede that wandered into my apartment one afternoon almost four years ago, unknowingly serving as the inspiration for much of this work.

Chapter 1

Motivation

Many applications call for distributed networks of small robots capable of working together to assist humans in dangerous or otherwise impossible tasks, such as identifying survivor locations in search and rescue missions, exploring hazardous environments, and surveillance. Miniature robots are necessary to accomplish these tasks, as many situations require robots to navigate small spaces or go unnoticed during reconnaissance. They must be inexpensive as swarms consist of many robots and employ efficient gaits to reduce weight of power and control electronics. The operating conditions require these robots to traverse a variety of terrain, implying legged designs may be appropriate for these applications.

In addition to being used for the above listed applications, miniature legged robots also have the potential to provide insight into biological locomotion at small scales. The robots could be used to explain the diversity of body morphologies in nature, different gaits used by biological creatures, and parameter values and muscle placement as they relate to efficient locomotion.

1.1 Miniature ambulatory robots

Advances in meso-scale fabrication techniques [65], [62] and an improved understanding of the locomotory mechanisms of insects [27] have enabled recent success in the development of miniature ambulatory robots. Most of these weigh on the order of 15-25 grams [32], [8] or 1.5-2.5 grams [7], [33] and are modeled after rigid body hexapods (namely cockroaches), utilize the alternating tripod gait seen in insects, and have a central body that houses electronics and actuators with six comparably massless legs.

1.2 Centipede locomotion

While cockroach-inspired millirobots have been successful at demonstrating fast, stable locomotion, the diversity of creatures found in nature leaves open questions about ambulation at small scales. An alternative to a rigid body and six legs is the body morphology of the centipede, a predatory arthropod characterized by their many legs and very flexible bodies. This unique body morphology suggests advantages over robots with rigid bodies and fewer legs in the following areas:

1. **Agility:** The inherent body flexibility allows centipedes to display remarkable agility traversing obstacles by conforming to surfaces.

2. **Stability:** The many legs of centipedes (up to 191 pairs in some species [21]) give this creature added stability on flat and rough terrain by providing increased ground contact points, while the elongated bodies allow for a wide trapezoid of stability.

3. **Robustness:** In nature it is common for small creatures to experience damage in the form of leg loss. With significant mechanical redundancy in the form of legs, centipedes are thought to be capable of sustained locomotion even in the face of severe appendage injuries.

4. **Adaptability:** The modular nature of a centipede body suggests a centipede-inspired robot could be adaptable to different situations, such as adding more legs when a mission calls for increased payload capacity for sensors. Additionally, centipedes can simultaneously using different legs for various tasks. Documentaries have shown some centipedes (*Scolopendra gigantea*) are capable of suspending their bodies from the ceiling of caves with their rear legs and, with their front legs, catching flying mammals of similar size (which they subsequently devour) [6].

These are all very useful characteristics that until now have been largely unexplored at small scales.

In addition to exhibiting multiple benefits over rigid body hexapods, a centipede-inspired millirobot also has the potential to answer underlying questions regarding centipede locomotion, specifically those pertaining to the effectiveness of body undulations. In the 1950's, Manton concluded that the body undulations, or waves that travel along the body of a centipede, are passive and detrimental to locomotion based on kinematic observations [45]. More recent work involving electromyograms attached to the lateral flexor muscles of centipedes found that muscles actively promote body undulations, thereby possibly increasing step size during straight-line locomotion [4]. Understanding undulatory locomotion could ultimately provide insight into efficient

methods of introducing flexibility into robot bodies.

1.3 Centipede robots

While there are currently no other known centipede-inspired millirobots, multiple macro-scale robots (i.e. mass on the order of kg and body length of approximately 1 m) have taken inspiration from myriapods. Most of these feature bodies with rotational joints between segments, actively controlled by motors, including the Nereisbot prototype (10 cm/module length and 0.27 kg/module) [55], a Centipede robot (10 cm/module length) [34], and the Legged CkBot (6 cm/module length and 0.138 kg/module) [53]. More recently, a centipede robot with flexible shafts between segments has demonstrated locomotion over a variety of obstacles (6.5 cm/module length and 0.11 kg/module) [38]. Due to the use of flexures and linear actuators for devices at small scales, the design of locomotory mechanisms and interconnections between segments differs from these larger-scale devices.

1.4 Dynamic modeling

Dynamic models of segmented robots are also very rare. It is often straightforward to model the dynamics of individual segments, but fairly challenging to accurately describe the interactions between segments and with the environment. On the insect-scale, the dynamics for robots with relatively rigid bodies and massless legs, similar to cockroaches, have been modeled. Videos and force data from actual cockroaches have been used to create a dynamic model of cockroach locomotion which can be

extended to similar cockroach-style millirobots to predict their motion and provide a design guide [31]. Unfortunately, this model does not encompass locomotion of millirobots with flexible, segmented bodies. The dynamics of larger segmented robots, such as a centipede robot [34], [46] and a segmented, legged robot demonstrating different directly actuated undulatory modes [55], and controllers for these robots were studied. Simulations were also performed to find an optimal number of legs for larger segmented robots [49]. These dynamic models do not accurately describe locomotion of millirobots due to scaling effects and actuation and fabrication differences. To properly answer questions associated with locomotion and design of segmented ambulatory millirobots, a dynamic model is necessary.

1.5 Contributions and thesis outline

The research presented here has contributed to the goal of developing millirobots for swarm robotics applications and understanding many-legged locomotion at small scales as illustrated by the following highlights and organized into the chapters of this thesis:

• **Chapter 2 (Design): Designed and fabricated myriapod millirobots with passively flexible bodies to use as a platform for studying terrestrial locomotion at small scales:** Most centipede robots, which only exist at larger scales, generally feature motors between segments to create body undulations similar to centipedes; however, at the millimeter scale, adding additional actuation can increase fabrication time and power consumption. This led to the design of a novel robot

with passive springs between segments rather than motors. The robot is composed of repeating segments, each with two legs driven by piezoelectric actuators and an external power supply and controller. The robot is fabricated using PC-MEMS, a layered manufacturing process featuring laser-machined rigid composites and flexible polymers as links and flexure joints, respectively [62].

• **Chapter 3 (Dynamic modeling): Formulated hybrid-dynamic model to describe motion of centipede millirobot:** To choose design parameters for this robot and determine the best gaits for straight-line locomotion, a hybrid-dynamic model was created that is successful at predicting trends in locomotion for an under-actuated robot with many legs.

• **Chapter 4 (Parameter studies): Showed how design parameters affect centipede millirobot locomotion at small scales**: The dynamic model was used to study the effect of design parameters on locomotion, specifically showing how back-bone stiffness affects speed of locomotion and stability while also choosing segment parameters to achieve efficient locomotion within a range of driving frequencies.

• **Chapter 5 (Straight-line locomotion): Discovered body morphology and drive signals that enhance speed during straight-line locomotion:** The long, flexible bodies of centipedes lead to undulations, or waves that travel along the length of the body. Experiments and simulation demonstrate that even with a passive body and underactuated design, choosing an appropriate phase for the drive signals causes

body undulations that increase step size and, therefore, the speed of the robot. Additionally, the best gaits for this centipede millirobot are very similar to those present in actual centipedes, providing insight into biology.

• **Chapter 6 (Turning): Developed a turning strategy for underactuated millirobots with any number of legs:** A locomotion strategy was formulated that allows the robot to perform many maneuvers with only two independent drive signals and contralaterally coupled legs, which is important for computationally-limited millirobots.

• **Chapter 7 (Robustness): Demonstrated graceful degradation of locomotion performance due to leg failures:** While performing tasks in hazardous environments, legged robots encounter situations where damage may be incurred, particularly to appendages. This work suggests that many-legged robots have the ability to maintain the capacity to walk even in the presence of leg failures. It is demonstrated that robots with nominally 10 legs or more are still able to walk even with a significant percentage of legs missing, how the location of missing legs affects performance, and conditions under which the gait must be altered to account for missing legs.

• **Chapter 8 (Obstacle traversal): Implemented design improvements to facilitate locomotion over obstacles and characterized payload capacity:** Due to their small size, legged millirobots are expected to climb over obstacles similar in

size to their body height. Additionally, swarm robotics applications typically feature hazardous, obstacle-ridden environments. Preliminary results comparing the performance of 6-leg and 12-leg millirobots suggest having more ground contact points and a flexible body assists with obstacle traversal and stability. Claws were developed to increase the height of obstacles this robot is capable of traversing. This robot is also able to carry an additional 123 percent of its body weight, which is important for future integration of onboard electronics.

Chapter 2

Design

The goal of this work was to create a millimeter scale robot with a centipede body morphology to answer questions regarding myriapod locomotion at small scales. In order to achieve this goal, an initial conceptual body morphology and mechanism design was iterated into a compact, easy-to-manufacture millirobot displaying locomotion not unlike that of its biological counterpart.

The notional design for this millirobot has a modular nature, consisting of repeated segments, each with two legs, connected by a deformable backbone. Two main characteristics, body flexibility and number of legs, are what distinguish this millirobot from others at this scale, which are generally modeled after cockroaches with rigid bodies and only six legs [32], [8], [33], [7] or four legs [39]. Having no central rigid body to ground mechanical components and actuation requires novel designs to create coordinated leg motion that results in net millirobot locomotion. While most larger centipede-inspired robots feature active joints between segments, such as DC motors to control body deformation [55], [34], [53], the design presented here focuses

on passive joints between segments with the only active components controlling the hip joints. This eliminates the need for additional actuation between segments, which can be costly in terms of energy and fabrication time.

Over the course of this project, there have been multiple designs, with the significant differences between each being in segment functionality and backbone structure. This process has involved multiple iterations, with design choices based on observations made during modeling and experimentation. While the initial design merely had two main features of centipede body morphology, i.e. a flexible body and many legs, the final millirobot resulted into a design similar in morphology to centipedes, which typically have repeating, two-legged segments, low-inertia legs, muscles at the distal 'hip' joint to create leg motion, feedback between segments running along both sides of the body, segments sitting lower than hip joints, and a foot that pivots relative to the ground [45]. Rather than merely mimicking the body morphology of a centipede, an iterative process of design improvements was used to create a compact, dynamically efficient, stable, and robust millirobot capable of locomotion up to 20 cm/s and the ability to traverse obstacles up to half its body height. As the final design was used for the experiments presented in this thesis, details on previous designs can be found in [19] and [30], and references are made to these designs throughout this chapter to justify decisions regarding body morphology.

The millirobots used throughout this thesis have varying numbers of segments, ranging from 3 through 10 segments, or 6 through 20 legs. The lower limit was determined by the minimum number of segments to maintain static stability with contralateral leg coupling, while the upper end of the range was based on both man-

ufacturing challenges and drive signal limitations. This range of millirobot lengths enabled trends dependent on the number of legs to be successfully studied.

The milirobots described here do not have on-board electronics and are controlled and powered by an external xPC target system (Mathworks) and high voltage amplifier. The experiments described in subsequent chapters use waveforms alternating between 0 and 200 V, albeit current on the order of mA, for stance and swing control. For autonomous locomotion, future work should focus on onboard electronics similar to those presented in [37] and [7]; however, it was possible to study locomotion techniques at this scale using a tether of minimal weight to reduce interference with locomotion.

2.1 General body morphology

The design for a centipede millirobot began with an overall general body morphology and horizontal plane motion analysis before focusing on the individual mechanisms used to create this motion. The mechanical diagrams illustrating the body morphology in the horizontal plane for each of the millirobot designs are shown in Fig. 2.1. As the locomotion strategy focuses on the horizontal plane motion, the stance DOF is not included in the description. This is considered to be a binary input, with each design capable of switching stance by instantaneously removing the pin joint from the current stance foot and pining the current swing foot. As can be seen in Fig. 2.1, each of the designs feature repeating segments connected by passive joints.

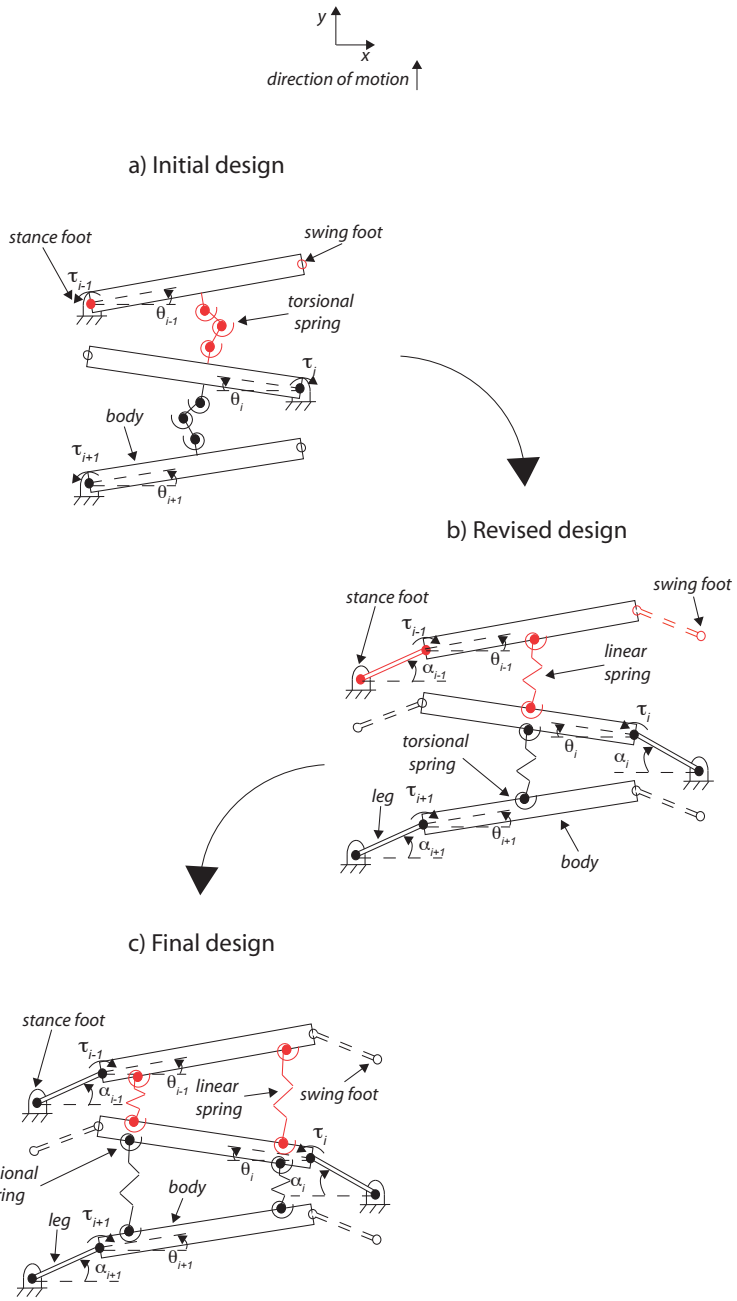

Figure 2.1: Diagrams of horizontal plane motion for a) initial design [19] ©2010 IEEE, b) revised design [30], and c) final design with changes between designs highlighted in red [2] ©2012 IEEE.

2.1.1 Initial design

The initial locomotion strategy required each segment to function as the legs of the millirobot (Fig. 2.1(a)). Each segment would rotate relative to the stance foot located at the distal end of the segment. Upon completion of the rotational motion, the stance foot is lifted from the surface while the swing foot is being placed on the ground. The process is then repeated with the segment rotating in the opposite direction. Adjacent segments are connected by three passive joints, created using rotational flexures. Considering the passive intersegmental flexures and the pivot point for each segment as pin joints and using Gruebler's equation shows that having three flexures between segments gives each segment one independent DOF in the horizontal plane. By having each segment input be a torque applied at the stance foot pivot point, the number of DOF matched the number of inputs in the horizontal plane.

As noted, the passively flexible backbone for the initial design is composed of only rotational flexures. Not only does this design have a singularity in the uncompressed state, but it also causes the body compression and segment rotation to be highly coupled. With this body morphology, the mass is concentrated in the segments, which, as can be seen in Fig. 2.1(a), causes the step size to be fully dependent on the amount of segment rotation. Having significant segment rotation to provide a reasonable leg swing as the millirobot moves forward increases energy consumption. For many of the larger-scale centipede robots, the body rotation and leg swing angle are also equivalent as the legs are rigidly attached to the segments [55], [34], [53]. This design also required the stance foot to adhere to the ground while the segment

rotated with respect to it, which was found to be impractical on many surfaces used in experiments.

2.1.2 Revised design

To improve the overall body morphology, the design was revised to solve the issues of efficiency and backbone singularities (Fig. 2.1(b)). In this design, massless legs were added to each segment. A segment has one actuated DOF in the horizontal plane, a torque input at the shoulder joint, and one actuated DOF in the vertical plane, which allows legs to be lifted and placed on the ground. It differs from the previous design in that an additional DOF in the horizontal plane is passive and allows the foot to pivot with respect to the ground as can be seen by comparing Fig. 2.1(b) with the previous representation (Fig. 2.1(a)). Rather than having segments, which contain most of the system mass, experience the same amount of rotation as the legs as in the initial design, massless legs are added to produce forward locomotion. While the segments do rotate as the backbone compresses and extends, the rotation is less than that in the initial design as the segments are not the only component contributing to step size. This additional passive DOF causes the design to be underactuated, requiring a dynamic model to fully describe the motion. Another notable improvement is the backbone design which features two torsional springs surrounding a linear spring between each segment (Fig. 2.1(b)). Replacing a rotational joint with a linear joint eliminates the backbone singularity and allows the segment rotation and body compression to be further decoupled.

The revised body morphology was a significant improvement over the previous

design in that it removed the backbone singularity, allowing the backbone to compress and extend and segments to initiate motion simultaneously. The massless legs improved locomotion efficiency and eliminated the need for adhesives to prevent the feet from slipping; however, the underactuated nature of the design requires the passively compliant backbone to provide sufficient feedback between segments to not only prevent adjacent segments from colliding but also potentially cause segment rotation that will enhance locomotion. Having the backbone situated along the center of mass (COM) of each segment only allows the springs to apply restoring forces as opposed to moments about the COM as segments move relative to one another.

2.1.3 Final design

The only difference between the revised design and final design in terms of body morphology is in splitting the backbone into two sections that run along the length of the body as shown in Fig. 2.1(c). This gives the millirobot the same two DOF per segment in the horizontal plane, but allows the backbone to apply larger moments about the segment COM due to the increased distance of the joint attachment points from the segment COM compared to the revised design (Fig. 2.1(b)).

As will be shown in Chapter 5, this body morphology was capable of producing locomotion enhancing undulations very similar to actual centipedes. The springs running along both sides of the body can be compared to the lateral flexor muscles that run along the body of actual centipedes, curving the body as the centipede locomotes. While the body morphology presented here features passive springs rather than active muscles, as the segments move relative to one another, the springs produce forces

that curve the body in ways similar to the muscles in actual centipedes. Additionally, the torque applied at the hip joints and the massless legs are also similar to actual centipedes, which have most of their mass concentrated in the center of the body. While based purely on design choices to improve locomotion, the body morphology of this millirobot ended up being very similar to actual centipedes, allowing this work to provide insights into biological locomotion.

2.2 Mechanism design

Upon formulating a conceptual design of the body morphology and locomotion strategies for the millirobot, the individual mechanisms necessary to create this motion were designed. A rendering of the design of the final version of the millirobot used throughout this work is shown in Fig. 2.2. The design takes into consideration the overall body morphology, which requires swing and stance motion of the leg at the hip joint (2 DOF) as well as backbone connections created using linear and rotational springs. Again, the design process was iterative; however, the focus here is on the final millirobot design used in the experiments presented in this thesis. The two earlier versions of this millirobot are presented in [19], [30]. The millirobots shown in Fig. 2.3 have segment masses of 220 mg and measure 4 cm by 1 cm by 1.2 cm. A detailed description of how design parameters were chosen for this millirobot is presented in Chapter 4.

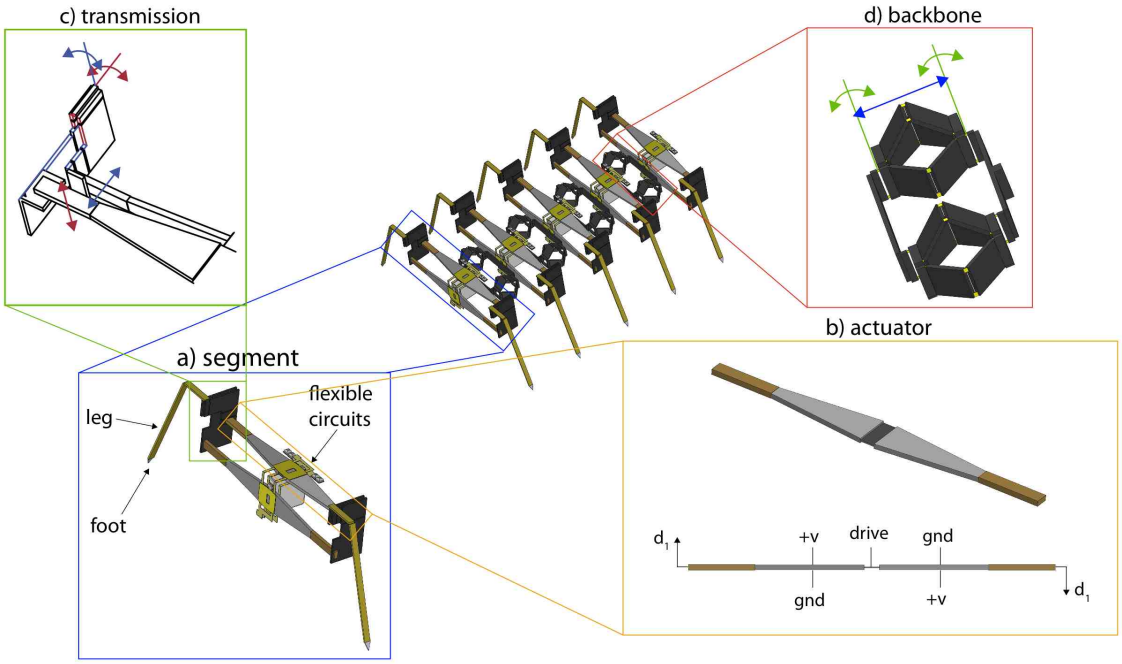

Figure 2.2: Final design of centipede millirobot illustrating detail of a) segment, b) actuators, c) transmission, and d) backbone [2] ©2012 IEEE.

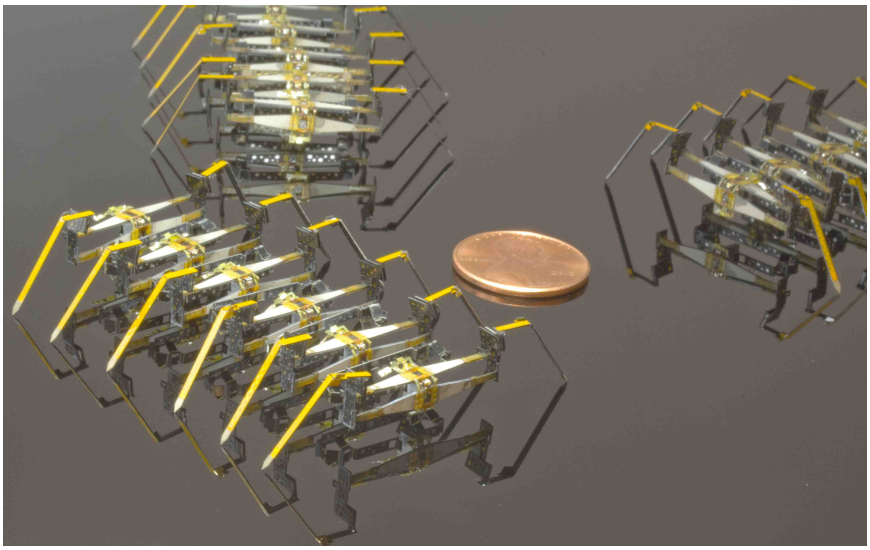

Figure 2.3: Centipede millirobots of varying lengths used for the studies presented in this thesis [2] ©2012 IEEE.

2.2.1 Segment design

A single segment has two legs, each capable of lift and swing (Fig. 2.2(a)). The legs are angled outward to facilitate lifting and feature pointed feet to promote rotation of the feet with respect to ground, consistent with the overall body morphology presented in Sec. 2.1.

Actuation

Piezoelectric actuation was chosen for this millirobot due to the high bandwidth (hundreds to thousands of Hertz), high energy density [67], and easy integration with the PC-MEMS fabrication process. Piezoelectric actuation has previously shown potential for locomotion at this scale in walking [43], [51] and flying robots [64], [23]. Additional motors were considered for this robot. DC motors at small scales tend to have very low power densities due to their use of rotating components which suffer from the enhanced deleterious effects of friction at this scale. Even one of the smallest DC motors weighs 0.46 grams and is 4 mm in diameter (Didel MK04S-10) which is approximately twice as large as the mass of an individual segment for this millirobot. Shape memory alloy (SMA) actuators have a lower bandwidth than piezoelectric actuators (on the order of 1-5 Hz, compared to kHz for piezoelectric actuators), which would limit the stepping frequency of the millirobot.

Actuation of the stance and swing motions of the leg are achieved by two dual piezoelectric bimorph cantilever actuators oriented perpendicular to one another. The piezoelectric actuators each provide a linear displacement at the distal end. The actuator placed parallel to the horizontal plane provides stance control, while the

actuator situated perpendicular to the horizontal plane rotates the segment about the stance foot. The two sides of each piezoelectric bimorph share a drive signal and are oppositely poled. A diagram illustrating wiring and tip deflections of an actuator is provided in Fig. 2.2(b). This allows for contralateral coupling of legs such that when one leg is being lifted, the opposite is being placed on the ground. Similarly, when one actuator is pushing the robot forward, the opposite is resetting the swing foot in preparation for the next step. This simplifies the design by reducing the number of drive signals necessary to control each segment to two, but produces challenges when attempting to introduce asymmetries into the gait to achieve turning. The two actuators are grounded to a central mount, which is attached to adjacent segments via the flexible backbone components described in Sec. 2.2.2.

Transmission

The mechanical and structural components are flexure-based mechanisms. Pin joints and other rotational components created by macroscale processes are inefficient at small scales, as losses due to friction dominate due to increased surface area, A, relative to volume, V, ($A \alpha L^2$, $V \alpha L^3$). Using flexures as joints relies on material deformation rather than purely sliding rotational joints to reduce losses due to friction.

As a method of amplifying the actuator tip deflection and producing a rotational output at the hip joint, the distal ends of each dual cantilever actuator are attached to four-bar mechanisms oriented orthogonally. This compact transmission design is illustrated in Fig. 2.2(c). For each four-bar mechanism, the adjacent piezoelectric actuator acts as the mechanical ground since the actuators are stiff to bending about

an axis perpendicular to their face. This transmission allows both the stance and swing actuators to be mounted centrally within each segment, reducing segment inertia, and, more importantly, minimizing the mass of the legs, which experience the largest amount of motion.

2.2.2 Backbone

The goal of the backbone is to provide each segment with sufficient degrees of freedom to have an independent drive signal but still allow dynamic feedback between adjacent segments. The backbone is completely passive and composed of combinations of flexures that act as springs. An individual intersegmental connection is shown in Fig. 2.4(a).

Each connection has a linear joint (Sarrus linkage) sandwiched between two rotational joints (individual flexures) situated along the length of the body. This series of three joints is mirrored on both sides of the body to allow the motion of adjacent segments to provide restoring moments about the segment COM as segments rotate relative to one another. The Sarrus linkage is fabricated in a pre-compressed state to allow both body extension and compression. An actual backbone is shown in Fig. 2.4(b-d) undeformed, compressed, and rotated, respectively. The backbone was designed to allow relative motion between each segment in the horizontal plane but be resistant to off-axis rotations that might result in decreased leg lifting height. The off-axis compliance that allows bending along the length of the body will be shown to be beneficial in maintaining foot contact when traversing obstacles in Chapter 8.

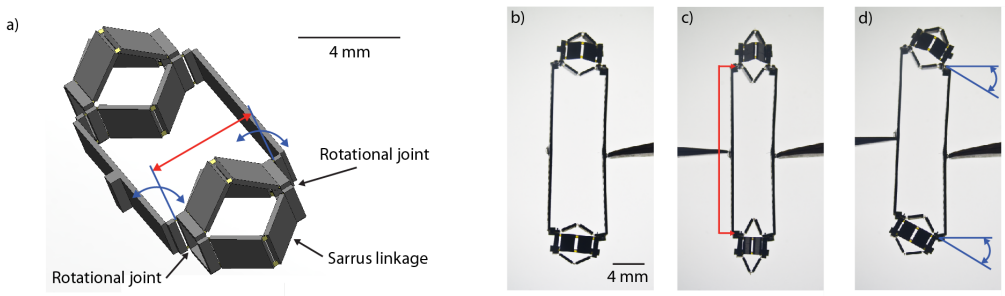

Figure 2.4: a) Rendering of an intersegmental connection illustrating passive linear and rotational joints and a top view of an actual backbone b) undeformed, c) compressed, and d) rotated [1] ©2011 IEEE.

2.3 Fabrication

The PC-MEMS (printed-circuit micro-electro-mechanical systems) process [62] was used to fabricate the robot designs presented here. This process was created to fill the gap between microscale fabrication using MEMS techniques and macroscale machining (for example, lathes, mills, injection molding, casting, etc.). While MEMS processes can create features on the micron scale, they are limited in the materials that can be incorporated into devices and work best for creating quasi-two-dimensional structures that exhibit planar motion, requiring many challenging manual steps to be taken to form three-dimensional components. Macroscale machining involves piecing together many different components and cannot create detailed features with the resolution required for millimeter scale devices (on the order of tens of microns).

The PC-MEMS process involves laser-micromachining rigid composites (namely 0/90/0 carbon fiber), flexible polyimide (Kapton), and sheet adhesives (Dupont FR1500) and bonding these layers together using heat and pressure. Precision pin alignment of the layers reduces the need for skilled labor. A final outline cut with a

laser releases the quasi-two-dimensional components.

The following sections will not describe the PC-MEMS fabrication process in detail as this is covered extensively in [62], but rather will focus on practices implemented to make the fabrication of this specific millirobot feasible and contributions this work has made to the fabrication of millirobots, including interlocking tabs and pin aligned internal circuitry. Since this millirobot has many repeating components, it was necessary to use batch fabrication techniques that allow many of the same components to be made in parallel. While the pop-up fabrication of a flapping wing microrobot has been demonstrated with only one DOF input [59], the fabrication techniques here focused on decreasing manual alignment, individual wires, and number of skilled folds. As the design was constantly changing throughout this work, and it was desirable to swap out individual components without replacing entire segments (i.e. changing transmission and backbone stiffness, leg shape, etc.), techniques were implemented to ease fabrication, but stopped short of transforming this robot design into a one step/segment process. This should certainly be a focus of future work, and would require solving the problem of integrating flexible circuits into the pop-up process and improving software to facilitate the design process.

2.3.1 Interlocking tabs

While most of the folds on this millirobot are right angles, the legs are angled outward at 20 degrees to facilitate lifting. A contribution of this work to fabrication techniques is the use of interlocking tabs to lock folds in place and form precision angles. By placing tab and slot features on components that are designed to be

a press fit, as illustrated for the leg of this millirobot in Fig. 2.5, not only are the components folded at a precise angle, but they are also locked in place while adhesives are applied.

a) interlcoking tabs technique

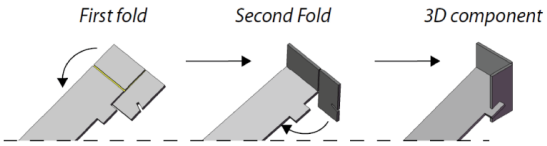

b) flat and folded legs

Figure 2.5: a) Interlocking tabs used to facilitate folding components and b) unfolded (center) and folded millirobot legs

2.3.2 Circuitry

An initial version of this millirobot required individual wires to connect each ground, bias, and drive signal to an external power supply [19]. As soldering to the thin electrodes on the piezo material or central carbon fiber elastic layer is not feasible, conductive epoxy was applied to connect 51 gauge wires (22 μm diameter) to each piezo plate (10 wires per segment). Thin, lightweight wires had to be used to avoid interference with the motion of the millirobot. The connections were often unreliable, wires were subject to breaking, and the process was time-consuming and frustrating. For millirobots with only one or two piezoelectric bimorph actuators, manual wiring is not a major concern, but realistically, had this fabrication step not been improved, this millirobot would not exist.

As the stance actuators for each hip joint share a single drive signal connected to

the central elastic layer, a single central elastic layer was laminated with four piezo plates to create an actuator with two coupled cantilever bimorphs (Fig. 2.6(b)). This eliminated the need to create four individual actuators for each segment and reduced the amount of internal circuitry.

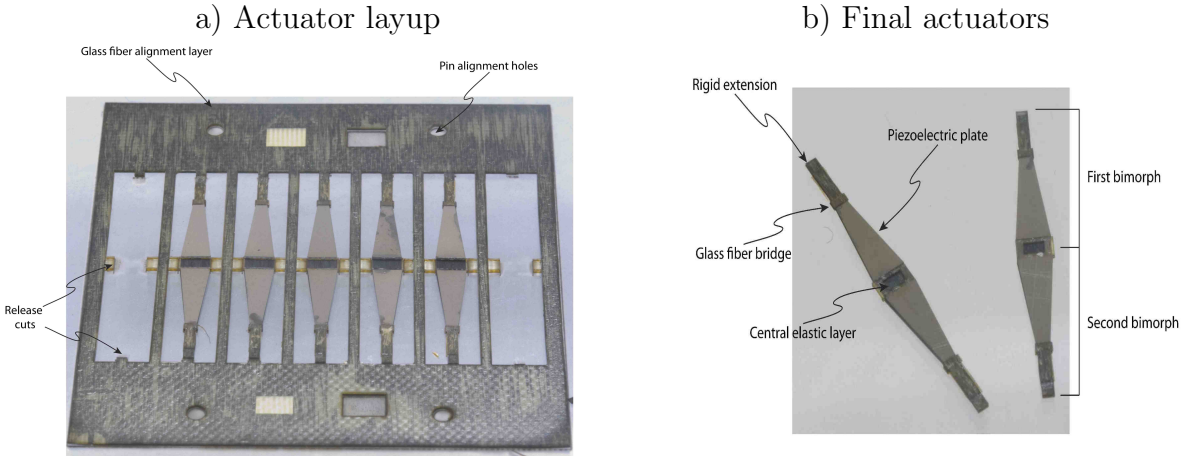

Figure 2.6: a) Layup used to create piezoelectric bimorphs. The end actuators have ben removed to show laser cuts to release actuators from mold. b) Actuators used for this millirobot.

A modified lithography process, which uses ablation via laser-machining rather than exposure and development, was used to create flexible circuits out of copper-clad polyimide. For each segment, a ground, high voltage bias, and two drive signals are needed. To reduce the number of external wires for each segment to only four/segment, the internal circuitry connects each of the four ground and four bias signals within the segment. To do this, two flexible circuits are used for each segment (Fig. 2.7). One circuit lies on the backside of the actuators, connecting the two drive signals to the elastic layer and the ground and bias signals for the rear piezo plates. This circuit also contains bond pads to solder the external wires. A second flexible circuit lies on top of the actuators to connect the ground and bias signals for the front

piezo plates. Both circuits contain bond pads to connect the ground and bias signals from the front and rear circuits.

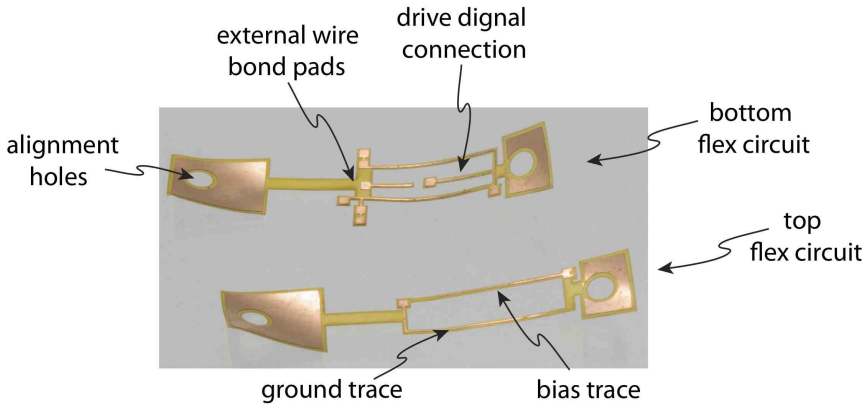

Figure 2.7: Top and bottom flexible internal segment circuitry.

To wire the circuits to the external power supply, the ground and bias signals for each segment are wired to those of the adjacent segment. For each millirobot, $2n + 2$ wires (where n is the number of segments) are used to connect the millirobot to the external power supply. 51 gauge wires were used, and the wires were twisted into a bundle to reduce interference with locomotion. While internal wiring of individual segments was improved significantly by introducing flexible circuits, future work to eliminate the manual wiring of ground and bias signals between adjacent segments could involve integrating flexible circuits into the backbone pieces to connect the circuits of each individual segment.

2.3.3 Segments

To connect the mount, actuators, and flexible circuits without requiring manual alignment, molds were created using a combination of laser-machined layers of a tacky substrate (Gelpak). This process is described in Fig. 2.8. Each of the mold layers and

flexible circuits are pin aligned, and individual components are placed into the molds. Glass-fiber prepreg and heat and pressure applied during curing bond the actuators to the mount and the flex circuits to the actuators, which rely on a physical contact for electrical conductivity. Upon release from the mold, six 90 degree folds complete the segment. The transmissions, which each have one fold facilitated by castellated flexures and an aluminum layer for holding the fold in place while an adhesive is applied, are press fit onto the ends of the actuators.

2.4 Conclusion

The millirobot design presented here and its similarity to the body morphology of its biological counterpart make it possible to demonstrate and study multiple aspects of centipede locomotion as will be shown in subsequent chapters, including passive undulatory gaits (Chapter 5), simple turning strategies (Chapter 6), robustness to leg failures (Chapter 7), and obstacle traversal (Chapter 8). The modular nature of this design allows each of these studies to encompass trends due to variation in leg number.

The PC-MEMS process was adapted to allow for the batch fabrication and precision alignment of the millirobot components. Future work should focus on a one-step assembly process via pop-up fabrication techniques.

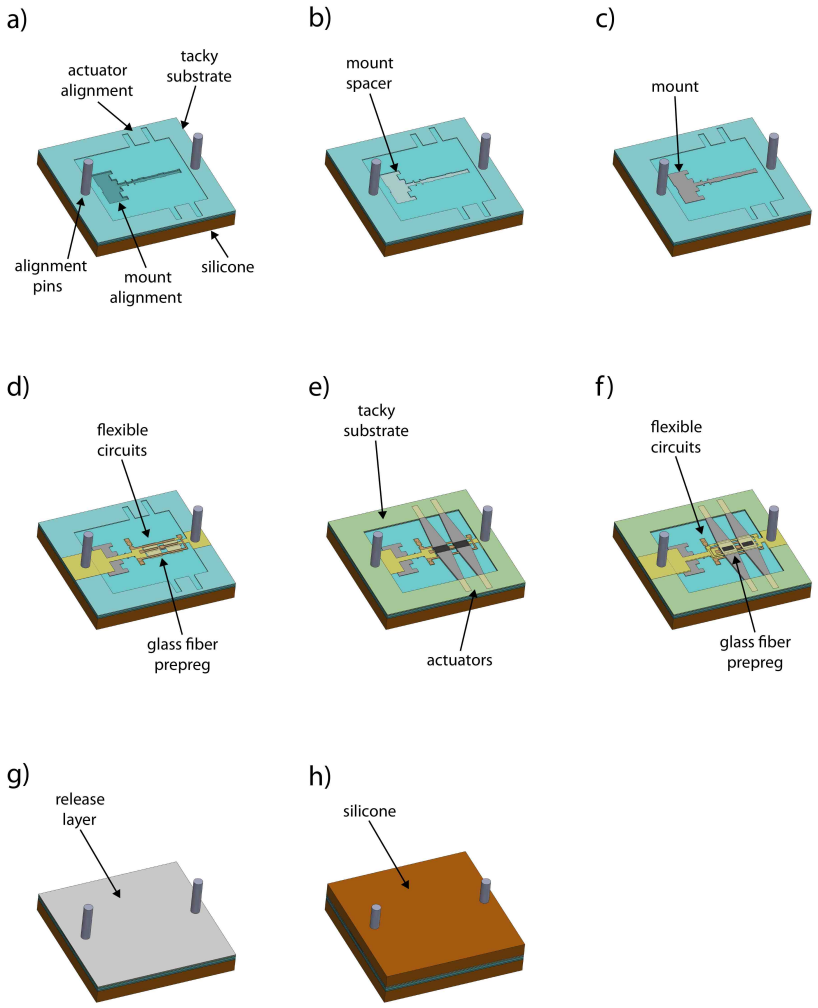

Figure 2.8: Fabrication process for segments: a) Silicone and three layers of a tacky substrate are pin aligned. The layers of tacky substrate have features for actuator and mount alignment. b) A spacer is added to elevate the mount. This combination of layers allows all components to lay flat. c) The mount to which the actuators are grounded is dropped into place. d) Two pieces of glass fiber prepreg (which bond the actuators to the mount and the flexible circuits to the actuators) are placed, and the bottom flexible circuit is pin aligned. e) An additional layer of tacky substrate is added, and the actuators are dropped into place. f) The top flexible circuits are pin aligned, and the pieces of glass fiber prepreg are added to bond the circuits to the actuators. g) A teflon release layer is added. h) The top silicone layer is added for even pressure distribution.

Chapter 3

Dynamic modeling

To study myriapod robot locomotion at small scales by determining fast and efficient gaits and choosing design parameters for this millirobot, a hybrid-dynamic model of the horizontal plane motion was created. Due to the millirobot being underactuated, with an additional passive DOF per segment in the horizontal plane, a kinematic model is insufficient to describe the motion of this millirobot. While dynamic models of insect-scale creatures with rigid bodies and flexible legs have been studied extensively [8], [35], [61], [31], [27], [26], [9] and used to create efficient and fast robots at multiple scales [8], [14], [52], there are no known models to describe the motion of many-legged robots with passively flexible bodies at this scale. It is expected that a model for a miniature centipede-inspired robot will similarly enhance the design of flexible-body, many-legged robots while also providing insight into biological centipede locomotion.

Modeling an underactuated, segmented robot presents its own challenges in that the interactions between segments must be accurately described to predict the overall

millirobot locomotion, particularly due to the underactuated nature of the millirobot which relies on the intersegmental connections to provide feedback between segments. It must also be performed in a modular way to easily encompass millirobots with any number of segments. The result of this effort was a model of the horizontal plane motion of a centipede millirobot able to accurately predict trends in locomotion on flat terrain as shown in Chapter 5.

3.1 Assumptions

A number of assumptions were made during the formulation of this model:

1. There is no coupling between the stance and swing motion. The stance and swing motion of the leg is created by two orthogonal four-bar transmissions. Due to the small amount of leg rotation (approximately +/- 14 degrees for the chosen parameters), there is assumed to be no coupling between the stance and swing motion, and the stance is determined by a binary input.

2. The feet are pin joints with respect to ground. Foot ground interactions are challenging to predict and depend on the surface on which the robot is walking. Here, it was assumed that locomotion would take place on solid, flat terrain as opposed to granular media. It was also assumed that the coefficient of friction would be sufficient to prevent feet from slipping laterally, while still allowing the feet to rotate with respect to ground. To facilitate this, the feet used in these experiments featured a sharp tip to allow pivoting on a single point. Note that if foot friction prevented the feet from rotating with respect to ground, the

torque applied at the hip joint of the millirobot would cause the millirobot to move in the opposite direction. This is an artifact of the underactuated nature of the millirobot.

3. The legs and backbone are massless. The majority of the segment mass is concentrated in the actuators, which are located in the central body of the segment. The legs (seven percent of total weight) and backbone (eight percent of total weight) individually comprise very little of the segment mass. This also means the resetting of the swing leg in preparation for the next step has no effect on body rotation.

4. Stance change is inelastic and instantaneous. While the millirobot dynamics are continuous throughout one step, transitions during stance change need to be modeled as the stance changes and the swing leg becomes constrained by a pin joint. Stance change is controlled with a trapezoidal wave with steep slew rate (10 kV/s), causing the stance to change in 2 ms for the 200 V drive signal used in the experiments presented here. Most of the studies are performed at low frequencies (1-15 Hz). At the higher limit of frequencies, this assumption begins to break down as stance change can comprise up to 40 percent of the total step. The implications of this will be discussed when comparing the simulation and experimental results in Chapter 5.

5. Flexure damping is negligible compared to actuator damping. Experiments by Steltz [60] for similar flexure-based mechanisms showed flexure damping is small compared to the actuator damping.

6. Transmission flexure bending energy is negligible. As the mechanical joints are composed of flexures rather than pin joints, millirobot motion results in storage of elastic energy in the flexures. The transmission flexures are in parallel with the actuator, assuming only one DOF per four-bar transmission (i.e. no flexure buckling). The effective hip joint stiffness results from the addition of the actuator stiffness and transmission joint stiffness, making the significantly smaller transmission joint energy negligible (actuator energy storage of 10^{-6} J vs. transmission energy flexure storage of 10^{-8} J/flexure).

Additional minor assumptions are mentioned throughout this chapter.

3.2 Individual segment dynamics

Each four-bar hip joint is controlled by a piezoelectric bimorph actuator as described in Chapter 2. Extensive modeling of piezoelectric bending actuators performed previously by Wood [67], [66] was used to calculate the actuator blocked force, F_a, and tip deflection, δ_a as a function of material properties (piezo coupling coefficient, densities, material thicknesses, etc.) and trapezoidal actuator geometry (width, length, and width and length ratios). The actuators can be modeled as a force source in parallel with a spring and damper (Fig. 3.1) with an actuator spring constant of

$$k_a = \frac{F_a}{\delta_a} \tag{3.1}$$

The actuator damping coefficient, b_a, is based on heat losses due to material deformation using equations from [66]. The actuator kinetic energy, which can be modeled

as a cantilevered mass on a rod, is assumed to be negligible compared to the kinetic energy of the segment during locomotion, particularly when mapped through the four-bar transmission.

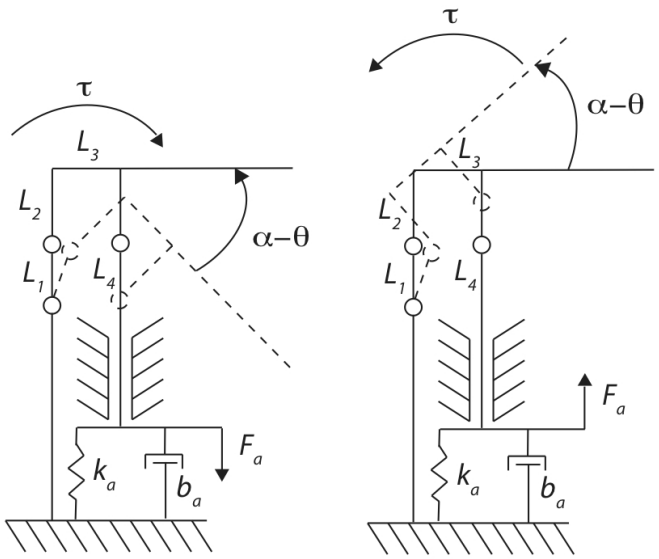

Figure 3.1: Diagram showing how actuator force is mapped to a torque using a four-bar mechanism. Dotted lines indicate rotation of four-bar mechanism [30].

The linear actuator input is translated into a rotational output at the hip joint through the four-bar transmission. To map the actuator force, stiffness, and damping through the transmission, a linearized transmission ratio was used based on an analysis in [64] and the small hip rotation (approximately +/- 14 degrees for the chosen parameters). The linearized transmission ratio, T_h, is the inverse of the length of the third link, L_3, of the four-bar mechanism as illustrated in Fig. 3.1. This gives a hip torque of

$$\tau = \frac{F_a}{T_h} \tag{3.2}$$

3.3 Backbone modeling

The backbones main function is to provide feedback between segments and is composed of four rotational joints and two linear joints. The rotational joints are single flexures, with an associated spring constant calculated using bending beam theory

$$k_t = \frac{E_f t_f^3 w_f}{12 L_f} \tag{3.3}$$

where E_f is the modulus of elasticity, and t_f, w_f, and L_f are the flexure thickness, width, and length, respectively.

The linear backbone springs are sarrus linakges composed of a series of flexures oriented such that they only allow 1 DOF linear motion. While the rotational flexures can be modeled as bending beams with great accuracy, this model breaks down for the large deformations experienced by the sarrus linkage flexures. To allow both extension and compression of the backbone while avoiding singularities, the flexures were initially deformed to an angle of 45 degrees. Given the complexity of the device, a finite element (FE) model was created to calculate an effective stiffness for the sarrus linkage. The model was created such that sarrus linkage parameters (Fig. 3.2(a)) can easily be altered. An example case for the model is shown in Fig. 3.2(b), taking a force input on one face of the sarrus linkage while the opposite end remains grounded. The output is the deflection of the sarrus linkage, which can be used to calculate the stiffness, k_l. Additional studies were performed to reduce off-axis rotation by applying out-of-plane forces to the sarrus linkage.

Over large deflections, the sarrus linkage force-deflection curve is nonlinear, with

a) Parameterization

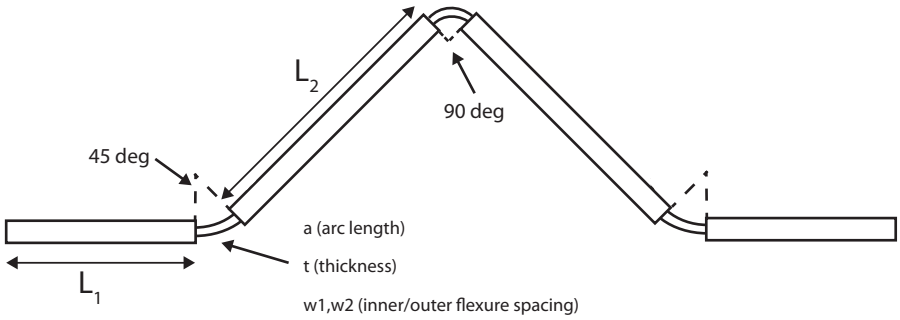

b) FEM model

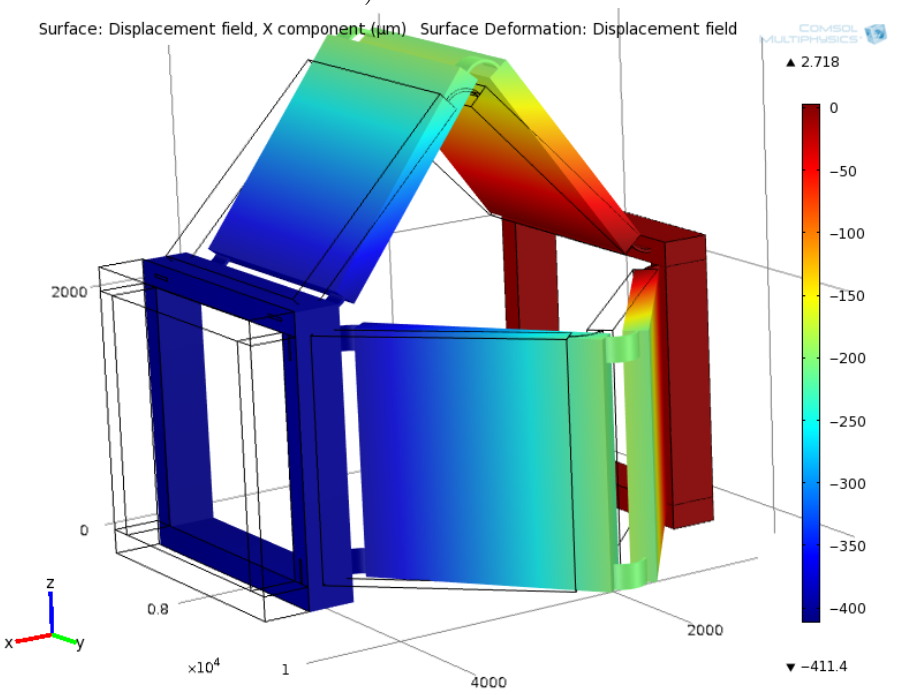

Figure 3.2: Finite element model for sarrus linkage including a) flexure parameterization and b) an example showing sarrus linkage deflection due to applied force.

the joint becoming stiffer for large deflections; however, a zoomed in view of the curve shows linearity over small deflections. For this model, the sarrus linkage was assumed to have a linear spring constant as anticipated deflections only ranged from 0 to 500 microns. The FE model results were compared to a sarrus linkage manufactured using the SCM process and tested by applying forces (using weights and gravity) and measuring deflection. These results are shown in Fig. 3.3. The model predicted a larger spring constant than what was found experimentally; however, it was found to agree to the same order of magnitude. This was taken into account when specifying flexure geometries.

3.4 Hybrid-dynamic model

Upon formulating models describing the individual segment and backbone dynamics, a multi-DOF hybrid-dynamic model was created for the millirobot. Due to the modular nature of the robot, the dynamics can also be written in a modular fashion, facilitating studies involving robots with any number of segments, n.

A physical description of the model is shown in Fig. 3.4. Segment i has two independent DOF in the horizontal plane. The leg is free to rotate relative to ground by an angle α_i, and the body can rotate an angle θ_i, both with respect to an axis perpendicular to the direction of motion. Having only one control input in the horizontal plane, but two degrees of freedom per segment makes this robot underactuated. The state variables for each segment are the leg and body rotations as well as the leg and body angular velocities

$$[\theta_i, \alpha_i, \dot{\theta}_i, \dot{\alpha}_i] \tag{3.4}$$

a) FEM prediction

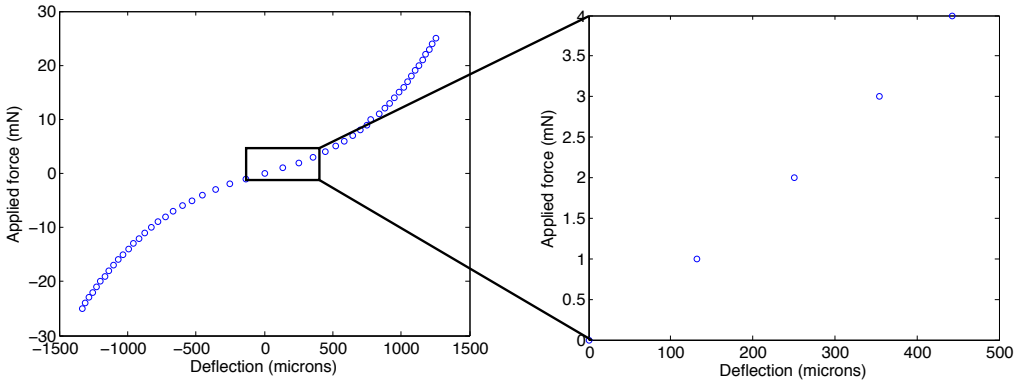

b) Results for small deflections

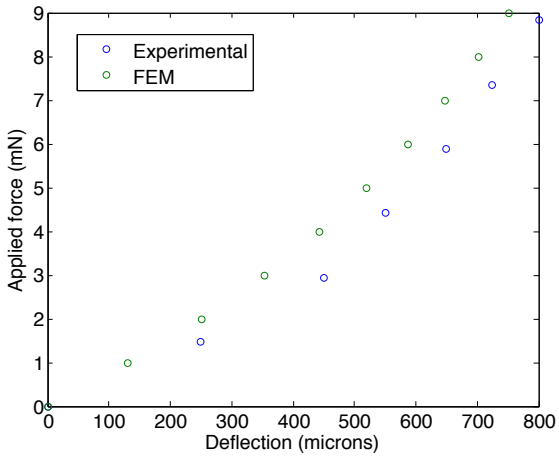

Figure 3.3: Results from sarrus linkage modeling showing a) deformation as a function of applied force with a zoomed-in view illustrating linearity over small deformations and b) finite element predictions compared to experimentally measured stiffness.

There are $4n$ state variables for an n segment millirobot.

Important geometric parameters include the leg length, L_{leg}, body width, w_b, measured as half the distance between hip joints, body length in the direction of motion, L_b, and equilibrium length of the Sarrus linkage, l_{eq}. The kinematics of each segment, or the position of every point on the robot, can be written in terms of the state variables, α_i and θ_i, and the current position of the stance foot, $(x_{f,i}, y_{f,i})$. The center of mass of a segment can be described in terms of the body parameters and state variables as

$$x_i = x_{f,i} + c_{f,i} L_{leg} \cos\alpha_i + c_{f,i} w_b \cos\theta_i \tag{3.5}$$

$$y_i = y_{f,i} + L_{leg} \sin\alpha_i + w_b \sin\theta_i \tag{3.6}$$

where $c_{f,i} \in [-1, 1]$ is a binary input variable indicating whether the left or right foot is the current stance foot. The complete kinematic equations are not shown here for brevity, but are included in the full dynamics derivation in Appendix A.

The mass of each segment, m, is concentrated in the body as the actuators constitute the majority of the mass, and the legs are assumed to be massless and rigid. The total kinetic energy is given according to

$$K = \frac{1}{2} \sum_{i=1}^{n} I_{cm} \dot{\theta_i}^2 + m(\dot{x_i}^2 + \dot{y_i}^2) \tag{3.7}$$

where I_{cm} is the moment of inertia about the center of mass, assuming mass is evenly distributed along the length of the segment. $\dot{x_i}$ and $\dot{y_i}$ are the velocities of the center of mass, which can be written in terms of the state variables using the kinematics of

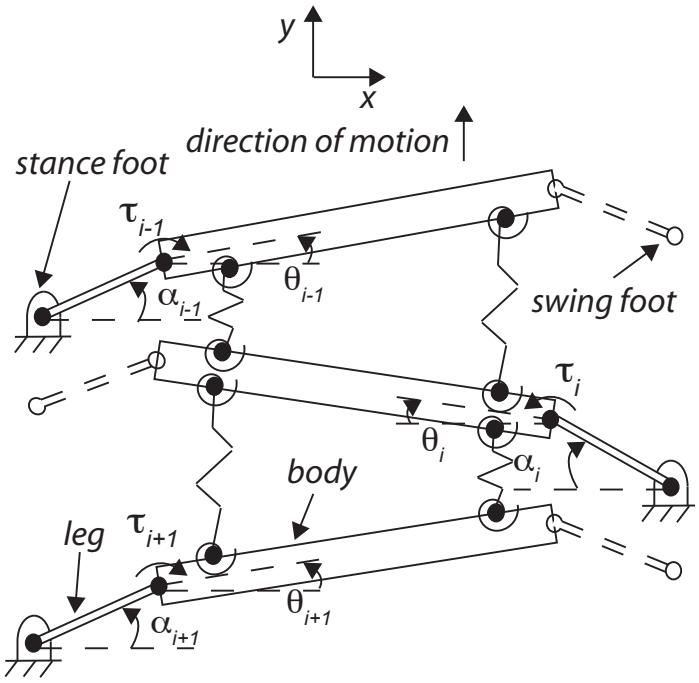

Figure 3.4: Depiction of horizontal plane motion of a three segment millirobot [1] ©2011 IEEE.

the system as

$$\dot{x_i} = -c_{f,i}\dot{\alpha_i}L_{leg}\sin\alpha_i - c_{f,i}\dot{\theta_i}w_b\sin\theta_i \tag{3.8}$$

$$\dot{y_i} = \dot{\alpha_i}L_{leg}\cos\alpha_i + \dot{\theta_i}w_b\cos\theta_i \tag{3.9}$$

The potential energy for the system includes that stored in the backbone rotational flexures and Sarrus linkages as well as that of the piezoelectric actuator. This is calculated as follows:

$$\begin{aligned} P = \quad & \frac{1}{2}\sum_{i=1}^{n-1}\left(k_l(\Delta {l_{ac,i}}^2 + \Delta {l_{bd,i}}^2) + k_t(\gamma_{a,i}^2 + \gamma_{b,i}^2 + \gamma_{c,i}^2 + \gamma_{d,i}^2)\right) \\ & + \frac{1}{2}\sum_{i=1}^{n} k_a \frac{1}{T_h^2}(\alpha_i - \theta_i)^2 \end{aligned} \tag{3.10}$$

where k_l is the linear spring constant for the Sarrus linkage, k_t is the torsional spring constant of the backbone rotational joints, $\Delta l_{ac,i}$ and $\Delta l_{bd,i}$ are the Sarrus linkage deflections, and $\gamma_{a,i}$, $\gamma_{b,i}$, $\gamma_{c,i}$, and $\gamma_{d,i}$ are the rotations of the backbone torsional springs. The deflections and rotations for each portion of the backbone can be written in terms of the state variables of each adjacent segment using the kinematics of the robot (Appendix A). The actuator stiffness, k_a, is mapped through the four-bar transmission with transmission ratio T_h.

Finally, the work transfer with the environment can be characterized by the torque input from the actuators, τ_i (actuator force mapped through the four-bar transmission) and the losses due to actuator damping as described by

$$W = \sum_{i=1}^{n} \tau_i(\alpha_i - \theta_i) - b_a \frac{1}{T_h^2}(\alpha_i - \theta_i)(\dot{\alpha}_i - \dot{\theta}_i) \tag{3.11}$$

where b_a is the actuator damping constant.

To illustrate that each of the energy terms included here are significant, Fig. 3.5 shows the system energy for the alternating gait for a 10 segment millirobot walking at 5 Hz. For this particular case, the backbone rotational and linear spring energy is less than the kinetic and actuator potential energy; however, it still accounts for up to 15 percent of the energy during portions of the step. The ratio of backbone spring potential energy to total energy varies for different gaits.

The Euler-Lagrange method and these energy terms were used to formulate the equations of motion for an n-segment millirobot. The Lagrangian used to describe

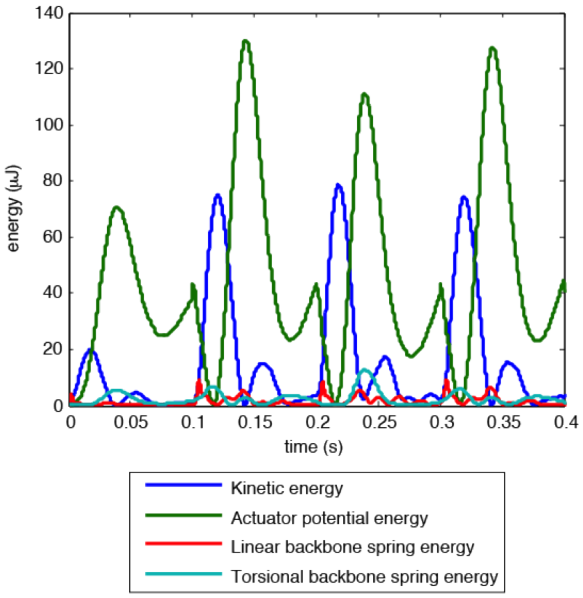

Figure 3.5: System kinetic energy, actuator potential energy, and linear and rotational backbone potential energy for a 10 segment millirobot using the alternating gait at 5 hz. Stance changes occur every 0.1 seconds.

the system is as follows

$$\begin{aligned} L = \quad & \sum_{i=1}^{n} \Big(\frac{1}{2}(I_{cm} + mw_b^2)\dot{\theta_i}^2 + \frac{1}{2}mL_{leg,i}^2\dot{\alpha_i}^2 + mw_bL_{leg,i}\dot{\alpha_i}\dot{\theta_i}\cos(\theta_i - \alpha_i) \\ & -\frac{1}{2}k_a\frac{1}{T_h^2}(\alpha_i - \theta_i)^2\Big) - \frac{1}{2}\sum_{i=1}^{n-1}\Big(k_l(\Delta {l_{ac,i}}^2 + \Delta {l_{bd,i}}^2) \\ & +k_t(\gamma_{a,i}^2 + \gamma_{b,i}^2 + \gamma_{c,i}^2 + \gamma_{d,i}^2)\Big) \end{aligned} \tag{3.12}$$

The first, second, and third terms are the kinetic energy, the fourth term is the actuator potential energy, while the last two terms are the backbone linear and rotational spring energy, respectively. To obtain the equations of motion, partial derivatives of the Lagrangian and work transfer were taken with respect to each of the state variables. This process was painful at best and illustrated in Appendix A. The results of

this effort were highly coupled, nonlinear equations for $\ddot{\theta}_i$ and $\ddot{\alpha}_i$ of the form

$$\begin{bmatrix} \dot{\theta}_i \\ \dot{\alpha}_i \\ \ddot{\theta}_i \\ \ddot{\alpha}_i \end{bmatrix} = A \begin{bmatrix} \theta_i \\ \alpha_i \\ \dot{\theta}_i \\ \dot{\alpha}_i \end{bmatrix} + b\tau_i \tag{3.13}$$

where A is a 4x4 matrix and b is a 1x4 vector and both are nonlinear functions of θ_{i-1}, α_{i-1}, θ_i, α_i, θ_{i+1}, and α_{i+1} and their derivatives. The full dynamic equations and derivation are given in Appendix A. The equations take a modular form to easily describe the dynamics for any number of segments. The equations for the first and last segments have less terms due to the lack of spring forces acting on the front and rear of the millirobot.

The coupling between the dynamic equations stems from the fact that the backbone compression, which results in elastic energy storage, is dependent on the state variables of the two surrounding segments. This coupling is critical in that it results in forces that provide feedback between segments to produce stable locomotion.

3.5 Stance changes

The model is hybrid-dynamic due to stance changes. While the equations presented above are continuous over the course of one step, the stance change introduces a pin joint constraint on the new stance foot, causing an instantaneous and inelastic collision. This was modeled for each individual segment using a method presented in [15] for a vertical-plane walker with knee joints. While kinetic energy is not conserved

during inelastic collisions, angular momentum is conserved about the new stance foot for the leg and segment system and hip joint for the segment alone. This is because the only external forces acting on the leg and segment system are the reaction forces due to pinning the new stance foot. Similarly, the only external forces acting on the segment alone are between the leg and segment at the hip joint. The goal was to use the final state variable values from the previous step ($\theta_{i,fin}$, $\alpha_{i,fin}$, $\dot{\theta}_{i,fin}$, $\dot{\alpha}_{i,fin}$) to calculate the initial conditions for the next step ($\theta_{i,init}$, $\alpha_{i,init}$, $\dot{\theta}_{i,init}$, $\dot{\alpha}_{i,init}$) using conservation of angular momentum about the new foot joint and hip joint. As a result of the kinematic convention chosen,

$$\theta_{i,init} = -\theta_{i,fin} \tag{3.14}$$

and, based on the coupling between the stance and swing legs and the assumption that the legs are massless,

$$\alpha_{i,init} = -(\theta_{i,fin} - \beta) \tag{3.15}$$

where β is the touchdown angle of the leg calculated by the transmission ratio and unloaded actuator deflection at the time of stance change. These values can also be used to calculate the new stance foot position.

Conserving angular momentum about the new foot pivot point gives

$$\begin{aligned} &\frac{1}{3}w_b^2\dot{\theta}_{i,fin} + (x_i - x_{f,i})\dot{y}_{i,fin} + (y_i - y_{f,i})\dot{x}_{i,fin} \\ &= \frac{1}{3}w_b^2\dot{\theta}_{i,init} + (x_i - x_{f,i})\dot{y}_{i,init} + (y_i - y_{f,i})\dot{x}_{i,init} \end{aligned} \tag{3.16}$$

while conserving angular momentum about the new hip joint results in

$$\begin{aligned}&\frac{1}{3}w_b^2\dot{\theta}_{i,fin} + (x_i - x_{s,i})\dot{y}_{i,fin} + (y_i - y_{s,i})\dot{x}_{i,fin} \\ &= \frac{1}{3}w_b^2\dot{\theta}_{i,init} + (x_i - x_{s,i})\dot{y}_{i,init} + (y_i - y_{s,i})\dot{x}_{i,init}\end{aligned} \tag{3.17}$$

where $(x_{s,i},\, y_{s,i})$ is the shoulder joint position. Both equations can both be solved for the initial body and leg velocities for the next step $(\dot{\theta}_{i,init},\, \dot{\alpha}_{i,init})$. The equations are included in Appendix A.

It should be noted that the leg touchdown angle β can vary based on the drive signal voltage at the time of stance change. In most techniques used here, the drive signal is either at ground or the maximum bias voltage at the time of stance change, and the actuator is fully deflected. The choice of coupled drive signals simplifies the design, but as can be seen in these equations, the leg touchdown angle is dependent on the voltage applied at the time of stance change, which also affects the torque being applied to the hip joint of the previous stance foot. This complicates the issue of introducing asymmetries into the gait to achieve turning, which is addressed in Chapter 6.

3.6 Simulation

Using Matlab, a simulation was created describing the motion of the robot. The complexity of the coupled, nonlinear equations required the use of a numerical differential equation solver (ode45). The hybrid dynamic nature of the robot allows for the simulation to solve the derived equations over single steps, while calculating

transitions between steps using the conservation of momentum equations provided in Sec. 3.5. The robot parameters, which will be discussed further in Chapter 4, as well as the drive signal are the inputs to the system. The modular nature of the differential equations also allow the number of segments to be altered by merely changing a single number in the simulation, making this perfect for studying millirobots with any number of segments. Outputs from the simulation include a full representation of the horizontal plane motion of the millirobot, energy values, a cost of transport and average speed estimate, and additional performance metrics used in evaluating the millirobot.

3.7 Initial results

As an initial confirmation of the ability of this model to accurately predict the locomotion of the millirobot, a version of this model with a slightly modified backbone configuration (i.e. one sarrus linkage and two rotational joints vs. two sarrus linkages and four rotational joints between each segment) was compared to experimental results of a three segment millirobot in terms of segment and leg rotation. As can be seen in Fig. 3.6, these results agreed well. Additional use of the model presented here will be shown in Chapters 4 and 5.

3.8 Conclusion

The horizontal plane dynamic model presented here was used to determine appropriate design parameters (Chapter 4) and was critical in predicting important

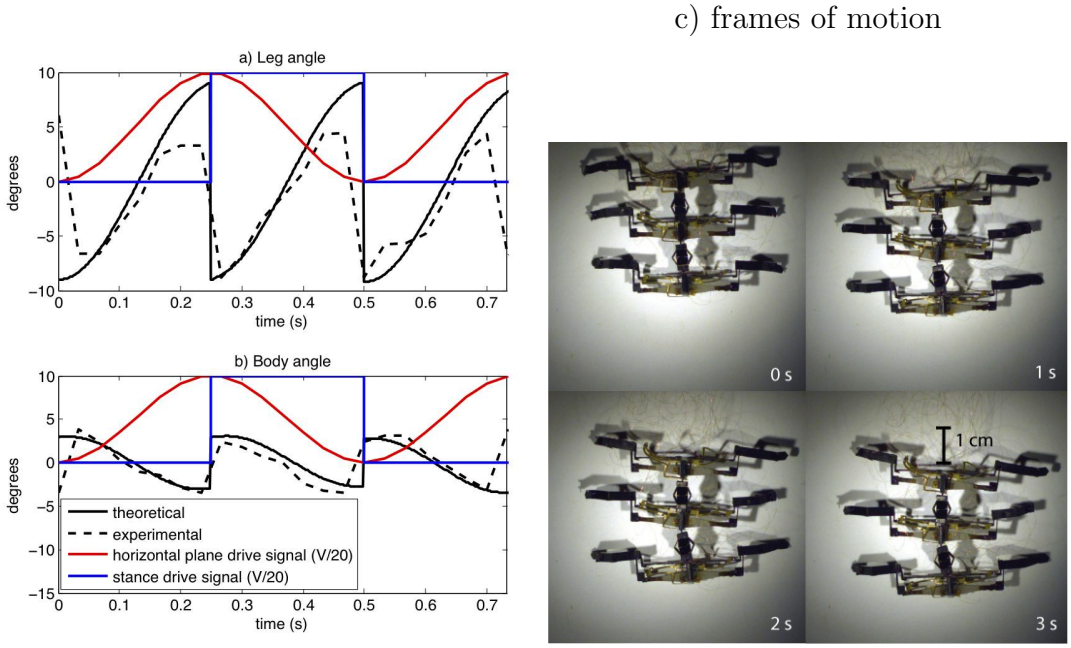

Figure 3.6: Theoretical and experimental a) leg and b) body angles for middle segment of three-segment robot plotted with simulation drive signals for three steps. c) Frames of motion of three-segment centipede millirobot [30].

trends in straight-line locomotion, specifically the presence of passive body undulations (Chapter 5).

This model does have some limitations. At high frequencies (i.e. above 15 Hz), the feet experience increased slipping. While two additional DOF could be added to the model to account for this, the millirobot was found to perform best in frequencies less than 15 Hz, thus minimizing the effect of feet slipping. Additionally, foot/ground interactions vary with surfaces and are difficult to predict. The stance change is also not perfectly instantaneous, causing slight losses in leg swing angle. Describing this would require a full 3D model, which could also be useful in analyzing the dynamic effects in the transverse plane observed in Chapter 8. This is proposed for future work as the horizontal plane model was sufficient for the studies performed in this thesis.

Despite these limitations, the horizontal plane model proved capable of providing important insight into trends in centipede millirobot locomotion as will be evidenced by the undulatory gait studies described in Chapter 5.

Chapter 4

Parameter studies

While centipedes found in nature share the common characteristics of long, flexible bodies and many legs, they each exhibit different degrees of body flexibility, leg lengths, masses, and muscle forces which result in varying speeds of locomotion, severity of undulations, and agility. Centipedes can have anywhere between 15 and 191 leg pairs with body lengths between 4 and 300 mm [21]. Some centipedes, such as the common house centipede *Scutegira*, have multiple fused segments and long thin legs, allowing them to run at speeds up to 40 cm/s in very open spaces, while *Scolopendromorph* and *Lithobiomorph* centipedes, with long flexible bodies and short legs, can rapidly navigate small spaces and uneven terrain [44].

To understand myriapod locomotion at small scales and choose design parameters for this millirobot, a systematic study was performed. There are numerous ways to choose design parameters for this millirobot. The method presented here is broken into two categories: segment design and backbone design. Segment parameters were chosen based on desired size and operating frequency range. Then, using the best gait

for straight-line locomotion (as will be described in Chapter 5), backbone parameters were varied individually in simulation for millirobots with 3 through 15 segments for a range of frequencies (1, 5, 10, and 15 Hz). They were evaluated based on speed of locomotion.

I will not claim that this is a fully comprehensive study of design parameters, nor that the optimal parameters for this millirobot were used for locomotion; however, parameters that resulted in stable, efficient locomotion were found. Additionally, this study gave valuable insight into locomotion of many-legged robots with flexible bodies. While the parameter studies and gait studies (i.e. determining drive signal waveforms and phases) were performed simultaneously, the end result was such that for the range of body parameters studied, there were similar trends among the different gaits tested. Given this, the discussion of body parameters that follows is presented using the drive signals found for the best straight-line gaits presented in Chapter 5.

The overall goal of this thesis is to study locomotion at small scales and create a centipede-inspired millirobot capable of agile locomotion for use in swarm robotics applications. To achieve this goal, the size of each segment was limited to approximately 1 cm by 1 cm by 4 cm; however, the method and trends presented here can be applied to robots of various sizes with a similar body morphology.

The body parameters used for many of the simulations and experiments in this thesis are shown in Tab. 4.1 and illustrated in Fig. 4.1. It is important to recognize the coupling between many of the parameters. For example, the body width, w_b, has to be greater or equal to the actuator length. Decreasing w_b decreases the maximum actuator length, which, in turn, decreases the actuator stiffness, k_a. Additionally,

Table 4.1: Centipede Millirobot parameters

Leg length, L_{leg}	10 mm
Body length, L_b	4 mm
Body width, w_b	10 mm
Sarrus linkage attachment, w_{sa}	7 mm
Sarrus linkage length, l_{eq}	6 mm
Transmission ratio, T_h	2.5 rad/mm
Actuator stiffness, k_a	860 N/m
Sarrus linkage stiffness, k_l	29 N/m
Backbone flexure stiffness, k_t	10 $\mu Nm/rad$
Maximum torque, $\tau_{i,max}$	34.5 μNm
Actuator damping, b_a	6.3 Ns/m
Segment mass, m	220 mg
Segment inertia, I_{cm}	7.3×10^{-3} mgm^2

changing the body length, L_b, changes the maximum actuator width, hip torque, τ, and k_a.

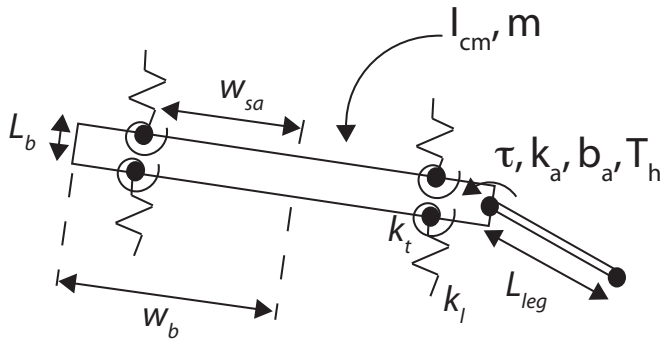

Figure 4.1: Illustration of a single segment with body parameters labeled.

4.1 Segment parameters

4.1.1 Swing control

A kinematic model was used to choose initial actuator and transmission parameters to serve as a starting point. The desired actuator output is blocked force, F_a, and unloaded deflection, δ_a. Mapping δ_a through the transmission to kinematically find the maximum leg swing angle gives a good indication of the step size for cases where there is no body rotation. Negative or positive body rotation will decrease or increase the step size, respectively, since the segment rotation at the time of stance change also affects step size of this underactuated robot. Given the desire to keep the robot small, to avoid collisions between legs, the maximum step size must be less than half the segment length ($L_b + l_{eq}$). This assumes opposite stance feet of adjacent segments and no segment rotation. The segment length was chosen to be 1 cm, specifying a desired kinematic leg deflection of 5 mm. For these reasons, δ_a was chosen to be 100 microns, and with a transmission ratio, T_h, of $\frac{1}{400}\frac{rad}{\mu m}$, results in a maximum hip deflection of 14 degrees. With a leg length, L_{leg}, of 1 cm, chosen based on size considerations, this gives a kinematic step size of 5 mm, ignoring dynamic effects and body rotation. T_h was chosen to amplify the actuator deflection while decreasing hip torque.

To determine F_a, which is linearly proportional to τ based on T_h, a simplified frequency response was taken into consideration. Simplifying the problem to only look at the segment dynamics, a frequency analysis was performed on the hip joint to determine k_a that would result in a hip natural frequency, f_h, of between 10-15

Hz. A range of 10-15 Hz was chosen based on experimental observations that above 15 Hz, the millirobot feet begin to slip significantly. The hip natural frequency is important to the millirobot driving frequency, as this gives an approximation of when to switch the stance to achieve maximum leg rotation. As will be seen in Chapter 5, this is a very good representation for the alternating gait but varies for other phases. For the alternating gait, driving the robot at frequencies lower than the hip natural frequency will cause the segment to oscillate, while driving at higher frequencies will cause the stance to change before the leg reaches maximum rotation. The hip natural frequency can be calculated using k_a ($\frac{F_b}{\delta_a}$), and actuator damping coefficient, b_a, both mapped through the transmissions

$$\frac{1}{2\pi T_h}\sqrt{\frac{k_a}{I}}\sqrt{1-\left(\frac{b_a}{2T_h\sqrt{k_a I}}\right)^2} \tag{4.1}$$

where I is the segment inertia about the hip joint found using I_{cm} and the parallel axis theorem. As I is dependent on the actuator mass and w_b, which is related to k_a and b_a, this was an iterative process. For the parameters chosen, the hip natural frequency is approximately 11 Hz.

F_a and δ_a, along with maximum electric field and mechanical strain constraints, were used to directly determine the actuator parameters, including the length, width, length and width ratios [67], while holding material thicknesses constant due to constraints on commercially available materials. A Matlab script written by Whitney [63] provided the optimal actuator parameters for F_a and δ_a by minimizing actuator

energy density

$$E = \frac{\delta_a F_b}{m_a} \tag{4.2}$$

where m_a is the actuator mass.

4.1.2 Stance control

In addition to the coupling of the body parameters that affect locomotion in the horizontal plane, there is also coupling with those that affect the vertical plane motion. The stance actuators have to apply enough force to hold the body off the ground while providing sufficient deflection to lift the legs. The amount of force needed to lift the body depends heavily on the mass of the segment, which is primarily dependent on both the stance and swing actuators. The lift height of the foot and stance torque applied at the hip joint are also affected by the leg length, as a longer leg will result in more lift but also require more hip torque due to an increased moment about the hip joint. This shows that the leg length and actuator mass affect both the horizontal and vertical plane motion. The leg lifting height can be estimated kinematically based on the free deflection of the actuator mapped through the four-bar transmission coupled with the leg length. It is important to note that this is only an estimate and the actual leg lifting height also depends on the mass of the millirobot and the amount of force output of the stance actuators, which determines the ability to keep the body suspended above the ground.

While many of the parameters were chosen using the horizontal plane model presented in Chapter 3, the parameters affecting stance were determined experimentally. This mainly included finding flexure widths, lengths, and thicknesses to prevent buck-

ling of the transmission joints under the weight of the millirobot. An initial transmission stiffness was chosen and increased during subsequent iterations of this millirobot, eventually resulting in values that allowed it to support up to 123 percent of its body weight while lifting its legs up to 6 mm with no payload (Chapter 8). The version of this robot used in Chapters 7 and 8 also has a central elastic layer for the stance actuators twice the thickness of the swing actuator (i.e. two layers of carbon fiber), to increase the actuator force output albeit marginally decreasing the actuator deflection.

4.2 Backbone parameters

There are multiple geometric and stiffness parameters associated with backbone; however, it was found that the parameters having the largest effect on locomotion performance (i.e. speed) are the torsional flexure stiffness, k_t, the sarrus linkage stiffness, k_l, and the lateral distance of the sarrus linkage attachment point from the segment COM, w_{sa}. These are illustrated in Fig. 4.1. Each of these parameters was varied individually, and the results of this effort were intuitively pleasing.

4.2.1 Backbone stiffness

It is important to recognize that the main function of the backbone in the horizontal plane is to provide sufficient dynamic feedback between segments. This means the backbone should be compliant enough to allow relative motion between segments, but not too compliant such that adjacent segments collide during locomotion. While straight-line locomotion and segment phasing will be discussed in depth in Chapter 5,

it is necessary to point out the effect of the optimal undulatory gaits which were used here. The undulatory gaits, or a phase of $\phi = \frac{2\pi}{n-1}$ radians between segments, increase step size during locomotion due to the positive segment rotation.

Fig. 4.2(a-b) shows that increasing the torsional joint stiffness, k_t, and the linear joint stiffness, k_l, individually reduces the speed for millirobots with varying numbers of segments over a range of frequencies. These trends occurred over a range of frequencies between 1 and 15 Hz; however, only those at 1 and 10 Hz are shown here for brevity. As k_l and k_t increase, the speed for the millirobot asymptotes to a constant value. This is expected as, for undulatory gaits used here, speed is enhanced by body rotation, and a stiffer backbone decreases the relative motion between segments, reducing body rotation. For example, doubling k_l from 14.5 N/m to 29 N/m decreases the leg swing angle from 50.1 degrees to 46.0 degrees and the segment rotation from 13.1 degrees to 8.0 degrees for a seven segment robot. The asymptotic nature illustrates that beyond a certain point, increasing the backbone stiffness has no effect on speed of locomotion.

While this result alone suggests that the backbone should be made as compliant as possible due to the consistent increase in speed with decrease in spring constant, stability must also be considered. Stability in the horizontal plane is defined as having no collisions between adjacent segments. Unstable solutions are plotted with a velocity of zero in Fig. 4.2. For very compliant backbones, the backbone is able to compress to the point at which adjacent segments collide. For k_t, the speed tends to level off at low stiffness before becoming unstable, whereas for k_l, the speed increases dramatically at low compliances before suddenly becoming unstable.

Based on these observations, to maximize speed, it is desirable to choose the smallest values for k_l and k_t that produce stable locomotion. A larger k_l has to be chosen for millirobots with more segments. For example, at 1 Hz, a millirobot with 5 segments remains stable at k_l as small as 4.5 N/m, but a millirobot with 15 segments only remains stable at k_l down to 14.5 N/m. This is due to the fact that for the same backbone stiffness, a 15 segment millirobot will experience more segment rotation than a 5 segment millirobot since it uses a smaller phase difference. This is also frequency dependent. At lower frequencies, such as 1 Hz, there are collisions between segments at k_l as large as 23 N/m, but at 10 Hz, collisions do not occur until k_l is reduced to 4.6 N/m. At higher frequencies, the stance changes before segments can rotate to the point of collision.

Increasing k_l and k_t causes the speed of locomotion to decrease; however, for most frequencies tested, the decrease in speed from the smallest stable stiffness to the point at which the speed asymptotes is larger when varying k_l. The decrease in speed when varying k_l was three times larger at 1 Hz and twice as large at 5 and 10 Hz compared to the decrease in speed from varying k_t. This shows that k_l has more of an effect on locomotion than k_t. In some cases, k_l can cause a speed decrease as much as 50 percent before it asymptotes

While the simulation is very useful in predicting trends of locomotion, there are minor differences that occur with the experimental system based on simplifying assumptions made when formulating the dynamic model in Chapter 3. This suggests that parameters should be chosen to avoid cases where the locomotion borders on the edge of stability. For example, Sec. 4.2 illustrates that the backbone should be made

as compliant as possible without allowing collisions to occur between segments (considered unstable). If there are small differences in experimental locomotion compared to the simulation, such as feet slipping, manufacturing variations, etc., the smallest backbone compliance before gaits become unstable may differ. Due to this, a buffer was given when choosing parameters near regions of unstable gaits. Based on the desire to keep the millirobot modular and add or remove segments without changing the backbone pieces, the minimum stiffness that produced stable locomotion for the millirobot lengths and driving frequencies used in these experiments was chosen to maximize speed. The chosen values are illustrated in Fig. 4.2 as vertical red lines.

4.2.2 Sarrus linkage attachment point

In addition to altering the backbone stiffness, the lateral distance of the sarrus linkage attachment point from the COM of the segment, w_{sa}, was also altered. It should be noted that in a previous version of this millirobot described in Chapter 2, the backbone had a single sarrus linkage between segments and ran along the center of the robot. By having two sarrus linkages and moving the attachment points away from the COM of the segments, the compression force of the sarrus linkages applies a restoring moment about the segment COM. Similar to increasing k_l and k_t, increasing w_{sa} decreases millirobot speed by applying a larger moment about the segment COM as the backbone compresses, reducing body rotation and undulatory effects. Most of the unstable cases occur at points of attachment close to the COM due to these smaller moments not providing sufficient feedback to keep segments from colliding.

For low frequencies, the backbone parameters have very little effect on three-

a) varying torsional spring constant, k_t

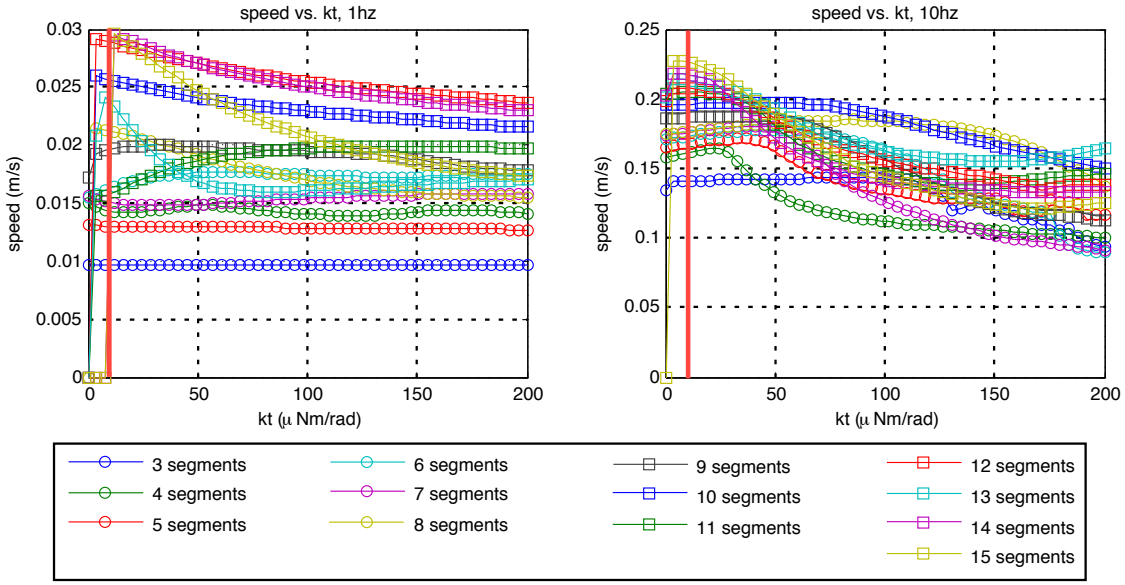

b) varying linear spring constant, k_l

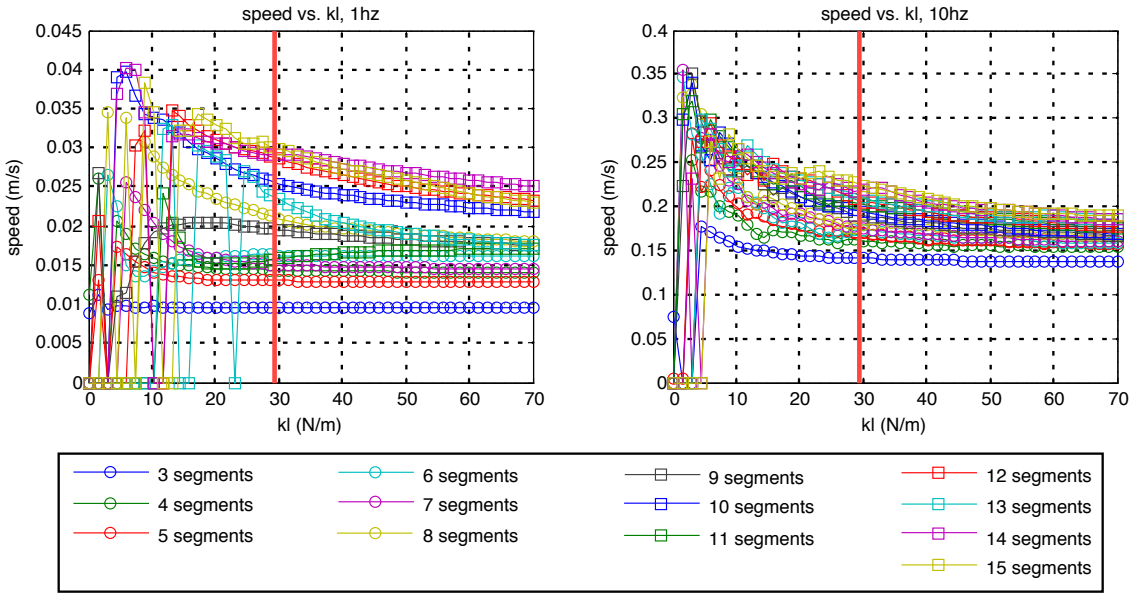

Figure 4.2: Speed as a function of a) torsional backbone spring constant, k_t, and b) linear backbone spring constant, k_l with chosen values illustrated by vertical red lines.

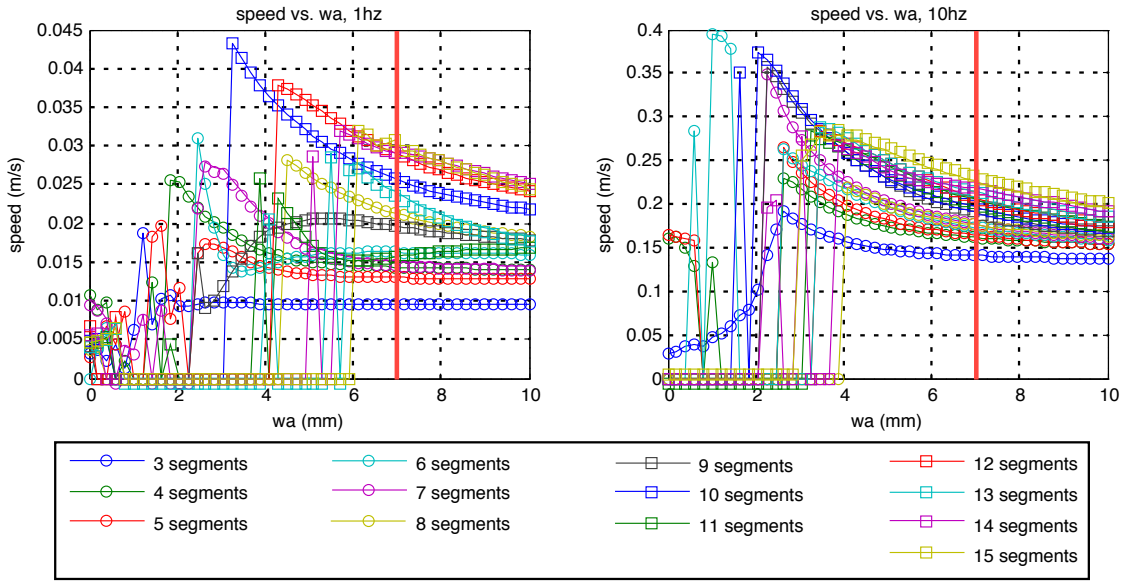

Figure 4.3: Speed as a function of sarrus linkage attachment point, w_{sa}, with chosen values illustrated by vertical red lines.

segment millirobots, which use the alternating gait. For the alternating gait at low frequencies, as will be shown in Chapter 5, the segment oscillates before coming to rest around an equilibrium point of zero body rotation when the stance changes. This equilibrium point of zero body rotation is independent of backbone stiffness. The backbone stiffness merely affects the amplitude and frequency of oscillations, which, at low frequencies, subside before the stance changes.

4.3 Conclusion

To choose segment parameters, an operating frequency was specified and an iterative process was used to find segment parameters. The analysis in Sec. 4.2, along with the gait studies in Chapter 5, suggest that the passive backbone should be as compli-

ant as possible to allow for large amplitude undulations while still providing sufficient feedback between segments to avoid collisions. The parameter studies performed here act as a guide for the design of a miniature centipede millirobot capable of stable and agile straight-line locomotion useful for understanding many-legged locomotion at small scales as is shown in the remaining chapters.

Chapter 5

Straight-line locomotion

Many centipedes exhibit wavelike motion of the body when moving at high speeds as depicted in Fig. 5.1(a). The phases between segments allow the stance legs to group together along the length of the body, with the body curving around these groups. This is in contrast to the alternating gait employed by rigid body hexapods at this scale with a phase of 180 degrees between adjacent leg pairs. The effectiveness of these undulatory gaits demonstrated by many centipedes have long been debated by biologists. Manton, who did visual studies on centipede locomotion and body morphology in the 1950's, argued that the undulations were passive. At low speeds, these undulations were less pronounced as compared to when the same specimen were traveling at higher speeds [45]. This led her to conclude that at low speeds the centipedes were able to suppress any body waves that would naturally arise, whereas when moving faster, the centipedes were unable to actively work against the undulations. Conversely, while using both visual information as well as electromyograms attached to the lateral flexor muscles situated along the body of a centipede, Anderson found that

centipedes actively promote body undulations [4]. Groups of legs form pivot points along the length of the body, which curves around the points (Fig. 5.1(a)). This body rotation may act to increase step size as compared to alternating gaits (Fig. 5.1(b)).

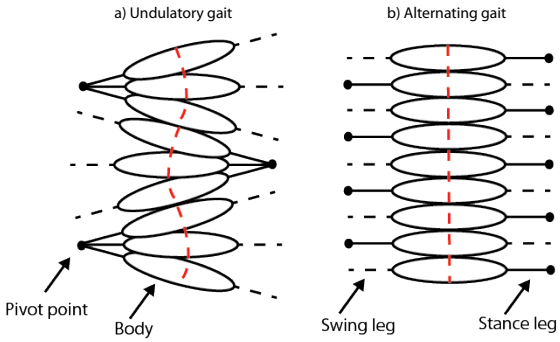

Figure 5.1: Illustration of a) undulatory and b) alternating gaits for a segmented creature, with red dashed line showing body curvature.

Many larger centipede robots use undulatory gaits for locomotion [34], [55], [53]; however, these robots have motors located between segments for the ability to directly specify segment rotation. The unique body morphology presented in Chapter 2 features passive flexures as intersegmental connections, requiring the use of different techniques to determine efficient gaits without direct control over segment rotation. This work seeks to find the best gaits, in terms of speed and cost of transport (COT) for a centipede millirobot with a passively flexible body and how these gaits compare to those found in nature.

Most of the text and figures in Sec. 5.1 are taken directly from [1] ©2011 IEEE, reprinted, with permission, while the majority of the text and figures in Sec. 5.2 are from [2] ©2012 IEEE, reprinted with permission.

5.1 10 segment millirobot

As the only system input is the torque at the hip joint and the timing of stance change, it was not immediately obvious that it would be possible to achieve undulations without direct control over the relative segment rotation. To explore the range of possible gaits, simulations and experiments of a 10-segment millirobot for various frequencies and phase differences were performed. A 10-segment millirobot was chosen as a variety of gaits can be demonstrated while still maintaining static stability.

5.1.1 Simulation results

Using the experimental system parameters, holding the leg cycle frequency constant at 5 Hz, applying a constant torque about each stance leg, and varying the phase of stance change between adjacent segments, the motion of the system was simulated for 500 steps for phases between 40 and 180 degrees. The drive signal for each individual segment was held constant at a specified torque for each gait; only the timing of stance change between adjacent segments was altered. This was done for a 10-segment, 20-leg robot, due to the wide variety of gaits that can be performed with this number of legs. At a phase difference of 180 degrees, all adjacent segments have opposite stance feet, similar to the alternating tripod gait used by hexapods. Below a phase difference of 40 degrees, or $\frac{360}{n-1}$ degrees where n is the number of segments, a 10-segment robot is not statically stable in the vertical plane, as clumps of legs no longer form a tripod. The results of the simulated motion are shown in Fig. 5.2.

Only stable solutions are shown, with stability in the horizontal plane being de-

fined as no collisions between adjacent segments (for 500 steps). The lack of data points between a phase of 97 and 172 degrees in Fig. 5.2 indicates a region of unstable gaits. In this region, there are only clumps of one and two legs. With many groups of legs distributed along the length of the body, legs are switching groups too quickly to pull each segment along the same path as the adjacent anterior segment. The robot fails to reach a limit cycle, eventually resulting in collisions between segments. At smaller phases and, therefore, larger groups of three or four legs, a single segment constitutes a smaller portion of the whole group, thus being easily pulled along the same path as previous segments when switching between groups of legs as stance changes. Additionally, this does not happen for phases around 180 degrees due to symmetry that comes with adjacent segments having opposite stance feet.

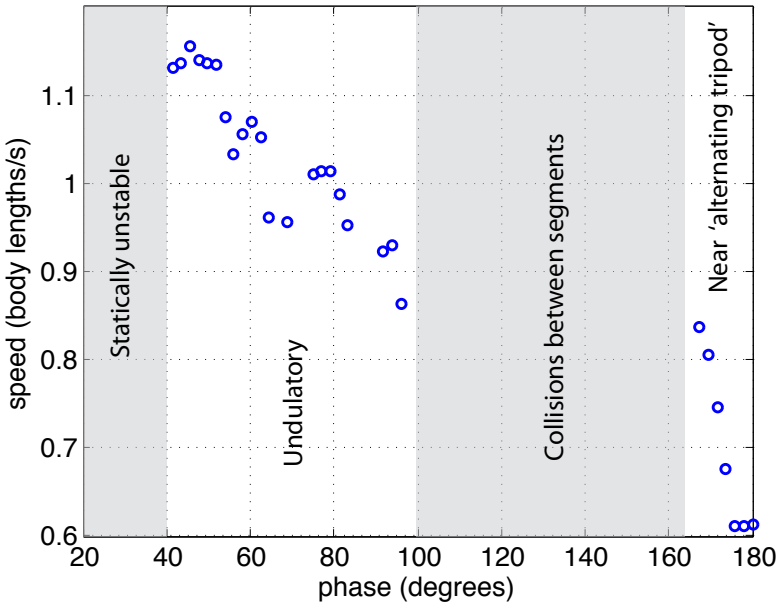

Figure 5.2: Simulated average speed at 5 Hz stepping frequency as a function of phase difference between adjacent segments. Only stable solutions are plotted.

The interesting part of this study is that the average speed decreases from a

maximum at a phase difference of 45 degrees to a minimum at 180 degrees, or the same phase used in the alternating tripod gait in hexapods. This speed difference can be attributed to the amount of segment rotation, θ, and leg rotation, α, for each segment at the time of stance change. For a phase difference of 180 degrees, when adjacent segments have opposite stance feet, the segments experience an initial negative rotation as the leg is rotating forward. Due to the opposite rotation of adjacent segments, the segment will oscillate around an equilibrium rotation of zero degrees before coming to rest. This is illustrated in Fig. 5.3(a). Conversely, for phase differences between 45 and 60 degrees, clumps of legs form pivot points around which the body and legs rotate. The segment rotates forward until the stance changes when at a positive segment rotation (Fig. 5.3(b)). This is analogous to a flexible beam that has perpendicular forces applied at the foot pivot points. The body curves around the pivot points for a group of legs similar to how a beam would bend under forces, causing this positive body rotation, increased rotation of stance legs, and wave-like motion of the center of mass of each segment, resulting in amplification of step size. This body bending evenly distributes the energy stored in the backbone flexures. For the case in Fig. 5.2, undulations almost double the step size compared to the alternating gait. It is important to note that these undulations are passive, arising merely from choosing the correct phase of stance change, unlike those of larger robots, which are directly controlled using motors [34], [55], [53].

Not only is the average speed for phases between 45 and 60 degrees (undulatory gaits) the largest for these operating conditions, but the body undulations demonstrated by these gaits are qualitatively similar to those of real centipedes [4],[45]. As

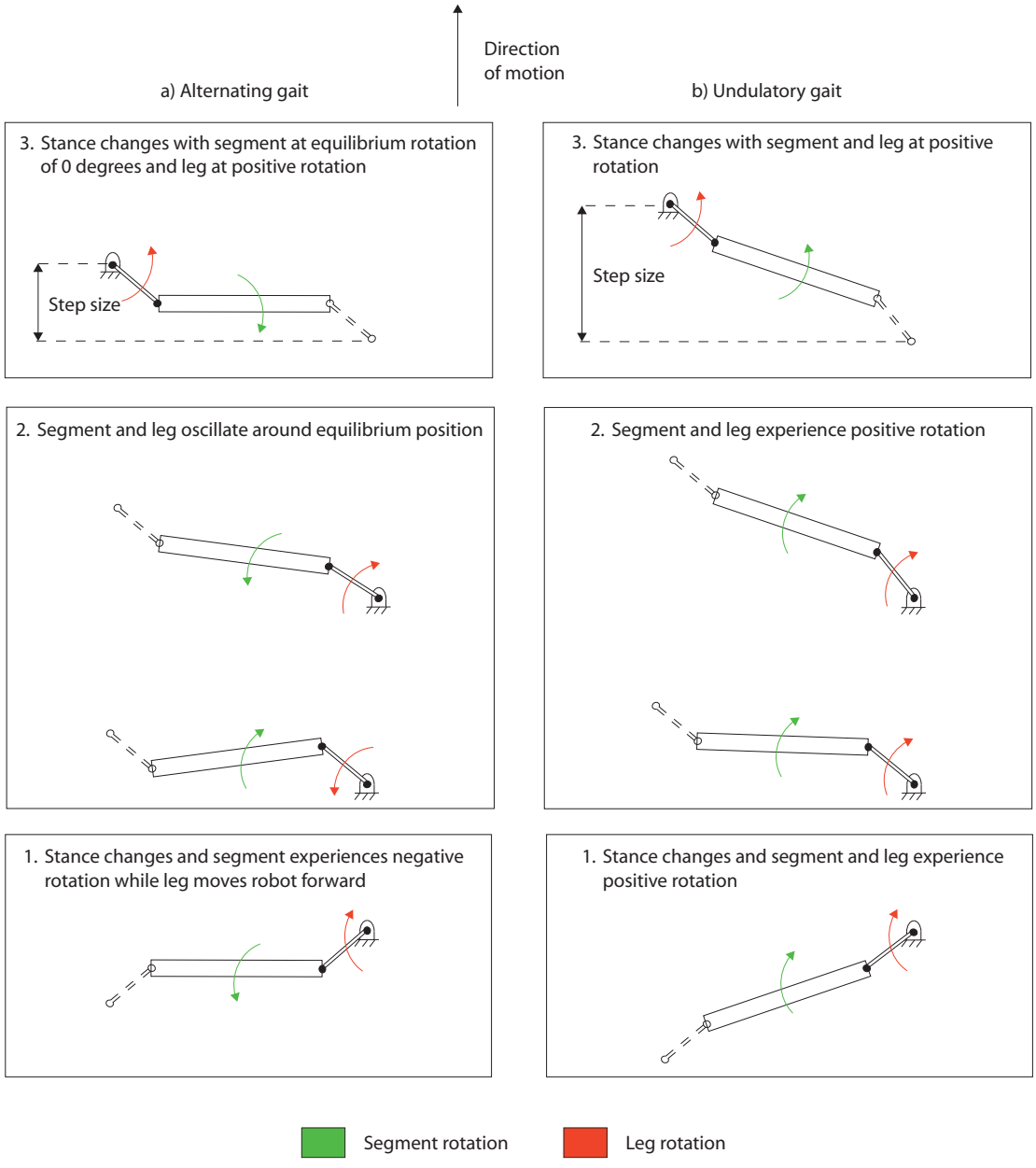

Figure 5.3: Illustration of segment and leg rotation over a single step for the a) alternating and b) undulatory gaits.

can be seen for a phase of 60 degrees in the frames of motion in Fig. 5.4, the legs form clumps pointing in towards a pivot point, while the centers of mass of the segments form a traveling wave along the length of the body. This shows that even though the design is underactuated with a passively flexible body, undulations mimicking those of actual centipedes are expected to result from the natural system dynamics, causing increases in speed for the same leg cycle frequency and body parameters as compared to alternating gaits.

To explore gaits over a range of frequencies, two representative gaits were chosen. The first gait is characterized by a phase of 180 degrees between adjacent segments, or 'alternating gait.' The second gait uses a phase of 60 degrees, an 'undulatory gait.' While a phase of 45 degrees should result in a faster average speed, a phase of 60 degrees allows drive signals to be shared between segments, which is beneficial for the experimental system. As shown in Fig. 5.7(a), the undulatory gait was found to produce a higher average speed than the alternating gait for a range of frequencies in simulation. For the undulatory gait, the motion over the range of frequencies was found to be similar to that described above and shown in Fig. 5.4. The degree of segment and leg rotation, or the magnitude of the resulting undulations, varied slightly across frequencies. For the alternating gait, at low frequencies, the segments would experience negative rotation followed by oscillations around an equilibrium value of zero degrees due to adjacent segments rotating in the opposite direction. This occurred mainly for frequencies up to 8 Hz; however, beyond 8 Hz, it is possible to see that the gap in average speed between the two gaits begins to close. While driving the robot at a frequency that will cause the stance to change when the segments are

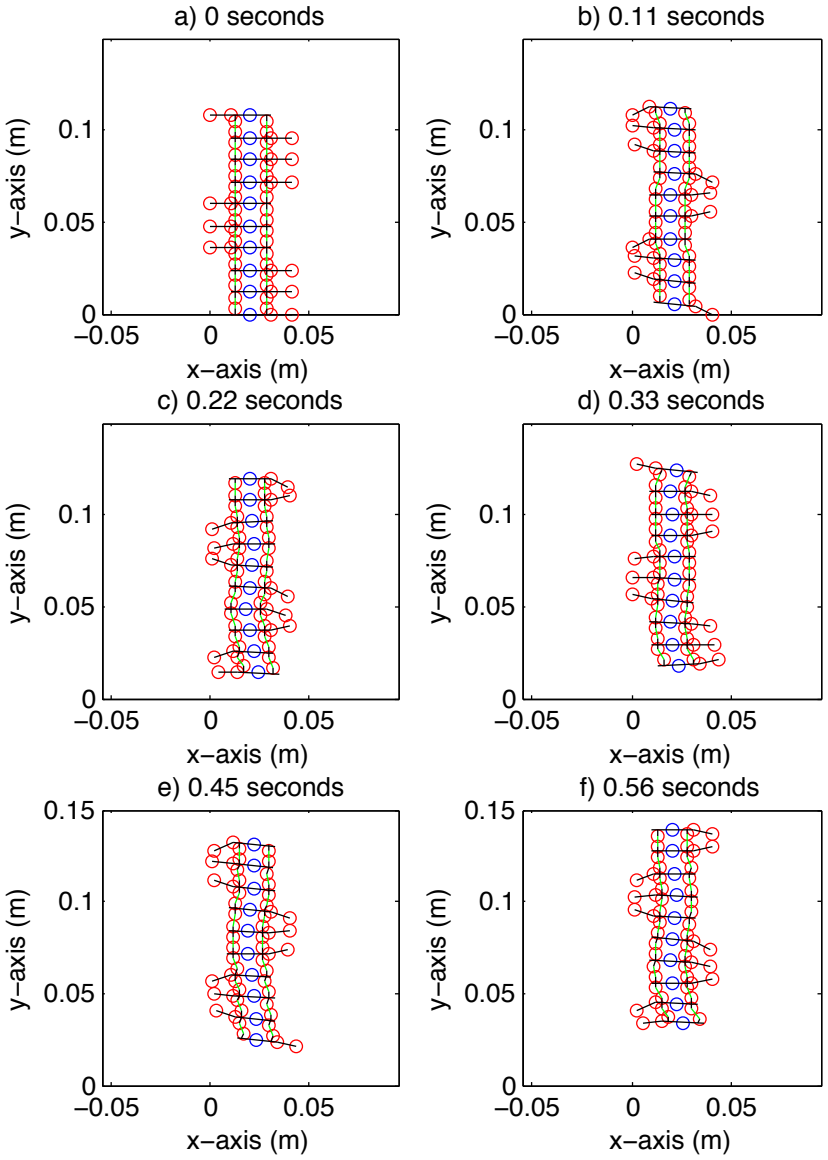

Figure 5.4: Simulated undulatory motion using a 60 degree phase difference between adjacent segments at a 3 Hz leg frequency. The red circles indicate the stance feet and hip joints, the blue circles represent the center of mass of each segment, the green lines are the Sarrus linkages, and the black lines are the body and legs. The swing legs are not shown.

at the point of maximum rotation for the alternating gait, which for the parameters chosen here is approximately 11 Hz, an undulatory gait at the same frequency is still predicted to perform better. This is due to the initial negative segment rotation for the alternating gait while for the undulatory gaits, the segment is always rotating in the direction of locomotion. The segment natural frequency of 11 Hz is dictated by the segment inertia and actuator spring and damping constants. This is discussed in more detail in Chapter 4.

The simulation was used to calculate the cost of transport (COT), defined as the absolute value of the mechanical work per unit distance traveled per mass, for each gait. Fig. 5.5 shows that the undulatory gait requires less work per unit distance as a result of negative body rotation and oscillations of the COM for the alternating gait. Efficient locomotion is particularly important for small-scale robots, which generally have limited power supplies.

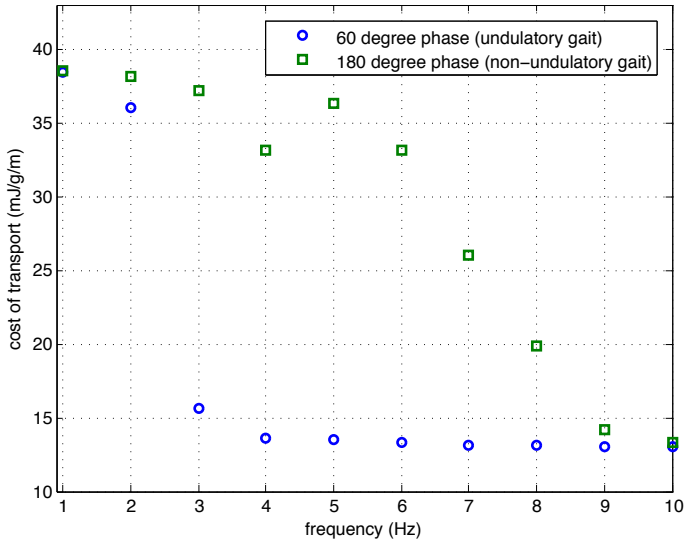

Figure 5.5: Cost of transport for phases of 60 degrees and 180 degrees from simulation.

5.1.2 Experimental results

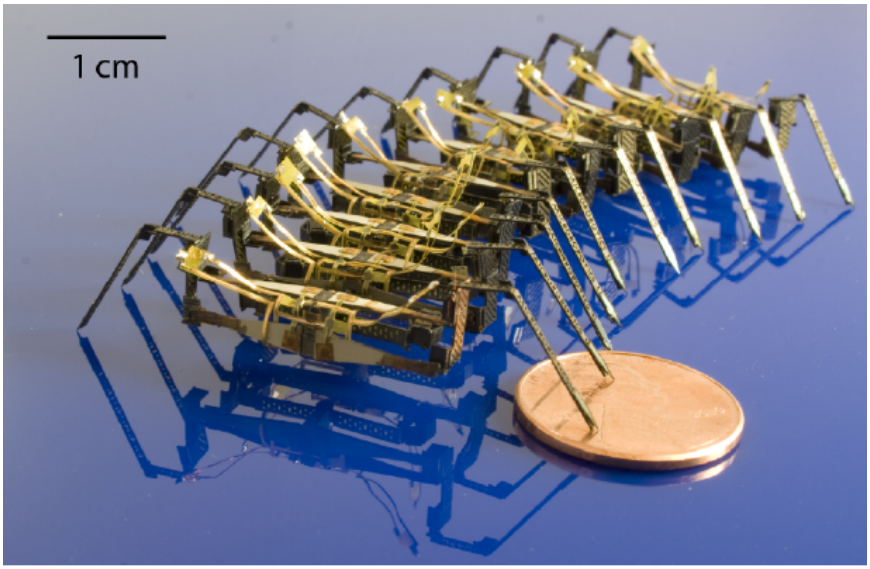

Figure 5.6: 10-segment centipede millirobot used in straight-line locomotion studies.

To verify the simulation predictions, a selection of gaits and leg cycle frequencies were tested in the 10-segment experimental device (Fig. 5.6) on flat terrain. The average speeds were recorded for each frequency and are shown in Fig. 5.7(b). For all frequencies excluding 10 Hz, the undulatory gait was as fast as or faster than the alternating gait. Similar motion was observed experimentally as was predicted in simulation, demonstrating that passive undulations can arise merely by altering the phase of the stance change between segments. Frames of motion for the undulatory gait are shown in Fig. 5.8. As in simulation, for the alternating gait, the legs experience positive rotation but spring back to an equilibrium position by the time the stance changes, while the segments undergo negative rotation but spring forward to an equilibrium rotation of zero degrees. The undulatory gait featured body undulations that acted to increase step size. The leg and body rotation at the time

of stance change, which affects the step size, was confirmed for each gait at 1 and 3 Hz using videos and motion analysis software (ProAnalyst). The experimental and simulated body and leg angles are recorded in Tab. 5.1, showing the average angles at stance change are larger for the undulatory gait. The maximum frequency tested here was 10 Hz, at which the robot reached a speed of approximately 7 cm/second. The actuators can be driven at higher frequencies, although the robot performance at higher frequencies was not tested at this time.

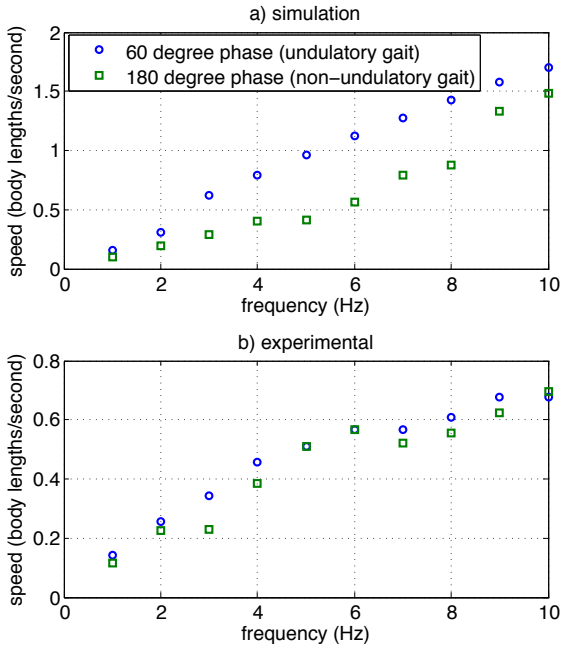

Figure 5.7: a) Simulated and b) experimental average speeds for phase differences of 60 degrees and 180 degrees over a range of frequencies.

For both gaits, the COM of the middle segment was tracked experimentally and predicted in simulation for frequencies of 1 and 3 Hz. The COM position in the direction of motion of the millirobot was plotted as a function of time (Fig. 5.9). Both in simulation and experiments using the alternating gait, the COM moves forward

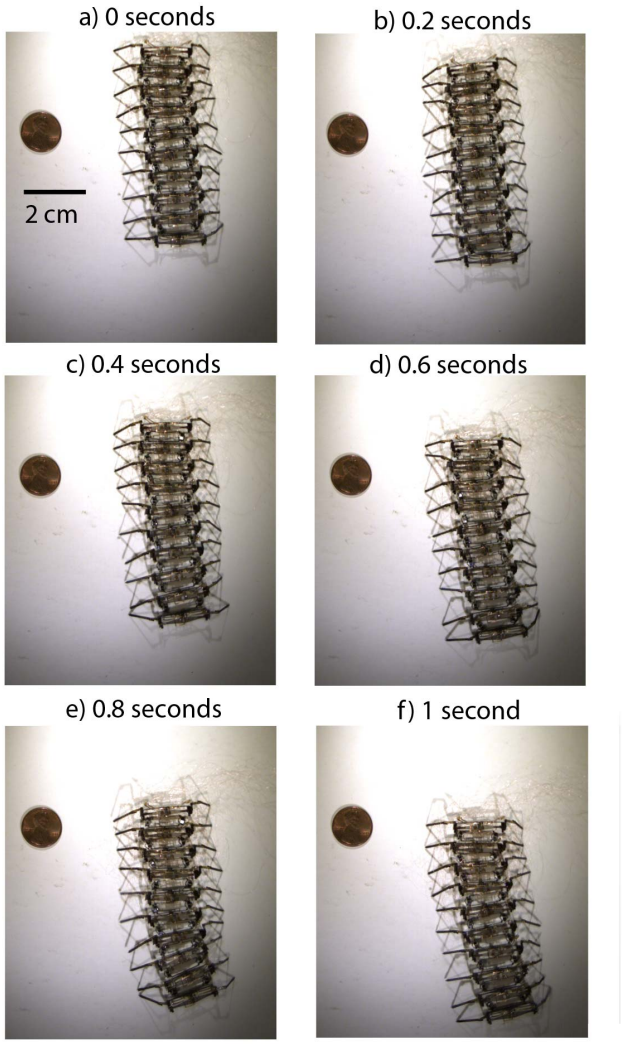

Figure 5.8: Frames of motion from experiments using a 60 degree phase difference of the stance of adjacent segments at a 3 Hz leg frequency.

Table 5.1: Average body rotation θ and leg angle α (degrees) at stance change averaged over 10 segments for five steps

F (Hz)	Phase (deg)	α_{sim}	θ_{sim}	α_{exp}	θ_{exp}
1	60	40.9	2.7	30	2.2
	180	26.6	0	25	-0.2
3	60	50.3	4.4	20	0.9
	180	26.5	0	15	0.2

then oscillates around an equilibrium position. When the COM moves opposite of the desired locomotion direction, energy is wasted. Alternatively, for the undulatory gait, both the simulation and experiments show the COM spring back slightly for a frequency of 1 Hz, but move steadily forward for a frequency of 3 Hz. The undulations that arise for this gait allow for a smooth forward motion of the center of mass, particularly at frequencies greater than 3 Hz

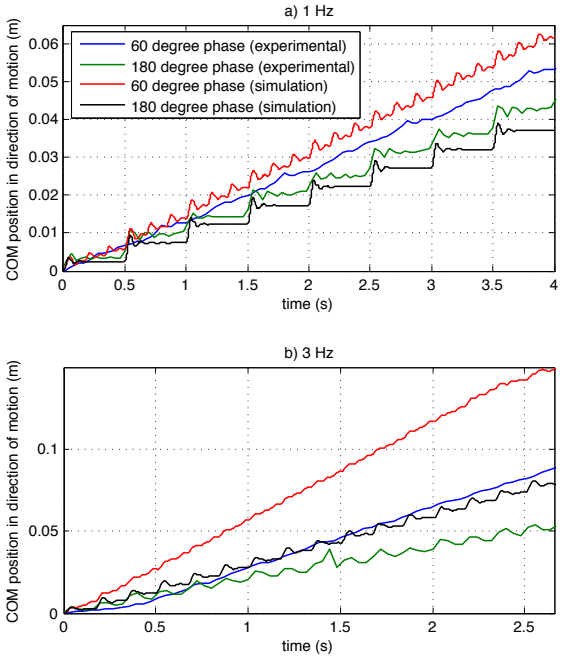

Figure 5.9: Experimental and simulated center of mass position for 60 and 180 degree phases at a) 1 Hz and b) 3 Hz.

While the trends for locomotion are similar for the simulation and experiments, the experimental average speed is generally smaller than that predicted in simulation, and the body undulations are not as pronounced. Unmodeled foot slipping, flexure damping, or coupling between horizontal and vertical plane motion could contribute to the slower experimental speeds. Motion could also be affected by fabrication differences

between segments due to manual assembly steps. Any differences in performance of a segment affects the motion of adjacent segments. External wiring may have an effect on locomotion as well. These differences were reduced in later versions of this millirobot by eliminating fabrication defects and improving foot-ground contact with thicker stance actuators and improved feet.

This study was performed with specific body parameters, although the geometries and compliances affect the severity of undulations. For example, as shown in Chapter 4, for a stiffer backbone, body undulations will be less pronounced; however, similar trends as shown here still occur. Increasing the stiffness of the backbone as much as two orders of magnitude still results in enhanced locomotion with undulatory gaits as compared to the alternating gait. This is due to the initial negative body rotation for the alternating gait as opposed to the positive body rotation for the undulatory gaits, although less pronounced than those with a more compliant backbone. Conversely, for a more compliant backbone, there will be less feedback between segments, leading to collisions between segments.

5.2 Varying number of segments

In Sec. 5.1, passive body undulations were shown to enhance locomotion for a 10-segment millirobot; however, due to the modular nature of the design, it was necessary to explore if this trend could be expanded to encompass millirobots with various numbers of segments and determine if there is an optimal phase for n-segment millirobots.

5.2.1 Simulation results

Straight-line locomotion is parameterized by the following:

1. bias voltage, $+V$
2. frequency, f
3. phase between segments, ϕ
4. ramp rate of the trapezoidal drive signals

To determine the best straight-line gaits as a function of number of segments in simulation, the phase of stance change between segments was varied while applying a near-constant torque at the hip joint of each segment. When varying the number of segments between 3 and 15 and varying the phase between 2π and $\frac{2\pi}{n-1}$ radians for a range of frequencies between 1 and 15 Hz, 86 percent of the cases showed $\frac{2\pi}{n-1}$ radians was the best phase based on maximizing speed and minimizing COT for an n-segment milirobot. For an additional five percent of cases where $\frac{2\pi}{n-1}$ radians was not the optimal phase, the percent difference in speed between the best phase and $\frac{2\pi}{n-1}$ radians was less than two percent, implying that generalizing $\frac{2\pi}{n-1}$ radians as the optimal phase does not result in any loss in performance. Most of these exceptions occurred in millirobots with less than six segments, which have a smaller range of phases that allow for static stability and less variation in speed among gaits. This can be compared to the alternating gait (phase of 2π radians), which, in some cases, can be up to twice as slow as a phase of $\frac{2\pi}{n-1}$ radians. In general, there was an upward trend in speed and downward trend in COT as phase decreased from 2π to

$\frac{2\pi}{n-1}$ radians. Fig. 5.10 shows the optimal phases for three frequencies evaluated based on speed, COT, and a combination of both with a cost function of

$$min\left(\frac{COT_\phi - COT_{\frac{2\pi}{n-1}}}{COT_{\frac{2\pi}{n-1}}} + \frac{v_{\frac{2\pi}{n-1}} - v_\phi}{v_{\frac{2\pi}{n-1}}}\right) \tag{5.1}$$

This shows that, in general, $\frac{2\pi}{n-1}$ radians is the optimal phase for this millirobot.

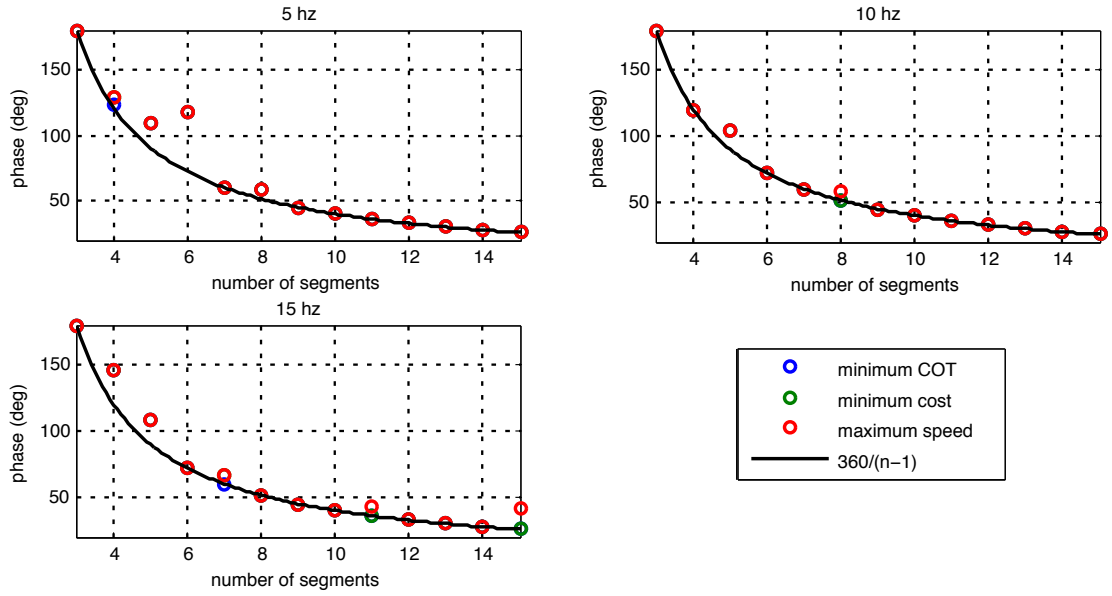

Figure 5.10: Optimal phase as a function of number of segments in terms of speed and COT

The optimal phase of $\frac{2\pi}{n-1}$ radians is the smallest phase between segments that still allows the groups of stance legs that form along the length of the body to result in a tripod, maintaining static stability in the horizontal plane. Having three groups of legs is also very similar to undulatory centipede gaits found in nature [4]. In both nature and this millirobot, the body curves around the groups of stance legs, increasing step size in the same fashion as the 10-segment millirobot in Sec. 5.1.

Again, for this millirobot, these undulations arise passively. This is illustrated in the frames of motion from a simulation for a seven-segment millirobot in Fig. 5.11(a).

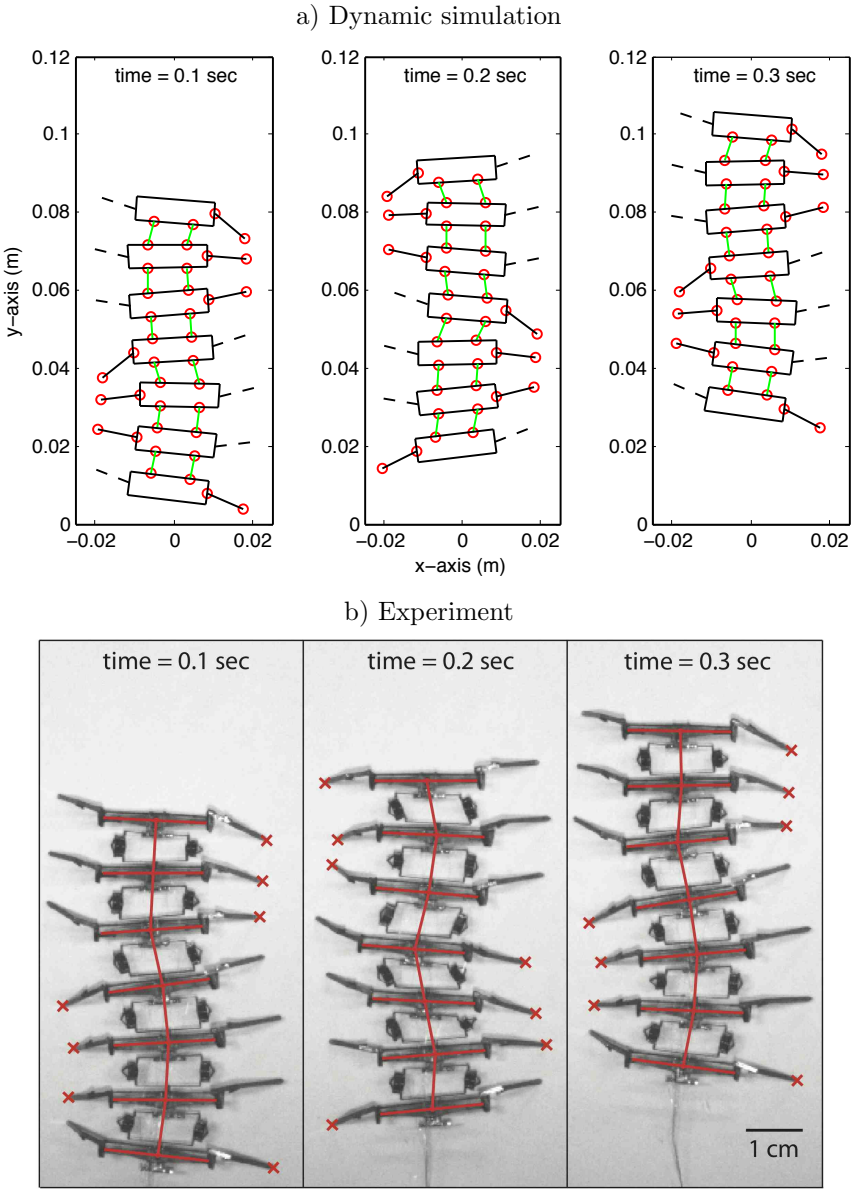

Figure 5.11: Frames of motion for passive undulatory gaits for a 14-leg millirobot a) simulated using a hybrid-dynamic model and b) observed experimentally at 5 Hz.

The speed for millirobots with different numbers of segments are plotted for a representative frequency of 10 Hz in Fig. 5.12 using the optimal phases of $\frac{2\pi}{n-1}$ radians.

The alternating gait results in the slowest speeds across the range of segment numbers as well as the highest COT. This gait is generally used by rigid-body hexapods, but here, causes body oscillations that reduce step-size and waste energy. Since this is the only phase a three-segment robot can use with contralaterally coupled legs while still maintaining static stability, this body morphology may not be the ideal choice for hexapods. There is a general upward trend in absolute speed as the number of segments increases and the phase between segments decreases. As the phase between segments decreases, the amount of positive body rotation of each segment at the time of stance change increases, amplifying the severity of body undulations. This occurs due to the increase in spacing between stance pivot points, allowing more severe body curvature. Adding additional segments allows the phase to be decreased while still having a tripod of stability, allowing for millirobots with more segments to have larger undulations and faster gaits. These results predict that even for millirobots with only four segments, it is still possible to have locomotion-enhancing body undulations.

While the absolute speed increases, the speed relative to the body length decreases as shown in Fig. 5.13 over a range of frequencies for the four millirobot sizes that will be used in the experiments. In each case, the optimal undulatory gait is a better choice than the alternating gait. An additional undulatory gait was plotted for eight segments to show that the undulatory gait with the smallest phase ($\frac{2\pi}{n-1}$ radians) causes more positive body rotation than other undulatory gaits. In this case, a phase of 90 degrees. For a fixed payload, such as onboard sensors, there could be a larger increase in absolute speeds as number of segments increases and phase of the drive signal decreases.

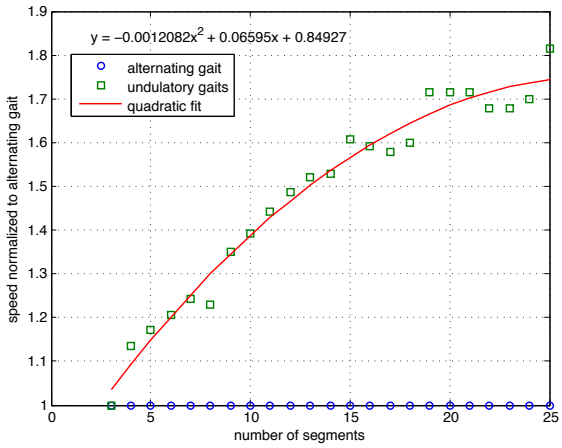

Figure 5.12: Speed as a function of number of segments for alternating and optimal undulatory gaits at 10 Hz normalized to alternating gait speed.

5.2.2 Experimental results

To verify the simulation results, the optimal undulatory gaits ($\frac{2\pi}{n-1}$ radians) and alternating gaits were tested on five through eight segment millirobots for 1-10 Hz. An external power supply and high voltage amplifier, controlled by Matlab and an xPC target system (Mathworks) were used to drive the millirobot. The average speed of two trials for each gait at each frequency are plotted in Fig. 5.14. This frequency range was chosen because above 10 Hz, there is a tendency for feet to slip with respect to ground, which causes losses and variations from the dynamic model. As can be seen, the optimal undulatory gaits result in faster straight-line locomotion over the entire frequency range for a variety of millirobots with differing numbers of segments compared to the alternating gait. Similar to the simulation results, frequencies between 4-8 Hz show the largest improvement over the alternating gaits. This is due to the negative body rotation for the alternating gait being at its maximum as the stance changes before it springs forward to zero body rotation, or no

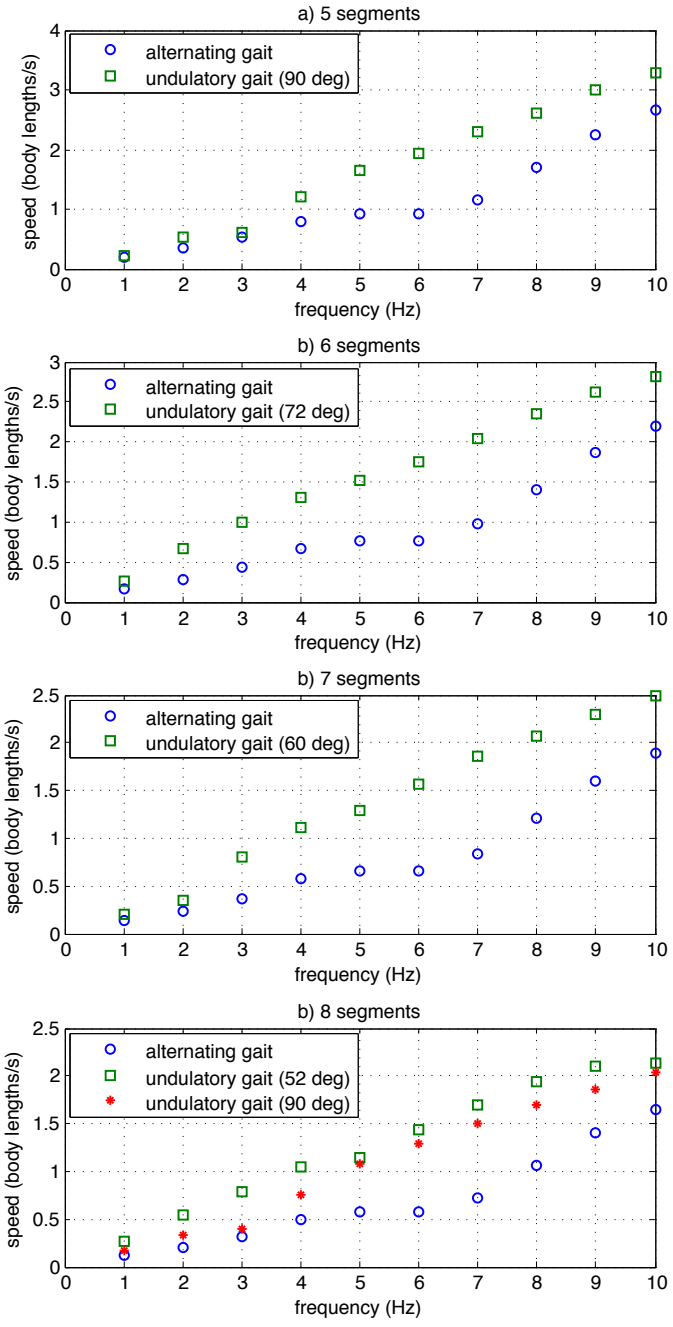

Figure 5.13: Simulated average speeds for alternating and optimal undulatory gaits from 1-10 Hz for a) five segments b) six segments c) seven segments and d) eight segments.

increase in step size. The benefit of each segment being offset by a certain phase from adjacent segments is that it simplifies the components necessary for onboard control. Upon generating the control signal for the first segment, each segment merely needs to phase shift that signal. This was also the motivation for the simple technique used for turning in Chapter 6 as additional electronic components onboard can be costly for a robot at this scale.

While the optimal undulatory gait for each length millirobot was generally an improvement over the alternating gait, there was not a noticeable increase in absolute speed as segment number increased. This could be due to slight differences between the model and actual millirobot, such as feet slipping, external wiring, or unmodeled flexure losses; however, the simulation was able to predict an improvement seen by the passive body undulations as compared to the alternating gait. As segment number and undulations increase, the ground reaction force increases, potentially making the feet more likely to slip.

Using high speed video (500 fps) of millirobots with 5, 6, 7, and 10 segments obtained as baseline speeds for the robustness experiments in Chapter 7, the average leg and body rotation over the course of eight steps was obtained (Tab. 5.2). This shows average body angles at the time of stance change between 0.23 and 4.2 degrees (i.e. half the total body rotation over the course of a step), illustrating that a phase of $\frac{2\pi}{n-1}$ radians creates undulations with positive body rotation to increase step size. Note that these results were taken from the robots used for the experiments in Chapter 7 as high speed video was unavailable for the data in Fig. 5.14. These robots featured improved stance actuators to reduce foot slipping and a stiffer transmission to prevent

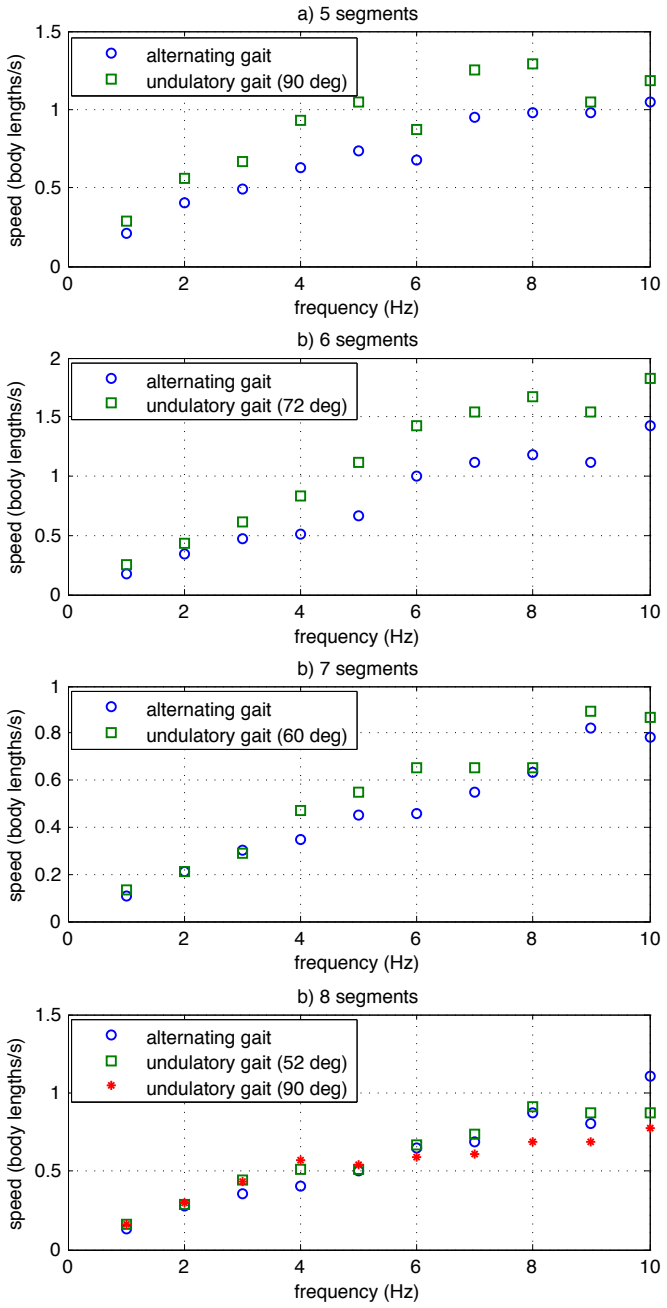

Figure 5.14: Experimental average speeds for alternating and optimal undulatory gaits from 1-10 Hz for a) five segments b) six segments c) seven segments and d) eight segments.

Table 5.2: Total body rotation θ and leg angle α (degrees) during a step averaged over eight steps

Segments	$\Delta\alpha_{exp}$	$\Delta\theta_{exp}$
5	29.6	8.4
6	31.5	7.5
7	29.5	6.8
10	22.6	0.46

flexure buckling that caused the experimental results to match those of the simulation more closely. Experimental frames of motion for a seven segment millirobot are shown in Fig. 5.11(b) which compare very well to the simulation frames in Fig. 5.11(a).

Due to the brittle nature of the piezoelectric actuators, instead of using a pure square wave to switch the torque when controlling opposite legs on the same segment, it is necessary to ramp the voltage up to the maximum value. It was found, both in simulation and experimentally, that the undulations become more pronounced as the ramp rate is increased, approaching a constant hip torque. In these experiments, a ramp rate of 10 kV/s was used, although for the turning scheme chosen and described in Chapter 6, a frequency dependent ramp rate worked best. The transition between straight-line locomotion and turning could involve altering the ramp rate, or the ramp rate could remain constant to reduce the complexity of the control strategy with a slight decrease in body undulations.

5.3 Conclusion

The work presented here demonstrates locomotion enhancement using undulatory gaits in centipede millirobots with varying numbers of legs. Increased leg and body

angles for an undulatory gait, which arise due to the passive dynamics of the system rather than being directly specified, were shown to increase the average speed of the millirobot compared to the alternating gait. This suggests millirobots inspired by the body morphology of centipedes can see improved straight-line locomotion by using undulatory gaits that feature groups of legs pointing towards similar pivot points distributed along the length of the body by merely altering the phase of stance change between segments. This shows that undulations can arise even with this novel underactuated design and passive body, not requiring individual motors placed between segments to directly specify segment rotation. Similar gaits have been found in nature [4], providing insight into biology and perhaps supporting the idea that undulations may assist flexible-body creatures in attaining high speeds by increasing step size.

Chapter 6

Turning

In addition to straight-line locomotion, methods for turning were also studied. Strategies used for miniature, underactuated cockroach millirobots involve stiffening the middle leg on one side of the body to introduce an asymmetry into the alternating gait [32], introducing a second actuator to bias the nominal gait [8], or adding a tail that rotates a mass to cause the robot body to rotate via conservation of angular momentum [50]. Turning by either altering the swing of contralateral legs or relative segment rotation was suggested for a larger centipede robot [70] which is made possible due to the actuators located between segments.

The goal for establishing a turning gait was to find a simple method that did not involve introducing additional actuators, can be easily extended to a robot with any number of segments, and can be blended with the nominal undulatory gaits described in Chapter 5. To do this, it was necessary to use the drive signals to cause an asymmetry in the gait of the robot and perturb it from its straight-line locomotion. The difficulty in this comes from the legs being coupled across the body,

with one leg being placed on the ground as the opposite is being lifted and the torque applied to the stance leg affecting the touchdown angle of the swing leg. While this greatly simplifies the robot design and reduces the number of drive signals necessary to control the robot, it presents challenges when introducing contralateral asymmetries into the gait. Additionally, unlike larger centipede robots, this millirobot features passive joints between segments, so turning can not be achieved merely by directly controlling the relative rotation between segments.

Most of the text and figures in this chapter are directly from [2]

6.1 Simulation

The simulation was unable to give an accurate representation for turning due to the high forces on the feet causing them to no longer act as perfect pin joints, but was used to gauge if two strategies would cause any asymmetries in the gait. The first strategy involved applying a larger torque to the stance leg on one side of the body as compared to the opposite leg by biasing the drive signal voltage. This method showed very little perturbation from the nominal straight-line gait due to the coupling between legs. The leg being subjected to a smaller torque on one side of the body rotated less. However, due to the coupling between legs, the leg subjected to the larger torque had a smaller initial touchdown angle, and, therefore, also experienced less rotation. A second method for turning involves changing the duty-cycle for the stance control actuator, causing the legs on one side of the body to remain on the ground longer than the legs on the opposite side and, therefore, have a larger stride.

In simulation, this proved to cause a larger asymmetry in the gait than biasing the torque. Using this method, contralateral legs would be subject to the same maximum torque as for straight-line locomotion, just for different lengths of time.

6.2 Experimental Results

To implement turning experimentally, a Matlab controller was created based on the parameterization of the turning strategy with the ability to smoothly transition between turning and straight-line locomotion. Turning via altering the time opposite legs are on the ground can be parameterized by the following:

1. duty-cycle for the stance and swing control signals, t_d
2. the ramp rate for the trapezoidal drive signals

To simplify the controller, the frequency and phase between segments will remain constant for straight-line and turning locomotion. The duty-cycle must be chosen to cause an asymmetry in the drive signal, but still maintain static stability in the vertical plane. A duty-cycle of 50 percent represents a symmetric drive signal. For example, a duty cycle of 100 percent would mean all stance legs are on one side of the body (with 0 percent meaning all stance legs are on the opposite side of the body), which is not statically stable. The minimum duty-cycle that can be used while still maintaining static stability is dependent on the number of segments and phase between segments. In the experiments performed here, a duty-cycle of 25 percent for left turns (or 75 percent for right turns) was used, as it was compatible with the five through eight segment robots used in the experiments and their nominal gaits.

Note that this strategy would not work for hexapods as static stability would not be maintained for any duty-cycle other than 50 percent.

While a fast ramp rate of 10 kV/s works best when changing the torque applied to the swing DOF for straight-line locomotion, a frequency dependent swing drive signal ramp rate works better for turning. It was found, by altering the ramp rate experimentally, that the ramp rate for the swing drive signal that causes the highest turning rate is $0.8f$ kV/s for a bias voltage of 200 V and duty-cycle offset of 25 percent (where f is frequency). The straight-line and turning drive signals are shown in Fig. 6.1. By having a ramp rate of $0.8f$ kV/s for turning, the drive signal is ramped slowly enough to just hit the voltage limit, or maximum torque, for the leg that is on the ground for the shorter time span before the stance is switched. This means the maximum torque on that hip is applied for the shortest amount of time while still allowing the opposite leg to fully reset in preparation for the next step due to the coupling of the legs. The ramp rate of the stance control always remains at 10 kV/s to switch stance as close to instantaneously as possible.

Another choice had to be made as to whether all legs would be involved in turning or if turning could be achieved by merely altering the gait of the first segment. It was found experimentally that only altering the duty-cycle of the first segment creates large reaction forces on the stance feet of the first segment, causing them to slip as the remaining segments push the first segment forward. This does not result in turning. Additionally, requiring all segments to be involved in turning not only distributes the asymmetry along the length of the millirobot, but it also allows each segments' drive signal to be the same as the first segment, merely offset by a constant phase. Each

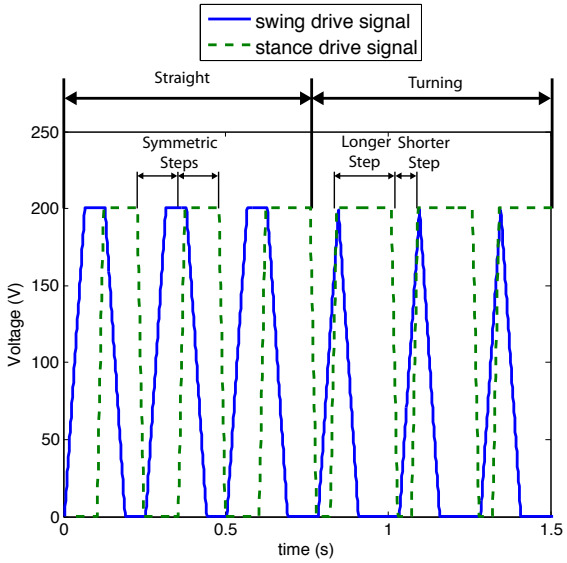

Figure 6.1: Drive signals for stance and swing control for straight-line and turning motions.

segment begins the turn at a time of $\frac{\phi}{2\pi f}$ seconds (where ϕ is in radians) after the adjacent segment.

To demonstrate turning for robots with an arbitrary number of segments, the method described here was implemented in millirobots with five, six, seven, and eight segments. Each of the four millirobots were run at 4 Hz. Five cases were tested: straight-line locomotion using the optimal undulatory gait, walking straight for 10 steps then turning left or right for the remainder of the time, and walking straight for 10 steps followed by turning left or right for 16 steps (two seconds) then walking straight for the remainder of the time. Each trial was repeated five times to test for consistency for a total of 25 runs per robot. Representative plots of the center of mass (COM) are shown for five and eight-segment millirobots in Fig. 6.2, although similar results were also found for six and seven-segment millirobots, demonstrating the effectiveness of this turning method for a modular millirobot. The orientation of

the millirobot is illustrated by the images of the millirobot as it appears at the end of each of the five different experiments. As can be seen in Fig. 6.2, when changing the duty-cycle of the drive signal, the millirobot is able to consistently perform left and right turns, as well as alter the severity of turns by changing the amount of time spent turning. This also shows that it can easily transition between straight-line locomotion to turning and back again.

For each of the above trials for five through eight segment millirobots, the average turning rate and turning radius were calculated and are shown in Fig. 6.3. There was no obvious correlation between turning rate or radius and number of segments. The turning radii were all in the neighborhood of one body length.

To demonstrate that this turning strategy works over a range of frequencies, it was tested on the six-segment millirobot between 1-10 Hz, using a drive signal ramp rate of $0.8f$ kV/s, where f is frequency, and a 25 percent offset in duty-cycle. The turning rates and radii are plotted in Fig. 6.4. As can be seen in Fig. 6.4(a), the turning rates for this six-segment millirobot increase to a maximum of 8 deg/s at 10 Hz. The increase in turning radius with frequency is less consistent, but higher frequencies tend to result in a larger turning radius.

Consecutive turns were performed using a six-segment millirobot over a range of frequencies. The COM tracking with three video frames of the robot at different positions during the maneuver from a trial at 4 Hz is shown in Fig. 6.5.

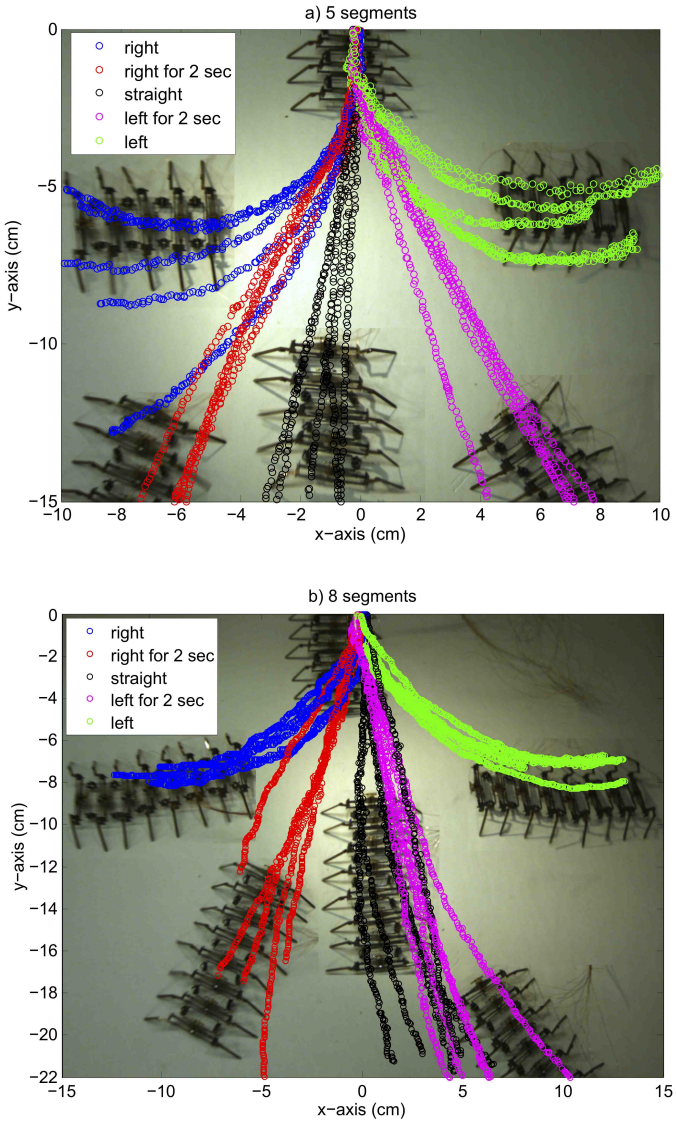

Figure 6.2: Center of mass tracking for turning and straight-line gaits for a) five-segment and b) eight-segment millirobots at 4 Hz.

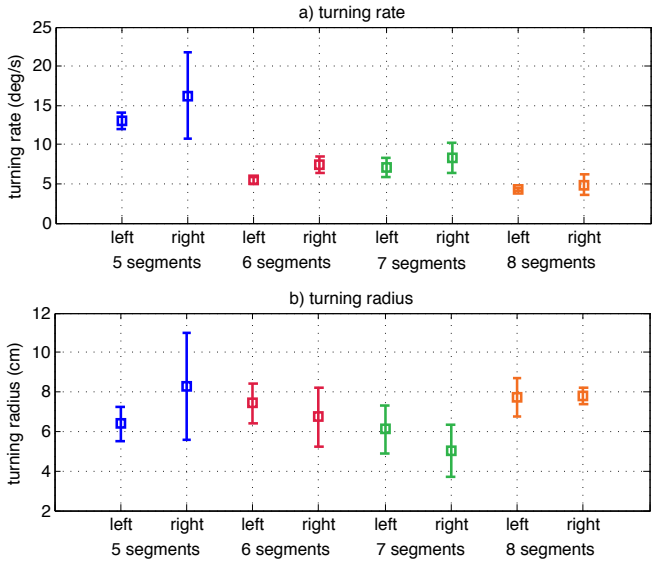

Figure 6.3: a) Turning rate and b) turning radius averaged over five trials for millirobots with five through eight segments. Error bars represent one standard deviation.

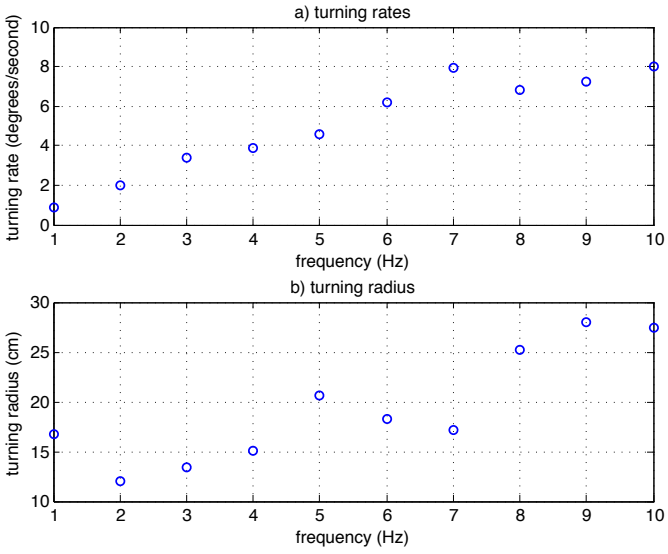

Figure 6.4: a) Turning rate and b) turning radius as a function of frequency for a 6-segment millirobot.

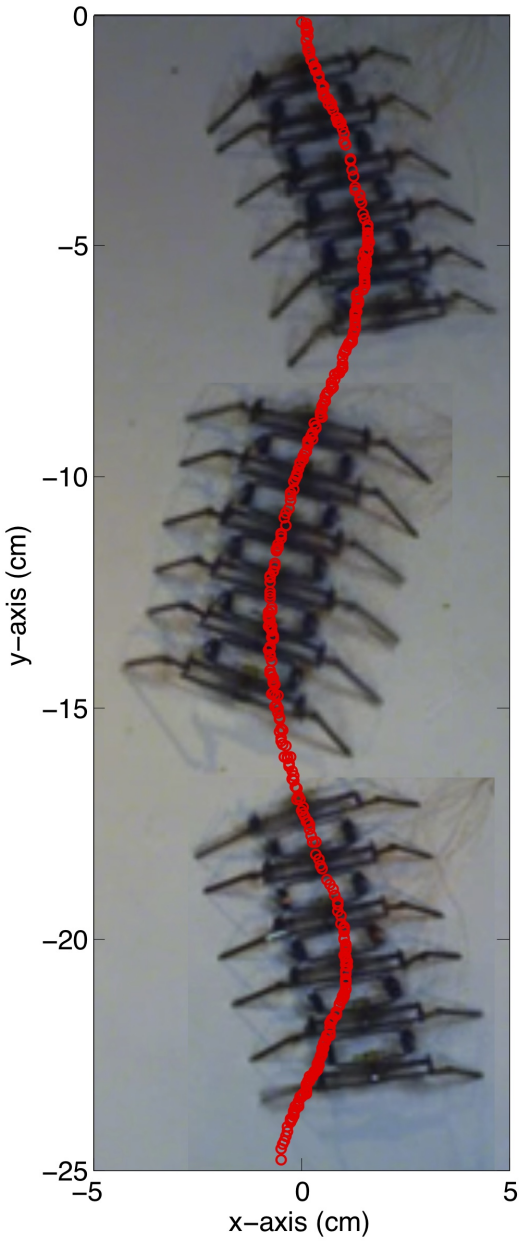

Figure 6.5: Center of mass tracking of six-segment millirobot performing consecutive turns at 4 Hz.

6.3 Conclusion

A simple turning strategy which alters the duty-cycle of the stance control was developed and implemented in the millirobot. This turning strategy worked for millirobots with varying numbers of segments and transitions between straight-line locomotion and turning were demonstrated. Most importantly, coupled with the driving strategy for straight-line locomotion, only two drive signals are needed to produce coordinated motion of all the legs of a centipede millirobot with any number of segments, reducing the number of onboard controllers necessary for future autonomy.

Chapter 7

Robustness

In nature, it is common for legged arthropods to experience limb failure. A study on Harvestmen collected in nature found that nearly half of the samples had at least one leg missing with twenty-five percent having two or more legs missing [28]. A similar study on the Spider *Scytodes globula* showed that out of 162 field collected samples, 36 had missing legs, with a higher percentage having the front legs missing than any other legs [3]. An extensive study of 2560 centipedes showed approximately 33 percent with one of the last legs missing and 25 percent with any other leg missing [24]. While many small creatures have the ability to regenerate limbs, it sometimes takes weeks for this to occur [13], requiring the creature to be able to locomote to feed or escape prey in the meantime. A study on Wolf Spiders showed that in the presence of leg failures, the average speed of locomotion decreased from 15 cm/s to 11 cm/s for males and approximately 25 cm/s to 18 cm/s in females [5]. Similar results have been found in Harvestmen [29]. Additionally, to maintain static stability, particularly at lower speeds, many creatures will alter the phase between legs to account for missing

legs [20].

Robustness strategies focusing on sensing the location of missing limbs and altering the gait to maintain static stability have been formulated for legged robots both in simulation [18], [10], [69], [54], [41], [47], [16], [17] and experiments [57], [22]. The strategies used for these macro-scale robots focus on adapting gaits to maintain static stability and forward locomotion rather than on designing redundancy into the system. At larger scales, it is feasible to introduce sensors to specify the location of missing legs and compute new gaits. The robot used in [22] to compute fault tolerant gaits has 19 DOF, 60 sensors, and eight computers. However, as robots are scaled down, computing power is limited, sensors become more costly due to smaller payload capacity, and robots tend to be underactuated. While different gaits have been studied in simulation for macro-scale robots with four, six, and eight legs, an experimental study looking at performance degradation as a function of nominal number of legs has not been performed.

To fulfill the demand for small, agile robots for swarm robotics applications, multiple miniature legged robots have been created. Most of these weigh on the order of 20-30 grams [32], [8] or 1.5-2.5 grams [7], [33] and are modeled after rigid body hexapods. Similar to their biological counterparts, it is expected that these robots will suffer limb failures when in use. Many of the robots at this scale are underactuated, using one motor or drive signal for leg pattern generation and another to introduce asymmetries for turning. This makes it mechanically difficult, if not impossible, to alter the gait to account for specific missing legs even if there is enough payload capacity for controllers and sensors to compute new gaits. Given this limitation, we

hypothesize that a robot with more mechanical redundancy, such as a myriapod-like body morphology, will allow legs to be lost while maintaining static stability and forward locomotion capabilities without altering the gait.

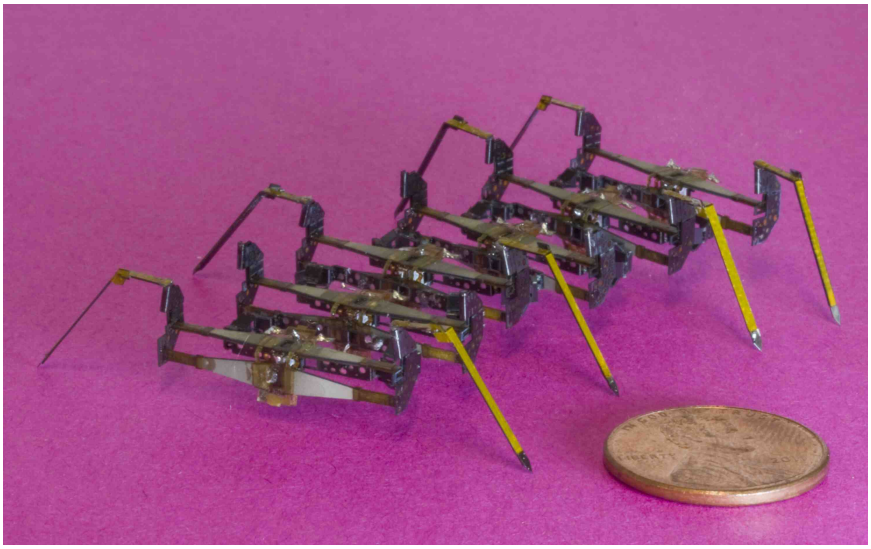

Figure 7.1: Centipede millirobot with multiple missing legs adjacent to a U.S. penny for scale.

To understand the benefits of having many legs as it relates to locomotion robustness when leg failures occur, the following questions need to be answered:

1. How many legs can be lost before an underactuated n-segment millirobot is no longer statically stable without changing the gait to account for missing legs?

2. What is the decrease in performance as a function of percentage of missing legs and does robustness to leg failures increase with nominal number of legs?

3. Is there any benefit to having sensors on-board to identify missing legs and adjust the gait to maintain static stability or improve forward locomotion?

4. Does the location of missing legs affect performance?

To answer these questions, the static stability as a function of number of legs, number of missing legs, and phase between segments was evaluated (Sec. 7.1). Sec. 7.2 describes the experimental approach taken to understand practical limitations of robustness for millirobots with 3, 5, 6, 7, and 10 segments (Fig. 7.1). This work shows that even with significant leg losses, the centipede millirobot displays performance degradation, instead of catastrophic failure, even without altering the gait (Sec. 7.4). Sec. 7.5 discusses which gait to choose when too many legs are missing and static stability is compromised. Sec. 7.6 shows that the location of missing legs along the length of the body does not affect performance, and that there are larger decreases in speed when more legs in a row are missing due to off-axis body compliance.

7.1 Static stability

It has been found that for an underactuated centipede millirobot with n segments, a passive backbone, and no missing legs, the best gait, in terms of speed and cost of transport, typically has a phase between adjacent segments of $\frac{360}{n-1}$ degrees [2]. Concerning static stability of a millirobot with missing or broken legs, there are three cases to consider:

1. No legs are missing.

2. A few legs are missing, but not enough to compromise static stability (i.e. the groups of stance legs form at least a tripod along the length of the body).

3. Too many legs in a row or legs on the first and last segment are missing, and static stability is compromised.

For the first and second cases, the gait does not need to be altered from the optimal undulatory gait to maintain static stability; however, for the third case, the gait has to be altered.

Using the optimal undulatory gait, the number of segments in a row that can be missing legs before the millirobot loses static stability is $n_{critical} = floor(0.5(n - 3))$. This arises from the fact that, using a constant phase between segments and having contralaterally coupled legs, the maximum phase between two adjacent fully functional segments cannot be greater than 180 degrees. As the number of segments increases, the number of segments in a row that can be broken asymptotes to 50 percent of the total number of segments. In terms of static stability for underactuated robots, this suggests the benefit for having more legs is more apparent when comparing 3-segment robots to 5-segment robots as opposed to comparing, for example, a 20-segment robot to a 21-segment robot (Fig. 7.2).

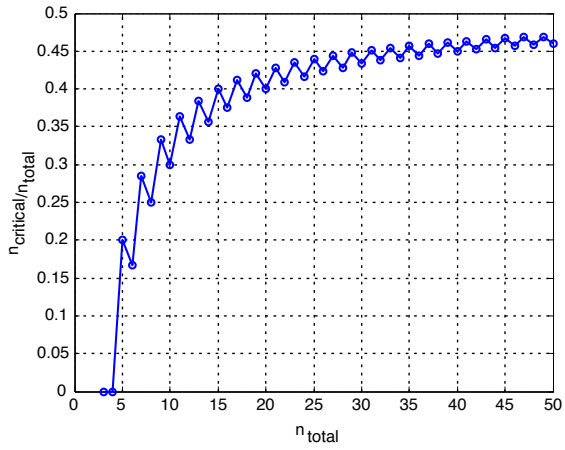

Figure 7.2: Maximum percentage of segments in a row that can be missing for an n-segment millirobot to maintain static stability.

While $n_{critical}$ is merely dependent on the nominal number of segments, the total number of legs that can be missing depends on the location of the missing legs. For example, if the first, middle, and last segments are fully functional, all additional legs can be lost and the millirobot will still maintain static stability without altering the gait from the nominal undulatory gait.

For the optimal undulatory gait, the first and last segments cannot be broken without compromising static stability. Using a phase slightly larger than the optimal undulatory gait, such as $\frac{360}{n-2}$ degrees, would allow the first or last segment to be lost without having to alter the gait and with little performance difference compared to the optimal undulatory gait for a millirobot with no missing legs, particularly for millirobots with many legs. However, the tradeoff is that less segments in a row could be missing before static stability is lost. This strategy could be useful if it is expected that anterior or posterior legs are more likely to become damaged than middle legs as occurs in many arthropods [3], [24].

7.2 Experimental methods

An experimental approach was taken to investigate performance degradation as a function of number and location of missing legs. Millirobots with 3, 5, 6, 7, and 10 segments were tested open-loop over a range of frequencies (1-15 Hz) using an external power supply and controller on flat terrain. Each data point is the average of two trials. Trials were chosen to obtain combinations of missing legs to answer specific questions. 31 cases with different numbers of legs in a row missing, legs missing at different locations along the length of the body, and varying total numbers of legs

missing for each millirobot size were tested with two drive signals for each case.

Legs were disabled by disconnecting the segment drive signal and completely removing them from the hip joint, eliminating interference of the leg with adjacent segments or terrain. The extent to which this accurately represents real situations is unknown as there could be multiple modes of failure, including actuator failure, leg removal, or transmission damage. While leg interference with adjacent segments could be detrimental to locomotion, the problem of body sagging described in Sec. 7.6 may be alleviated if legs remain attached and assist with supporting the weight of the damaged segment due to the inherent hip joint stiffness. Compared to the segment mass, leg masses are negligible, therefore lost legs do not affect the weight of the millirobot.

7.3 Baseline speeds

The performance metric for robustness to leg failures was chosen to be the percent decrease in speed, v_d, relative to the baseline speed, v_b,

$$v_d = \frac{(v_b - v_m)}{v_b} \times 100 \tag{7.1}$$

where v_m is the speed when legs are missing. v_d was chosen in place of absolute speed since millirobots of different lengths exhibit different baseline speeds. Baseline speeds were collected for each millirobot length using the optimal undulatory gait (Fig. 7.3). The speeds for most of the millirobots, particularly those with 6, 7, and 10 segments are not linear with driving frequency, but rather have a slower rate of increase at

frequencies higher than 10 Hz. This is due to a combination of the dynamics of body undulations, foot/ground contacts, and limited ramp rate of the trapezoidal drive signal.

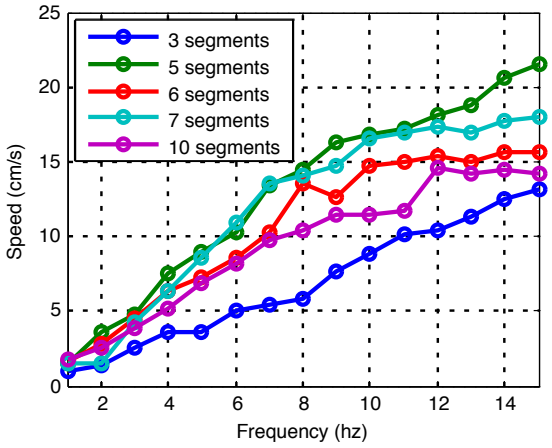

Figure 7.3: Baseline speeds for millirobots with 3, 5, 6, 7, and 10 segments with no missing legs.

7.4 Performance degradation

In order to determine if having more nominal legs results in a lower v_d without altering the gait, the decrease in speed as a function of the percentage of missing legs is plotted in Fig. 7.4 for various frequencies. It is important to note that for all of the points for 5, 6, 7, and 10 segments, static stability was not compromised by the removal of legs; however, for the data points for 3 segments, static stability was always lost as no legs can be removed from a 3-segment millirobot with contralaterally coupled legs without compromising static stability.

For cases in which the gait is not altered, the experimental results show that, as expected, there is an upward trend in v_d as a function of the percentage of missing legs

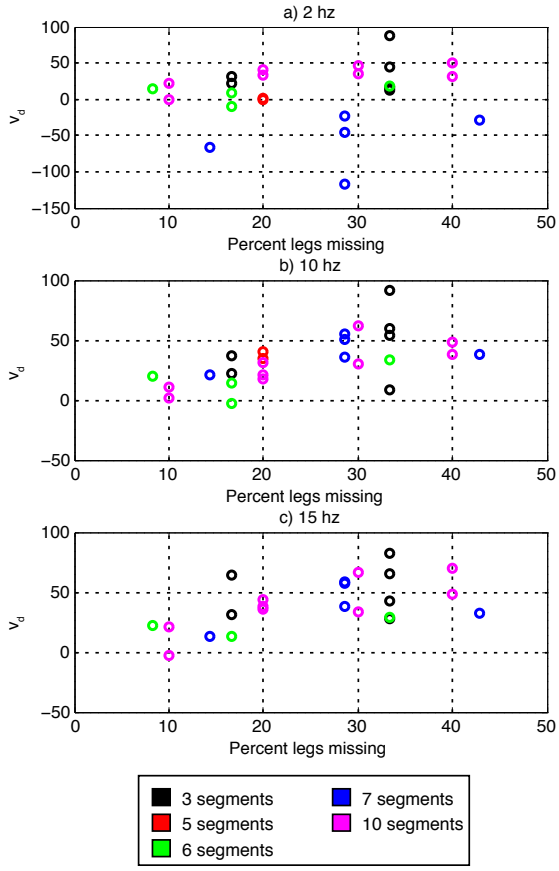

Figure 7.4: Percent decrease in speed as a function of the percentage of missing legs for various frequencies.

(Fig. 7.4). While the decrease in speed does become more severe with the percentage of missing legs, Fig. 7.4 shows that missing legs do not render this millirobot incapable of locomotion even when the gait is not altered. For example, one case shows that a millirobot with seven segments can have 43 percent of legs missing and only experience a 40 percent decrease in speed if the location of missing legs does not affect static stability. Additionally, for a 10 segment robot, 40 percent of legs can be missing and the decease in speed ranges from 48 to 70 percent without altering the gait. Note that for these cases, the broken segments were not all adjacent as that would result in a loss of static stability. There is variation among the data depending on the number of missing legs in a row, which is discussed further in Sec. 7.6.

Fig. 7.4(b-c) shows that v_d for hexapods is at the higher end of the range for the millirobots tested, although the decrease in speed is not significantly higher than that of millirobots with nominally more legs. Conversely, v_d as a function of absolute number of missing legs (Fig. 7.5) shows that having more than five segments results in less of a decrease in speed as legs are lost. For example, when one to two legs are missing, only having 3-5 segments results in speed decreases between 25-95 percent, while for 6, 7, and 10 segments, having one to two broken legs only causes a decrease in speed of 0-25 percent. If the number of expected leg failures is linear with the total number of legs, Fig. 7.4 suggests that, aside from a few critical cases, there may not be a benefit in terms of robustness to having more legs. Alternatively, if the expected number of leg failures is a sublinear function of the total number of legs, Fig. 7.5 shows that there could be a major performance advantage to having at least six segments. There is minimal difference in v_d between 6, 7, and 10 segments.

As discussed in Sec. 7.1, the number of legs that can be lost without compromising static stability increases with the number of segments. For all data points in Fig. 7.4 and Fig. 7.5 associated with milirobots with more than three segments, static stability was maintained without altering the gait. Every trial for the three-segment millirobot resulted in a loss of static stability due to the contralateral leg coupling, which cannot be fixed even by altering the gait. In many cases, this causes body-supported locomotion. There are also some cases for hexapods that cause critical failure. For example, if the middle legs are missing and the gait is not altered, the remaining segments are in phase, causing the robot to locomote laterally.

The decrease in performance is also frequency dependent, with less of a decrease occurring at lower frequencies, such as 1-4 Hz. In some cases, particularly for seven segments, the speed can increase when legs are missing. This is shown as a negative v_d in Fig. 7.4(a) and is a result of the natural dynamics of the segments and frequency of oscillation, which are altered when legs are missing (i.e. robot mass stays constant but hip stiffness is eliminated for missing legs). When no legs are missing, at very low driving frequencies, the segments can begin to oscillate backwards before stance changes; however, when legs are removed and the frequency of oscillation decreases, speed may increase. While the speed for a fully functional millirobot levels out slightly above 10 Hz, the average speed for millirobots with multiple missing legs begins to level out at 5 Hz (example cases shown in Fig. 7.9 and Fig. 7.11). This results in a larger decrease in speed at higher frequencies and a lower maximum achievable speed.

An additional performance metric that gives an indication of the stability of the system is the radius of curvature of the path of the center of mass (COM), R_c. For

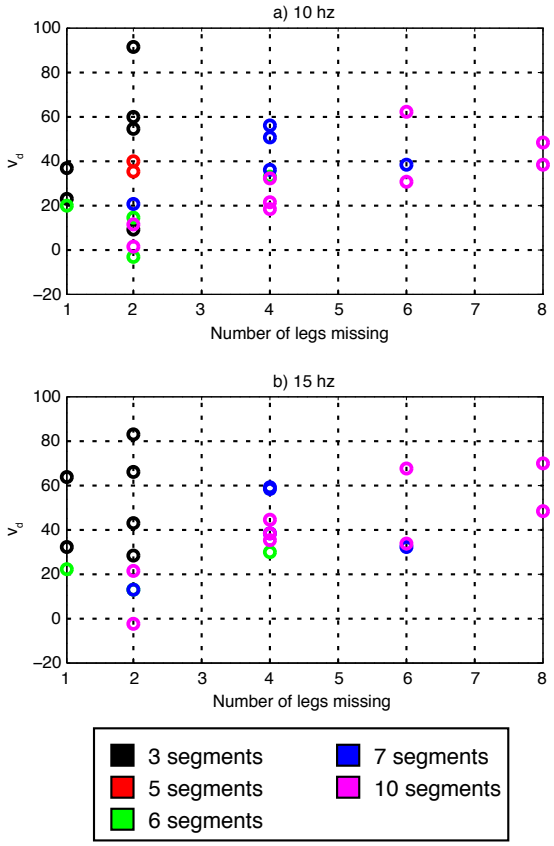

Figure 7.5: Percent decrease in speed as a function of the number of missing legs for various frequencies.

desired straight-line locomotion, if R_c decreases significantly as segments are removed, the direction of the millirobot may be more difficult to control. Fig. 7.6 shows that while there is not a significant correlation between R_c and the percentage of missing legs, R_c for three segments with missing legs is generally smaller than that with more segments when legs are removed for cases in which the gait was not altered. This is likely due to the loss of static stability. With all legs intact, the three-segment millirobot demonstrated R_c of similar magnitude to the other millirobots tested, showing that having more than three segments may help in preserving the directionality of the straight-line gait.

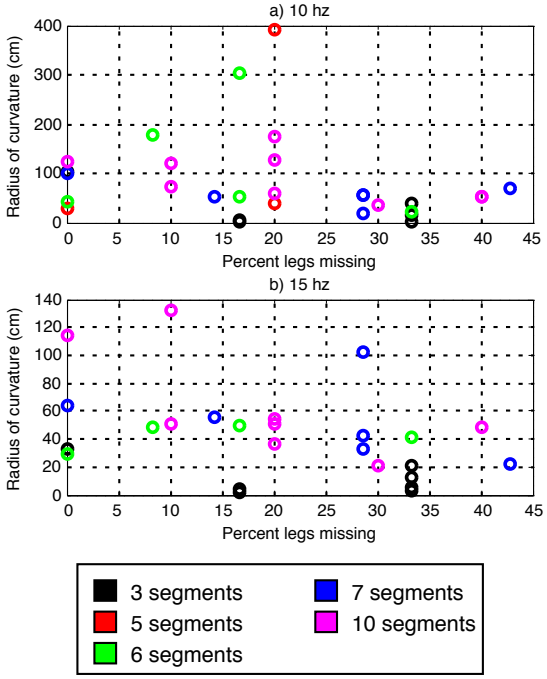

Figure 7.6: Radius of curvature as a function of percent of segments with missing legs for various frequencies.

7.5 Benefits to changing gait

7.5.1 Static stability conserved

If less than $n_{critical}$ segments in a row are broken and the first and last segments remain fully functional, static stability is not compromised, and it is not necessary to alter the nominal straight-line gait. However, if v_d is significantly less when altering the gait, it could be beneficial to have additional controllers and proprioceptive sensors on legs. Two different strategies were compared for a variety of combinations of missing legs:

1. Unaltered gait: The gait is not changed from the nominal gait (optimal undulatory gait) with a constant phase of $\frac{360}{n-1}$ degrees between all segments.

2. Nonexistent gait: A constant phase of $\frac{360}{n-(n_m+1)}$ degrees between fully functional segments is used, where n_m is the number of broken segments.

Both of these strategies are illustrated in Fig. 7.7(a). The unaltered gait does not require proprioceptive sensing, whereas the nonexistent gait uses knowledge of which segments are broken and alters the gait to act as if those segments do not exist. For example, with the nonexistent gait, a six-segment millirobot with one broken segment would use the optimal undulatory gait for a five segment millirobot with the phase difference constant between fully functional segments.

For all of the cases where the number of broken segments in a row is less than $n_{critical}$, the difference between using the nonexistent gait and not altering the gait was small, as can be seen by examples of these cases in Fig. 7.9 and Fig. 7.10. This

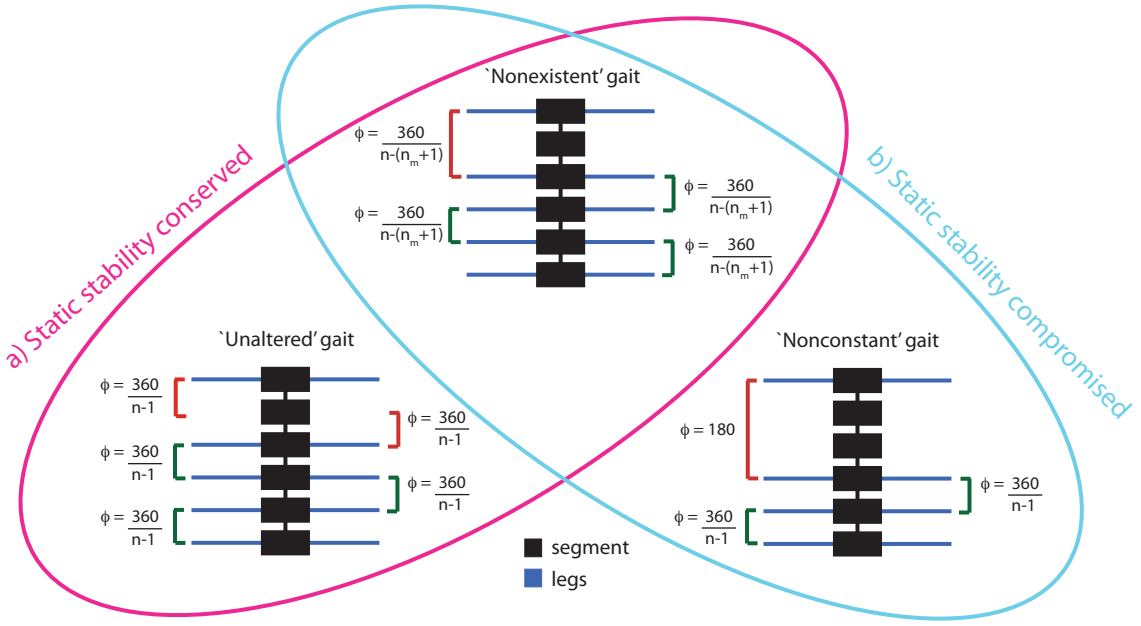

Figure 7.7: An illustration of the different gaits used when static stability is a) conserved and b) compromised.

suggests that it may not be beneficial to have additional sensing and control to alter the gait when static stability is not compromised; however, it is also conceivable that there is a different, optimal method of altering the gait that may result in increased performance. The nonexistent gait was merely chosen based on the idea that keeping a small constant phase between functional segments may assist in retaining beneficial undulations.

7.5.2 Static stability compromised

If more than $n_{critical}$ segments in a row or the first or last segments are broken or missing, altering the gait is necessary to maintain static stability. Two strategies were used for this:

1. Nonexistent gait: A phase of $\frac{360}{n-(n_m+1)}$ degrees, which is constant between fully functional segments, is used, where n_m is the number of broken segments. This is the same as the nonexistent gait for when static stability is conserved.

2. Nonconstant gait: The nominal optimal undulatory phase of $\frac{360}{n-1}$ degrees is retained between all segments, except the segment immediately following the group of more than $n_{critical}$ broken segments, which is altered to be 180 degrees out of phase of the segment immediately before the group of broken segments. This relies on the idea that static stability can be maintained as long as the phase between segments surrounding a group of broken segments is not more than 180 degrees.

Both of these strategies are illustrated in Fig. 7.7(b).

In the four experimental cases in which static stability was compromised, the nonexistent gait resulted in significantly higher speeds than the nonconstant gait, particularly at higher frequencies (Fig. 7.8). An example plot of the nonexistent and nonconstant gaits for a seven segment robot with the third, fourth, and fifth segments missing is shown in Fig. 7.10. The nonexistent gait caused a v_d of only 18 and 32 percent at 15 Hz for two segments in a row missing for a six-segment robot and three segments in a row missing for a seven-segment robot, respectively. This shows that even when more than $n_{critical}$ legs are missing, locomotion is still possible with only a small degradation in performance so long as the gait is altered. The nonconstant gait was chosen for its simplicity, only requiring one drive signal to be altered, while the nonexistent gait was chosen since the constant phase between functional segments was expected to assist in preserving body undulations. This was found to be the case

Table 7.1: Total body rotation θ and leg angle α (degrees) during a step averaged over 20 steps at 15Hz

Nominal Segments	Broken Segments	Gait	$\Delta\alpha$	$\Delta\theta$
6	3rd and 4th	Nonconstant	12.8	-2.9
6	3rd and 4th	Nonexistent	15.1	1.3
7	3rd, 4th, and 5th	Nonconstant	11.5	-4.7
7	3rd, 4th, and 5th	Nonexistent	18.8	0.2

when tracking the average leg and body rotation for both gaits for two cases at 15 Hz. As shown in Tab. 7.1, the nonexistent gait results in an average positive body rotation and larger leg swing compared to the nonconstant gait.

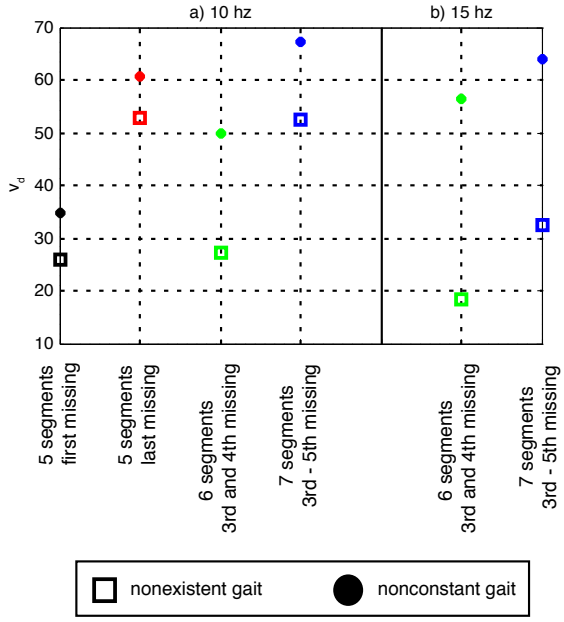

Figure 7.8: Percent decrease in speed when static stability is compromised.

7.6 Effect of location of missing legs

Example cases were used to examine effects of the location of missing legs on v_d. If a particular segment or group of segments cause more of a decrease in speed when broken, it may be beneficial to have sensors on only those segments to alter the gait and avoid performance degradation or critical failure.

Fig. 7.9 shows that the location of the missing legs along the length of the body, has no noticeable effect on v_d for millirobots with 5, 7, and 10 segments across the entire range of frequencies, except when the last segment is missing. Conversely, the three-segment millirobot presents a unique problem in terms of location of missing legs. As the first and last segments are in phase, if the middle segment loses both legs, catastrophic failure occurs unless the gait is altered to make the first and last segments 180 degrees out of phase. This causes a dependency on location of missing legs for the three-segment millirobot, but not for millirobots with five or more segments.

While the location of missing legs along the length of the body did not affect millirobot speed, the number of segments in a row with missing legs did have a significant effect on performance. As can be seen in Fig. 7.11, even with the same number of missing legs, having more broken segments in a row causes a more significant decrease in speed, independent of drive signal. When legs are missing, the body tends to sag due to the passive body compliance. This problem is exacerbated when many legs in a row are missing as the serial compliance in the body causes increased deformation. In addition to loading segments adjacent to the group of missing legs, the resulting body curvature also causes segments further from the group of missing legs to lift off the ground, thus decreasing their contribution to forward locomotion. This is illus-

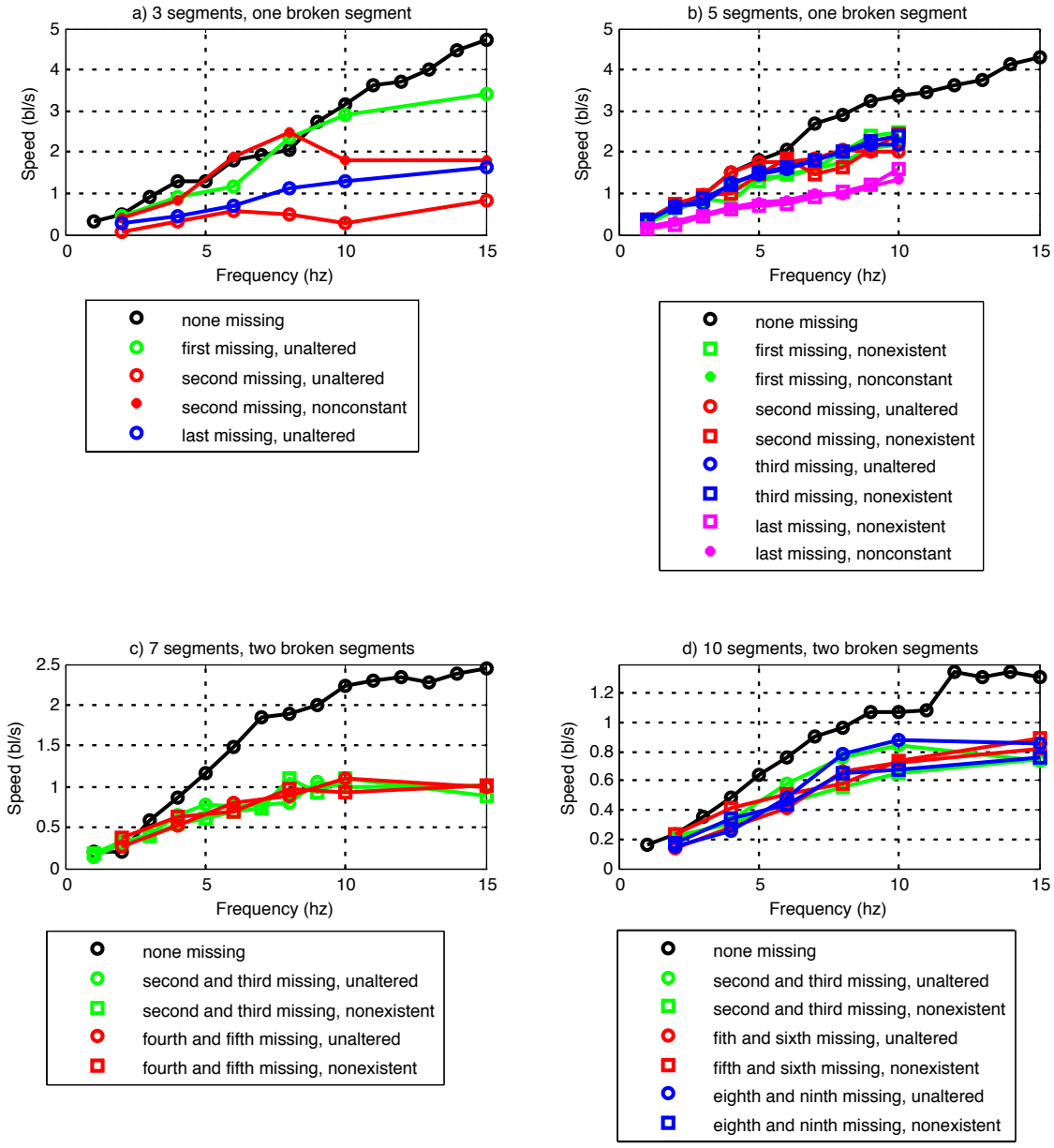

Figure 7.9: Speeds for 3, 5, 7, and 10 segment millirobots showing that the location of missing legs along the length of the body does not affect performance for similar numbers of missing legs. The exception is with the last segment.

trated in Fig. 7.10. The only observed exception to this was with six segments when there was no noticeable difference in speed between the third and fifth segments legs missing and the third and fourth segments legs missing using the nonexistent gait.

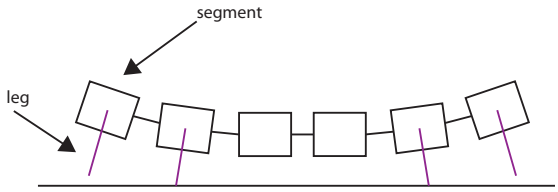

Figure 7.10: An illustration of the resulting body curvature when groups of segments have missing legs.

A 10 segment millirobot has shown that with four or more segments in a row missing, the body sags to the extent that segments with missing legs touch the ground. While the static stability analysis in Sec. 7.1 suggests that millirobots with 11 or more segments can have four broken segments in a row while still maintaining static stability, the off-axis compliance of the body is the limiting factor. While it has been shown that a passively compliant body allows for locomotion enhancing undulations and the off-axis compliance may help in preserving ground contact of all legs when traversing rough terrain, there may be a trade-off when considering cases when many legs are missing.

7.7 Conclusion

This chapter describes the effects of mechanical redundancy as a method for robustness to failures in miniature underactuated robots. A kinematic analysis showed that $floor(0.5(n-3))$ segments in a row can be damaged before an n-segment mil-

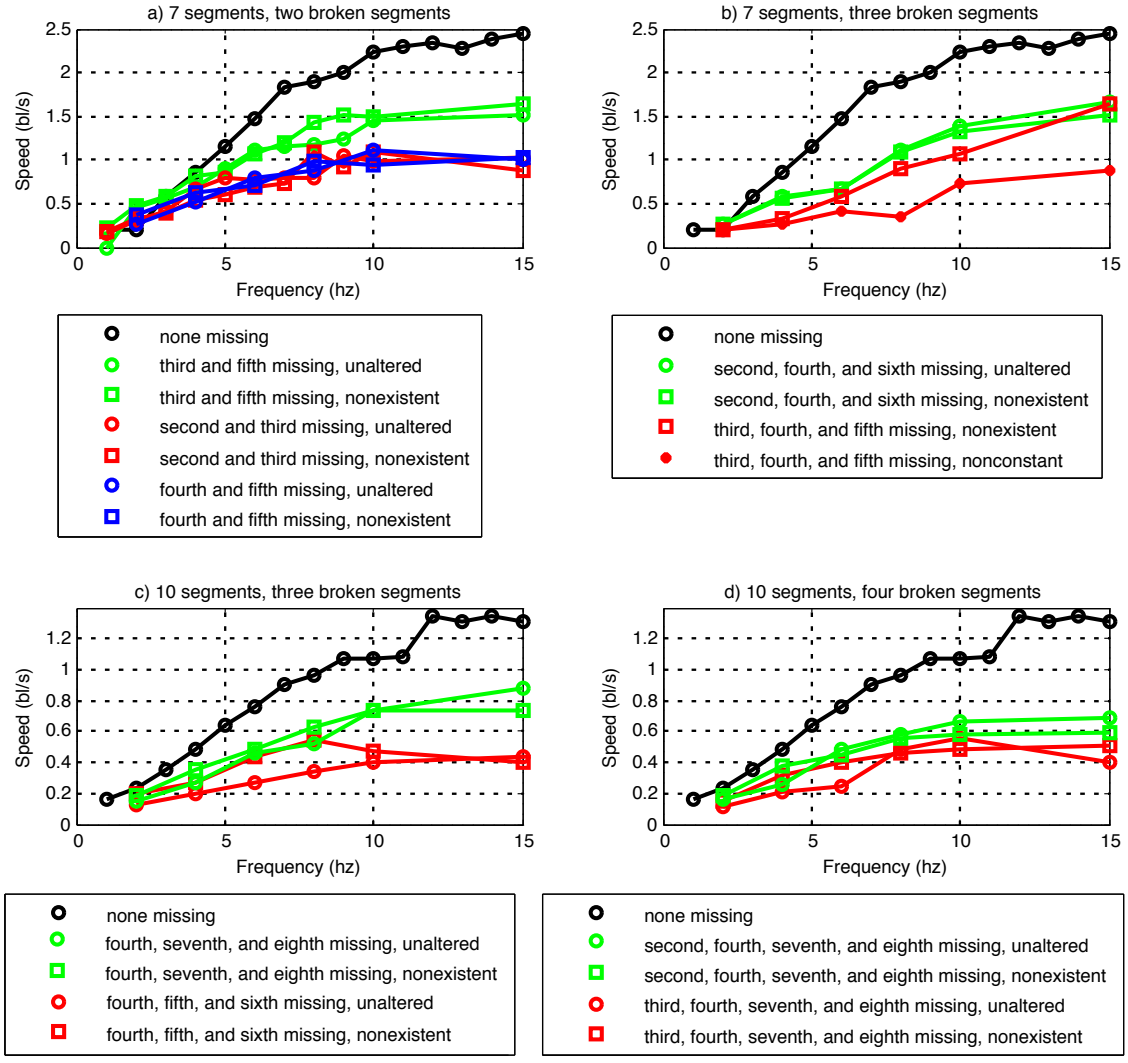

Figure 7.11: Speeds for 7 and 10 segment millirobots illustrating that multiple segments in a row missing (red and blue), as opposed to missing segments distributed along length of body (green), results in a greater decrease in speed compared to baseline speeds (black).

lirobot loses static stability using the optimal undulatory gait. While the speed of forward locomotion decreased as legs were removed, there was a graceful degradation without altering the gait. Robustness of locomotion to leg failures didn't increase as a function of nominal legs when considering the percentage of legs lost; however, millirobots with six or more segments were found to experience less of a decrease in speed than three or five segments when considering the absolute number of missing legs. If the expected number of failures is a sublinear function of the nominal number of segments, there is an advantage of having more legs.

It was found that when less than $n_{critical}$ segments in a row were missing and static stability was conserved, there was no benefit to increasing the phase between working segments to account for the missing leg. For cases where static stability was compromised, the nonexistent gait resulted in better performance over the nonconstant gait; however, the off-axis compliance in the millirobot limited the number of legs that could be missing in a row even when the gait was altered.

In future work, it may be interesting to implement machine learning for the millirobot to find new optimal gaits for when legs are missing. While this might not be practical to do autonomously in real-time, the learned gaits may show trends that could be used to produce improved results over the nonexistent gait shown here.

Chapter 8

Obstacle traversal

While the development of legged robots has been partially motivated by the ability to traverse rough terrain with more ease than systems with wheels, the problem of locomotion in unstructured terrains remains challenging and largely unsolved. Some strategies for larger robots have focused on using sensing and control strategies to navigate obstacles by finding stable footholds, often in a follow-the-leader fashion [48], [68]. This is popular for systems with very little physical compliance [12], [40].

Rather than directly controlling foot placement on rough terrain, legged robots have also benefitted from passive structures. Similar to mechanical stabilization in cockroaches running over rough terrain [58], efforts have explored compliant legs to maintain stability and speed [36], [25]. Other large robots have implemented directional spines inspired by those that allow spiders and cockroaches to run effortlessly over mesh surfaces [56]. Passive strategies are particularly important for miniature robots, which tend to lack sophisticated sensing and control but often need to traverse obstacles a significant percentage of their body height. These include body-supported

climbing [39] and leg compliance [8].

Centipedes, which often find caves and other rough terrain as their natural habitats, are well-suited for obstacle traversal and may exhibit benefits over rigid body hexapods, which most miniature legged robots are modeled after. Their flexible bodies allow them to morph to rough terrain to reduce loss of foot contact, while their many legs provide added stability. Unfortunately, no miniature robots and very few legged macro-scale robots (i.e. masses on the order of kilograms) have taken inspiration from centipedes to demonstrate locomotion over rough terrain [38]; however, robots with tracks [42] and Whegs [11] have been shown to benefit from active rotational joints located in the body.

This work aims to answer the following questions related to body morphology and obstacle traversal for a miniature robot with a passively compliant body:

1. Which gaits are best for navigating obstacles for this millirobot?

2. What mechanisms can be used to increase the height of obstacles that millirobots can navigate?

3. Does having more legs and/or a passively flexible body help with obstacle traversal in terms of locomotion speed and maximum height of obstacles this robot is able to traverse?

The goal of this work was not to determine if having a flexible body is beneficial for all robots on all terrain, but rather to determine if a flexible body and many legs help this particular robot traverse step obstacles of varying heights. These questions are answered via experiments for millirobots with flexible and rigid bodies with 6 and 12 legs (Sec. 8.5). The best gait, payload capacity, and operating range for rough

terrain locomotion were determined, while claws to assist this millirobot traverse obstacles half the body height were designed and implemented (Sec. 8.3-8.4). Finally, the various body morphologies were tested on additional obstacles, including those shorter in length than the body of the robot and stair-like obstacles (Sec. 8.6).

8.1 Experimental setup

Most of the experiments presented here used obstacles of varying height (1.98 to 6.20 mm) placed on flat terrain. Millirobots with different body morphologies were run, open loop, over the obstacles for a range of frequencies. The speed of locomotion was calculated starting from when the first foot touched the obstacle and ending with when the last leg left the lower surface. If the robot made no progress in traversing the obstacle after four seconds, the trial was considered a failed attempt. Due to variation between trials, most trials were verified using a second robot and similar trends were found. Two data points were averaged for each case in Sec. 8.5, and 10 trials were averaged for the cases in Sec. 8.6 due to increased variation in trials.

This robot is of the same design used for the experiments in Chapters 5-7, with added stoppers placed between segments to prevent the passive backbone from collapsing completely when the robot collides with an obstacle. These do not affect undulations on flat terrain. For comparisons between flexible and rigid body robots with the same number of legs, the backbone stoppers were replaced with rigid supports of similar mass to eliminate the flexibility in the body. This allowed the same robots to be used for a comparison between rigid and flexible body morphologies to eliminate any difference in results due to fabrication defects or performance degra-

dation over time. Note that the millirobots were not optimized for backbone/hip stiffness. The off-axis backbone stiffness for the flexible backbone components along the length of the robot body was measured by applying force to the end of backbone components (Fig. 8.1). Two trials were performed, and a linear fit to the data gave a stiffness of 1.9 g/mm.

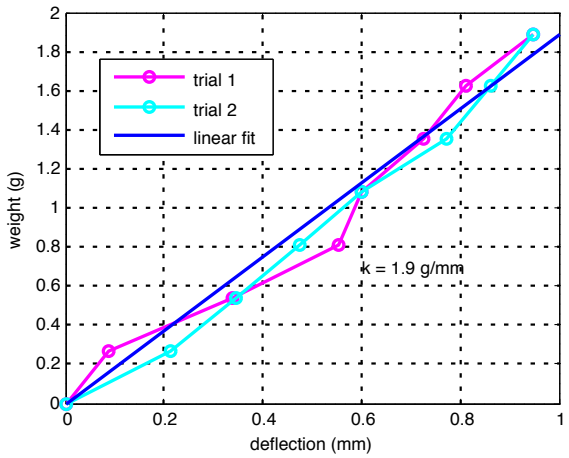

Figure 8.1: Off-axis backbone stiffness (i.e. along length of body) for flexible body.

8.2 Operating range

Tests were performed for frequencies ranging from 1-15 Hz. When tracking the underside of each segment for the different body morphologies on flat terrain, the body and hip joint compliance was found to produce dynamic effects in the transverse plane, causing the robot to exhibit oscillations about the equilibrium resting height of the COM. The frequency and amplitude of these oscillations varied according to robot size and gait, ranging from 6 mm peak-to-peak using the alternating gait at 5 Hz for the six-segment flexible body millirobot to only 3 mm for the rigid body

version. In all cases, the amplitude of COM oscillation was maximum in the range from 5-10 Hz and significantly reduced at 15 Hz. This was also found to be the range the millirobots were most successful at navigating obstacles.

8.3 Gaits

It was described in Chapter 3 that the best gaits for this n-segment robot with a passively flexible body use a phase difference of $\frac{360}{n-1}$ degrees between adjacent segments and a constant hip torque to produce passive undulations. The studies comparing these two gaits focused on the horizontal plane motion; here, studies are performed to investigate which gait results in the best millirobot performance in terms of leg lifting height, payload capacity, and obstacle traversal.

8.3.1 Payload capacity

To determine leg lifting height as a function of payload for the alternating and undulatory gait, weights were added incrementally to a five-segment robot being driven quasi-statically at 1 Hz on flat terrain. The feet on one side of the robot were tracked over a series of six steps using motion analysis software. The foot profile is not a square wave, but rather has maximum and minimum points caused by the shifting of the COM at low frequencies. The average and maximum leg lifting height is shown in Fig. 8.2. It will be shown in Sec. 8.3.2 that the robot can actually walk over obstacles taller than the maximum leg lifting height of the first segment, possibly due to the force of posterior segments.

The maximum and mean leg lifting height varied significantly along the length

of the body and between gaits. The uneven number of legs off the ground on the same side of the body causes the different profiles shown in Fig. 8.2. It is expected that as the number of segments increases, the difference between leg lifting heights among segments will decrease. It is also hypothesized that the alternating gait results in higher leg lifting heights due to the off-axis compliance in the backbone allowing segments to sag as more legs in a row are off the ground on the same side of the body for the undulatory gait.

Fig. 8.2 shows that the robot can hold up to 1.35 grams, or an additional 123 percent of the body weight, while still maintaining forward locomotion on flat terrain. This gives an indication of payload capacity for future autonomy.

8.3.2 Obstacle traversal

As expected, based on the leg lifting heights found in Sec. 8.3.1, Fig. 8.4 shows that while the undulatory gait is faster on flat terrain for 1-10 Hz, the alternating gait is faster when climbing up onto obstacles over the range of frequencies and allows the millirobot to locomote over obstacles that the undulatory gait cannot, particularly at higher frequencies. Additionally, for short obstacles at 7 and 10 Hz, the alternating gait performs better over obstacles than on flat terrain, possibly due to the unwanted oscillations observed on flat terrain being reduced when moving over obstacles.

At higher frequencies, such as 15 Hz, there is a significant decrease in speed for obstacles taller than 3.42 mm for the alternating gait. It was observed that at higher frequencies, the leg lifting height is reduced to less than the obstacle height and the amplitude of oscillation of the COM is significantly reduced, causing the millirobot

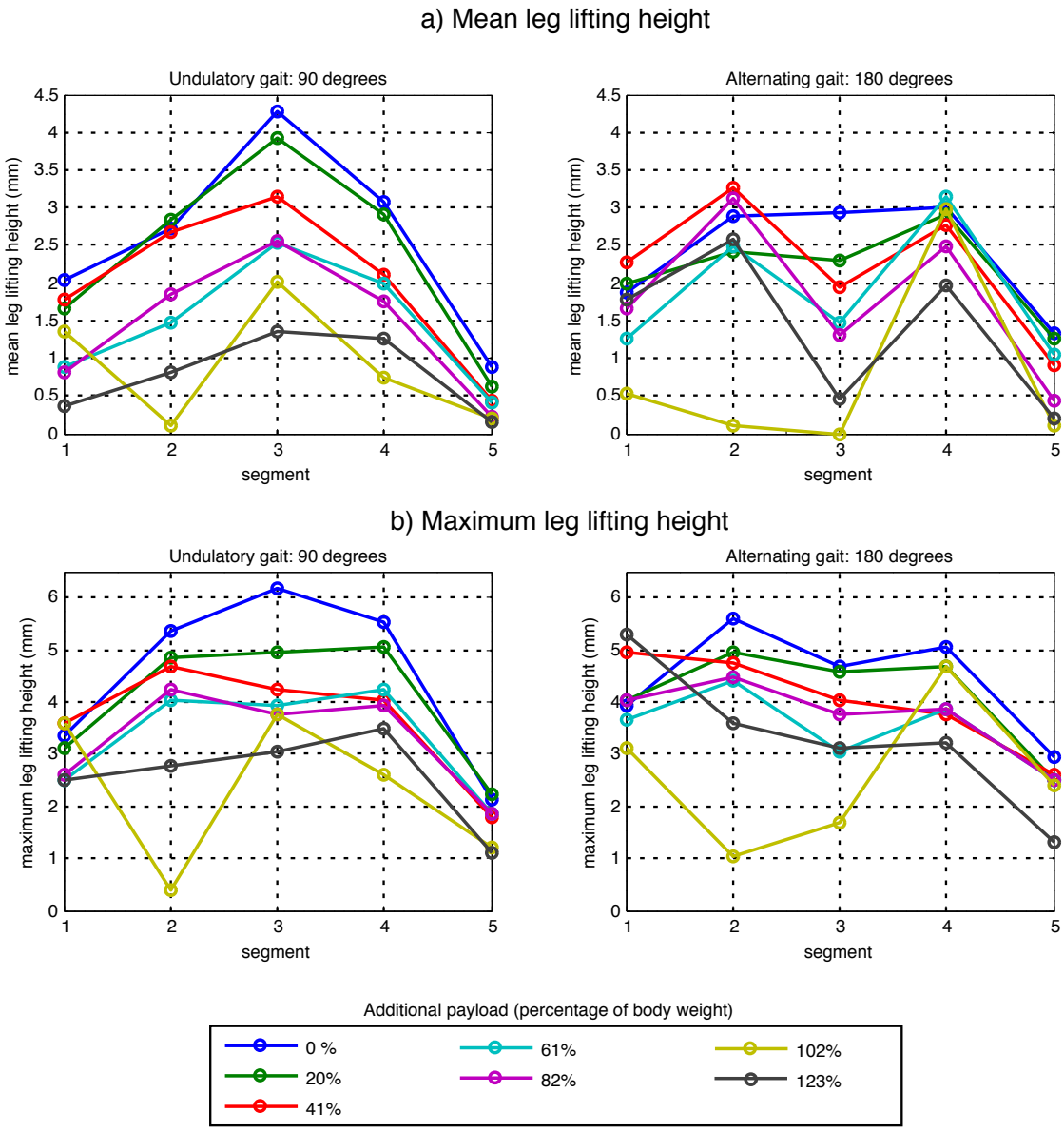

Figure 8.2: a) Mean and b) maximum leg lifting height for a five-segment millirobot for undulatory and alternating gaits with 225 mg weights.

to first run into the obstacle, exhibiting a pause in locomotion until the millirobot is able to push itself over the obstacle. For the undulatory gait, the robot is unable to navigate obstacles taller than 1.98 mm at 15 Hz unassisted due to the reduced leg lifting height. The alternating gait results in larger amplitude oscillations of the COM in the transverse plane (approximately 6 mm at 5 Hz compared to 4 mm), possibly due to all legs pushing off the ground at once. This results in enhanced locomotion over obstacles. Additionally, the oscillations of the COM for the alternating gait for 5, 7, and 10 Hz occur at the stepping frequency, while the undulatory gait exhibits oscillations at half the stepping frequency. A better understanding of this phenomenon should be the focus of future work.

8.4 Climbing mechanisms

A goal of this work was to find mechanisms that could increase the height of obstacles the millirobot is able to overcome. Due to the limited actuator force/displacement, which affects leg lifting height, additional mechanisms were added to improve locomotion over rough terrain. Given the difficulty of predicting the types of terrain these robots will encounter a priori as well as obstacle locations in real-time, passive mechanisms were chosen rather than actively controlling body curvature and leg trajectories.

8.4.1 Claws

The first approach to facilitating locomotion over obstacles focused on integrating different claws onto the feet of a six-segment, flexible body millirobot to increase the

effective step height. The claws were laser-machined using 2 mil stainless steel and attached to the feet using a temporary adhesive for easy removal. An illustration of different claw types as well as an indication of their effectiveness at traversing obstacles is given in Tab. 8.1.

Table 8.1: Claw effectiveness at enabling traversal of 6.20 mm tall obstacles. Note that '1st' refers to the millirobot being capable of lifting the legs of the first segment onto the obstacle, '4th' refers to the millirobot lifting all legs up until the 4th segment onto the obstacle, etc.

Claw type	None		First Segment		All feet		All feet		All feet	
Phase (deg)	180	72	180	72	180	72	180	72	180	72
5 Hz	No	No	Yes	Yes	Yes	Yes	Yes	Yes	N/A	Yes
7 Hz	No	No	Yes	4th	Yes	Yes	Yes	Yes	N/A	Yes
10 Hz	No	No	No	No	Yes	3rd	Yes	No	N/A	No
15 Hz	No	No	1st	No	Yes	2nd	Yes	No	N/A	No

Since the tips of the claws are taller than the feet, they are able to grip the top of obstacles taller than the leg lifting height. Once the tips of the claws are on the top of the obstacle, the angled surface of the claws enables the robot to slide the feet onto the obstacle as it moves forward.

The claws most successful at enabling the millirobot to climb over obstacles 6.20 mm in height for a range of frequencies had two angled surfaces (column two of Tab. 8.1). When the claws catch on the top of the obstacle, the hip joints and piezoelectric actuators are deflected, reducing their ability to lift the feet. This means the legs have to slid over the obstacle. The ratchet-like claws reduce the ability to slide and require the robot to lift them off the surface to advance, making them ineffective.

8.4.2 Angled bracket

It was observed that when the millirobot attempts to navigate obstacles taller than the leg lifting height, it runs into the obstacle, and the rear segments push the first segment over the obstacle after a short pause. The blunt face of the robot reduces the effectiveness of this, so to facilitate the first segment sliding over the obstacle, an angled bracket was added to the front of the robot. An angled face was previously demonstrated in body-supported locomotion over obstacles in work by Kohut [39]. The impulse force imposed on the robot as it contacts an obstacle is perpendicular to the face of the robot, so an angled surface results in a vertical force component to push the robot over an obstacle.

It was found that the claws enabled the millirobot to climb over 6.2 mm tall obstacles twice as fast at 7 Hz compared to the bracket. Additionally, the angled bracket was unsuccessful at frequencies higher than 7 Hz, while the claws allowed obstacle traversal using the alternating gait up to 15 Hz. The bracket was successful at assisting the first segment at traversing obstacles; however, in many cases, rear legs would get stuck and either cause the robot to slow down or not climb over the obstacle.

8.5 Single step obstacles

It has been hypothesized that an advantage of centipedes, which have many legs and a flexible body, over cockroaches with six legs and a relatively rigid body is the ability to morph to surfaces and more easily navigate rough terrain. Additionally,

with more ground contact points, myriapods are thought to be more stable than robots with fewer legs. To test this hypothesis, the following body morphologies were used and are shown in Fig. 8.3:

1. six segments, flexible body, 6 cm in length
2. six segments, rigid body, 6 cm in length
3. three segments, flexible body, 2.5 cm in length
4. three segments, rigid body, 2.5 cm in length
5. three segments, rigid body, 6 cm in length

The segment width to length ratio is 4:1, which allows many segments to be added while not excessively growing the length of the millirobot. While this gives millirobots with five or more segments a sufficiently large tripod of stability, with only three segments, the short body length and large leg swing angle causes the COM to exit the tripod of stability. For this reason, in addition to testing a three-segment millirobot with a 2.5 cm body length, a three-segment robot with a body length equal to that of the six-segment robot was also tested.

For single step obstacles of varying height, the absolute speed (Fig. 8.4) and decrease in speed compared to locomotion on flat terrain (Fig. 8.5) were used as performance metrics. Note that for 6.20 mm obstacles, claws were added to assist obstacle traversal.

While the three-segment rigid body millirobot was faster than the equivalent with a flexible body, it was still slower at climbing up onto obstacles for most frequencies

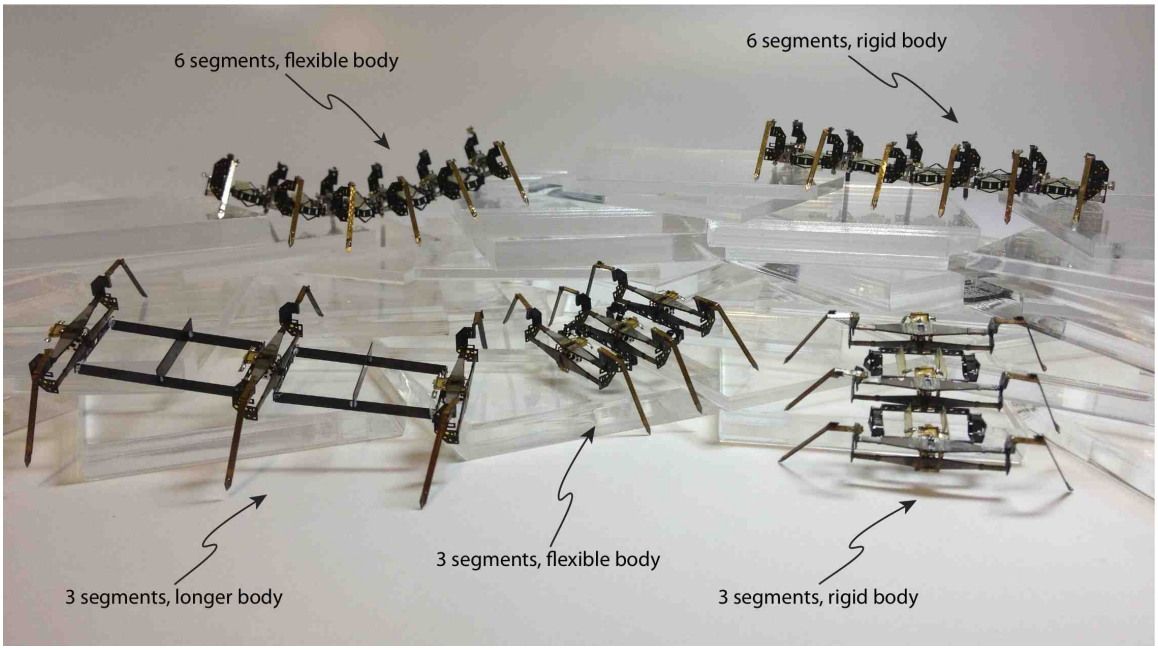

Figure 8.3: Photo of body morphologies used in these experiments: six-segment flexible body, six-segment rigid body, three-segment flexible body, three-segment rigid body, and three-segment longer body.

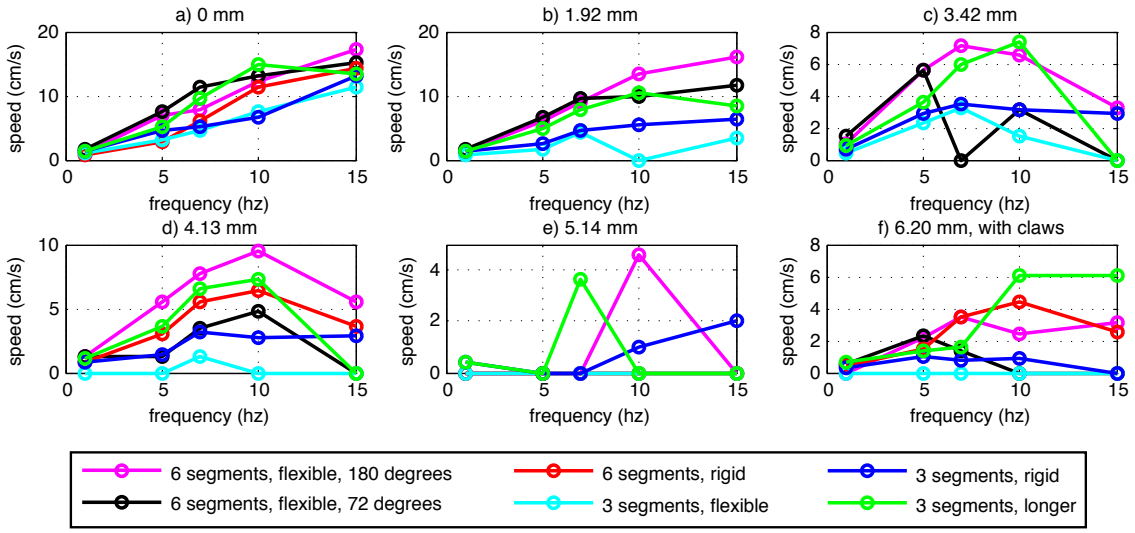

Figure 8.4: Absolute speed on a) flat terrain and over single step obstacles between b) 1.92 mm and f) 6.20 mm (with claws).

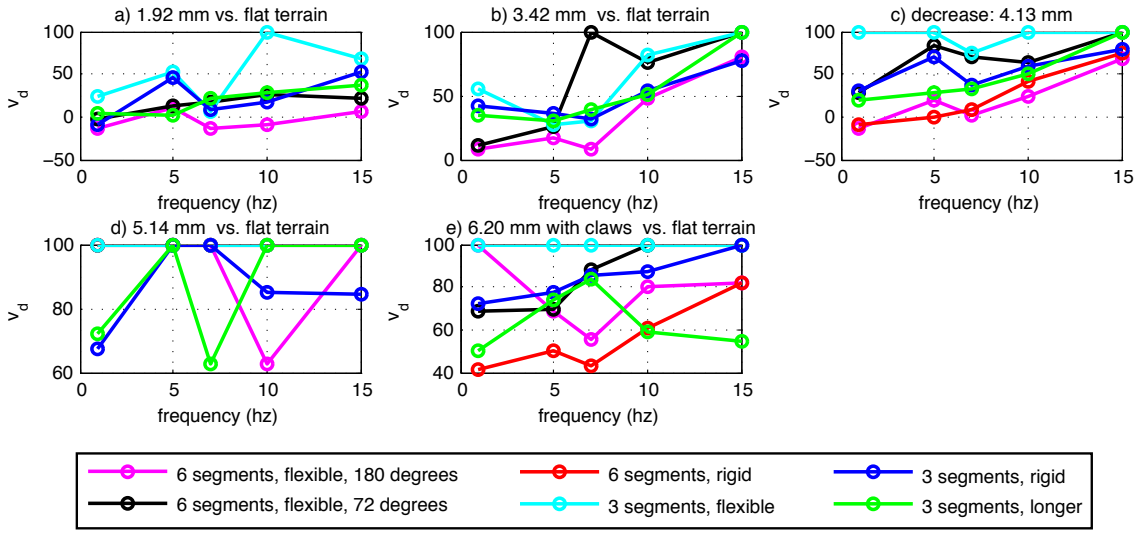

Figure 8.5: Decrease in speed compared to flat terrain for obstacles a) 1.92 mm to e) 6.20 mm (with claws) in height.

tested when compared to a six-segment, flexible body millirobot using the alternating gait. The decrease in speed for the three-segment rigid body millirobot over obstacles compared to flat terrain is also higher than most other body morphologies tested, except the 6 segment flexible body millirobot with the undulatory gait and the three-segment flexible body millirobot.

The fact that the longer bodied robots were faster can be explained in terms of millirobot stability and COM shifting during locomotion. Fig. 8.6 shows how the COM of three and six-segment millirobots shifts during locomotion. For three-segment millirobots, this causes the millirobot to tip back and forth, particularly at lower frequencies, resulting in body pitching angles up to 20 degrees and a height of 15 mm for the bottom of the first segment at 5 Hz. The three-segment millirobot struggles to pull the back legs over the obstacle, as a significant percentage of the weight of the millirobot is being placed on the back segment with the middle legs

on the obstacle and the front legs suspended (Fig. 8.7). This was a common mode of failure to traverse an obstacle for this body morphology. While this results in slower locomotion, this pitching allows the front legs to lift higher than those for a six-segment millirobot, allowing the three-segment rigid body robot to traverse 5.14 mm obstacles (without claws) at a larger range of frequencies than the six-segment millirobot. The three-segment millirobot with a longer body was found to not exhibit this severe pitching due to having a larger tripod of stability, increasing the speed of locomotion over most obstacles; however, this body morphology has negative effects with the obstacles in Sec. 8.6 and experiences periods of time when the middle legs lose ground contact.

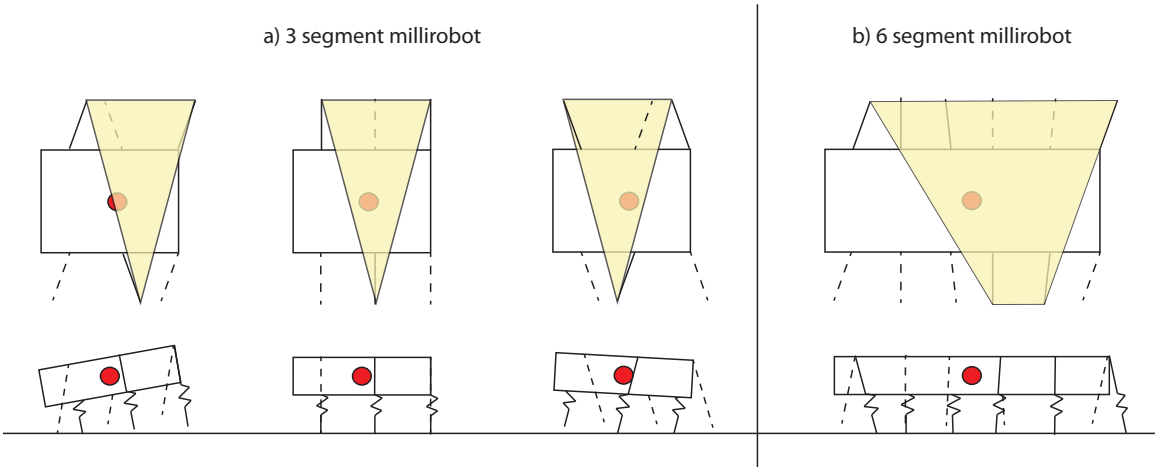

Figure 8.6: Illustration of top and side view of COM shifting for a) three-segment and b) six-segment millirobots during flat terrain locomotion.

The six-segment millirobot exhibited smooth locomotion over more obstacles compared to the three-segment rigid body millirobot due to increased legs and body length preventing pitching. For obstacles 4.13 mm in height, the six-segment flexible body millirobot using the alternating gait was usually faster and experienced less of

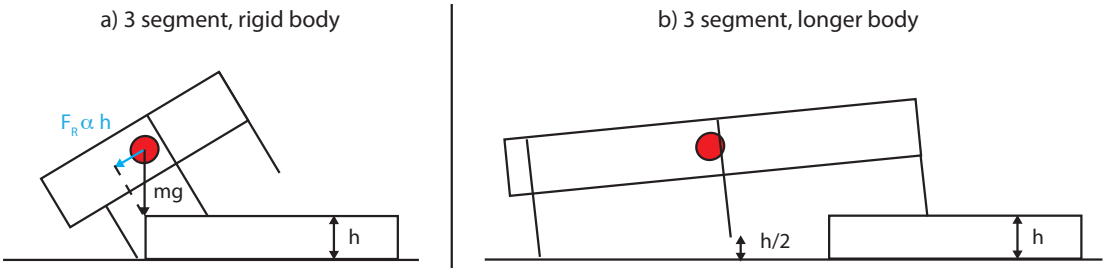

Figure 8.7: Illustration of a) force increase on back legs of three-segment millirobot, F_R, as obstacle height, h, increases and b) reduction in leg lifting height for three-segment millirobot with longer body.

a decrease in locomotion compared to the six-segment millirobot with a rigid body; however, for obstacles 6.20 mm in height, the rigid body robot was more successful. This is possibly due to the compression of the flexible body reducing the impact force against the obstacle, which is more important for taller obstacles where the millirobot is unable to lift the legs higher than the obstacle. This is discussed further in Sec. 8.6.

8.6 Stairs and short obstacles

In addition to testing obstacles with a single step input, obstacles 6.20 mm tall but only 2 cm in length (i.e. shorter than the body length of the six-segment robot) and stairs with 4.13 mm step heights were tested. These are illustrated in Fig. 8.8(a).

As can be seen in Fig. 8.8, the 6 segment flexible body millirobot was the most successful at navigating these obstacles in terms of least number of failures and highest speeds. Fig. 8.9(a) shows the body of the robot morphing to the surface to maximize the number of legs in contact with the ground. This resulted in smooth locomotion over the obstacles. Conversely, for the remaining body morphologies, some trials resulted in the millirobot unable to traverse the obstacle (Fig. 8.8) or reduced speeds

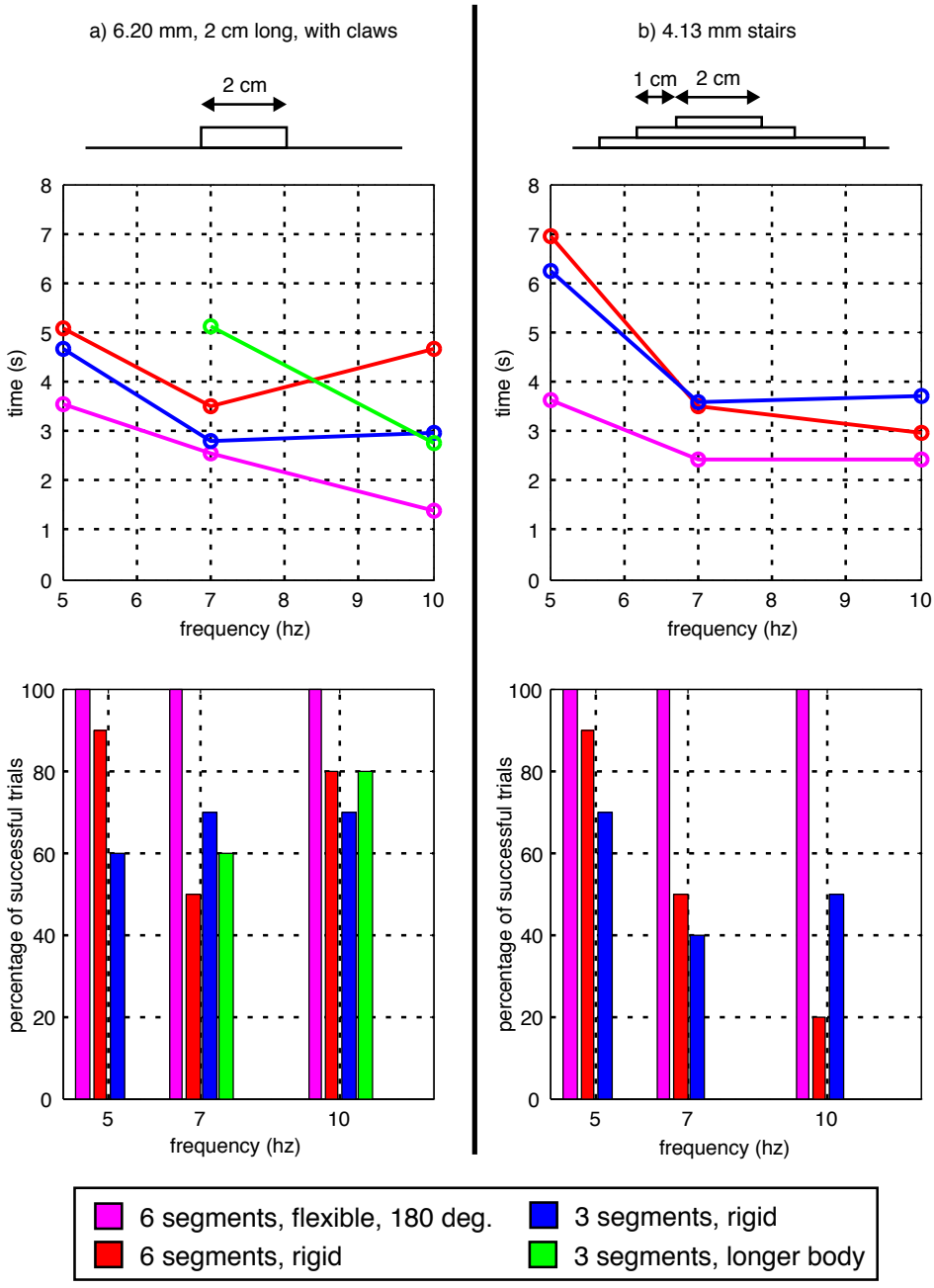

Figure 8.8: Speeds and success rates for centipede millirobots of differing body morphologies traversing a) 6.20 mm tall and 2 cm long obstacle and b) stairs with 4.13 mm step heights.

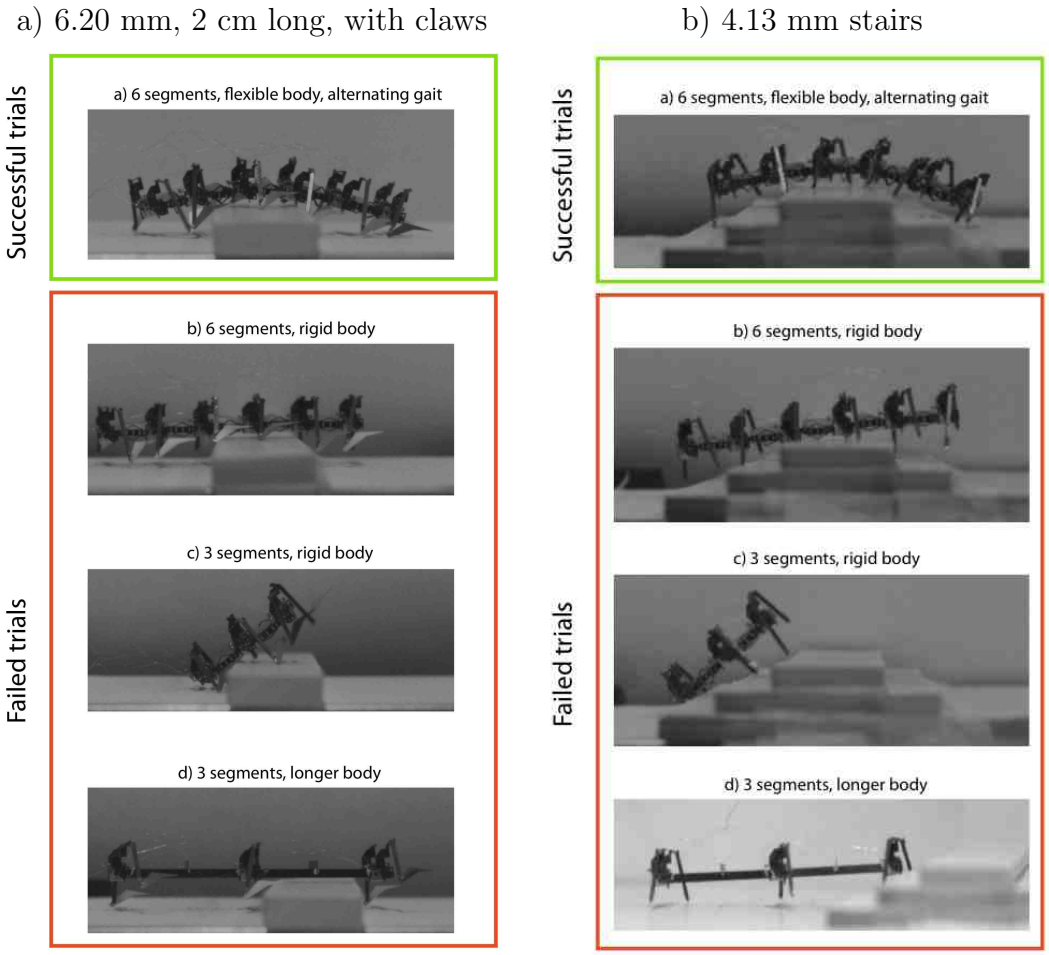

Figure 8.9: Modes of success and failure for different body morphologies over a) 6.20 mm tall and 2 cm long obstacle and b) stairs with 4.13 mm step heights.

of locomotion. Fig. 8.9(b-d) shows the typical modes of failure.

As expected, the six-segment rigid body robot became stuck when the first two and last two segments lost ground contact due to the obstacles having surfaces shorter than the body length. The middle legs were required to support the weight of the robot and unable to push the robot forward. The three-segment rigid body robot generally struggled lifting the back legs onto the obstacle due to the height of the obstacles preventing the millirobot from tipping forward and most of the weight being placed on the rear legs as described in Sec. 8.5. This occasionally had the catastrophic consequence of tipping over backwards due to the angle of inclination.

Finally, the three-segment millirobot with a longer body was the least successful at traversing these obstacles (Fig. 8.8). This was particularly apparent for the stairs. When the front legs of the millirobot are on an obstacle, the middle legs are suspended by half the obstacle height. As these legs form the center of the tripod of stability, the robot tips, reducing the front and rear leg lifting height by half the obstacle height as illustrated in Fig. 8.7. While for single step inputs in Sec. 8.5 it is able to slide over the obstacle with the front legs, in this case, it is unable to move forward as the front legs become stuck on the next step.

Note that while the six-segment flexible body millirobot performed better than the rigid body equivalent on these obstacles, this sampling of obstacle types does not encompass all those found in natural environments. For example, it is hypothesized that for narrow valleys in terrain, the rigid body millirobot may perform better by spanning the length of the crevice, while the flexible body millirobot may allow segments to dip into the crevice and become stuck or slow down locomotion. This

millirobot, independent of body rigidity and number of legs, was also unable to traverse obstacles shorter in length than the spacing between legs (1 cm). Redesigning the robot underside to eliminate blunt faces on segments could alleviate this issue.

While the results in this section suggest many legs and out-of-plane body flexibility assists in obstacle traversal, the extent to which the horizontal plane body flexibility assists is debatable. Qualitative observations of an eight-segment flexible body millirobot indicate the serial compliance of the flexures that allow relative segment rotation may decrease the impulse force exerted to push the millirobot over the obstacle. This force is proportional to the rate of decrease of velocity. The body compression upon impact results in a lower rate of decrease in velocity and possbily lower impulse force. Additionally, after impact, the body begins to rotate and the force vector from each segment is no longer directed perpendicular to the obstacle face as shown in Fig. 8.10. This phenomenon was not noticeable for the six-segment flexible body millirobot used in the previous tests, but is apparent as segment number and, therefore, serial compliance, increases. As the flexure rotation for straight-line undulatory gaits is typically less than 20 degrees, brackets to limit the amount of rotation of the flexures during obstacle collision but allow undulations during straight-line motion are suggested for future improvement.

A six-segment flexible body millirobot was also found capable of traversing gravel as shown in Fig. 8.11.

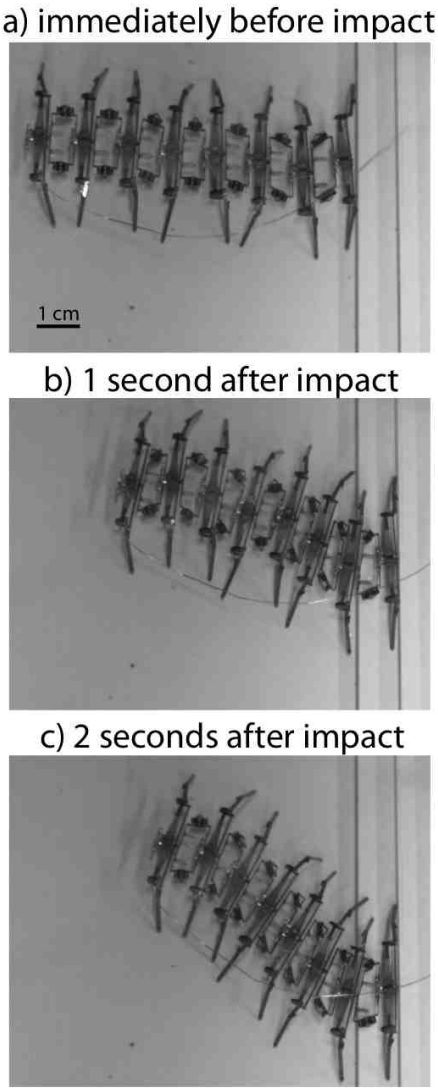

Figure 8.10: Frames of motion showing body curvature in eight-segment millirobot upon impact with 4.13 mm stairs.

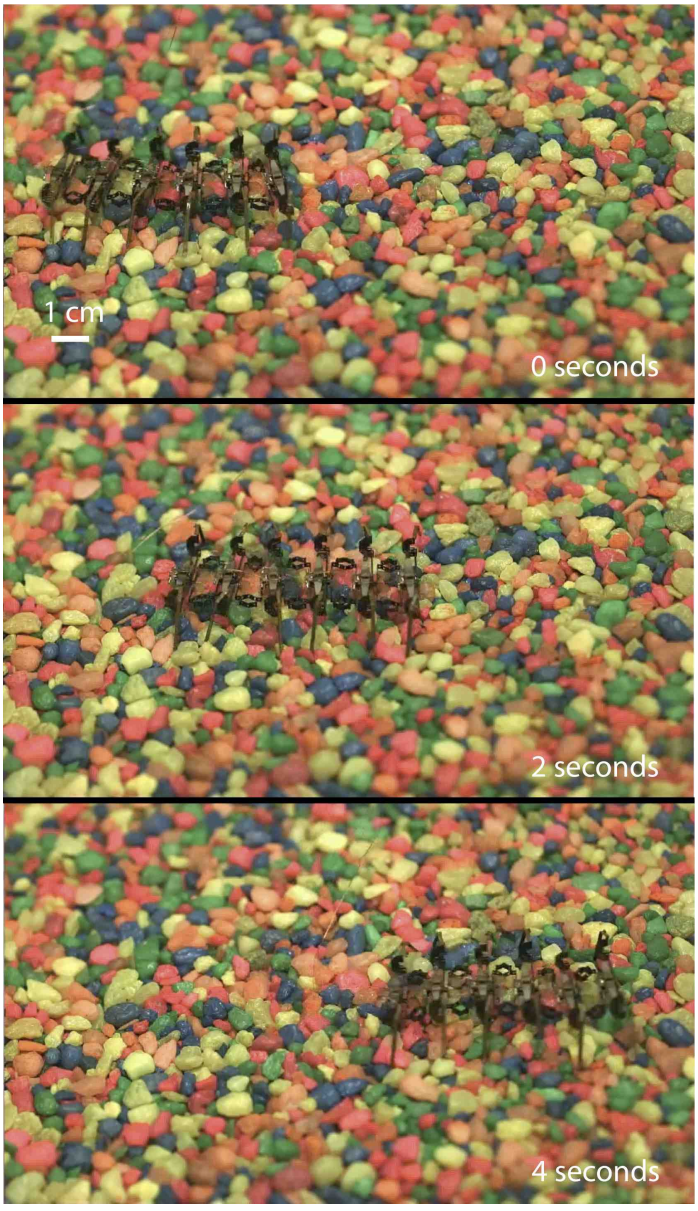

Figure 8.11: Frames of motion showing six-segment flexible body millirobot walking over gravel.

8.7 Conclusion

Claws were created to allow the millirobot to traverse obstacles up to half the body height while not affecting locomotion on flat terrain. Sec. 8.5 shows that the pitching of the three-segment millirobot increases front leg lifting height allowing traversal of obstacles 5.14 mm in height for a larger range of frequencies than the six-segment millirobot; however, it significantly reduces the speed of locomotion on flat terrain and over obstacles as compared to the six-segment millirobot, which exhibited more smooth transitions. Additionally, the flexible body millirobot was found to perform best over obstacles 4.13 mm in height, whereas the rigid body millirobot was more successful with obstacles 6.20 mm in height possibly due to a larger impulse force exerted by the rigid body. The results from Sec. 8.6 suggest that the off-axis body compliance assists in traversing obstacles shorter than the body length, while an increased number of legs allows the robot to maintain stability when traversing obstacles with steep inclines. Obstacle traversal is particularly important for miniature robots in swarm robotics applications, such as search and rescue and hazardous environment exploration, as terrain is often unpredictable and rough.

This is not a comprehensive study on locomotion over rough terrain; however, this does imply benefits of a compliant body and many legs, which motivates future work on finding an optimal amount of body flexibility and length and number of legs for different scenarios. Controlled body compliance may be achieved by adding flexures that allow out-of-plane body bending as opposed to relying on the off-axis compliance of the sarrus linkage and rotational backbone flexures. Finally, while the body compression upon obstacle impact seemingly detracted from locomotion,

this compression could be leveraged via the integration of passive intersegmental mechanisms that cause segment pitching to assist in obstacle traversal.

Chapter 9

Conclusion and Future Work

This thesis is an overall study on the design, fabrication, modeling, and locomotion of a millirobot inspired by the body morphology of centipedes. This millirobot employs a novel design with a passively flexible body capable of generating locomotion-enhancing body undulations representative of those found in nature. More importantly, this work shows that those undulations can be caused by the passive system dynamics and described fully by a horizontal plane model. The use of only two drive signals has allowed this millirobot to demonstrate a variety of maneuvers. Additionally, graceful degradation due to leg failures and superior performance over a selection of obstacles imply advantages of a centipede body morphology.

While there are certainly many ways to extend the work presented here, the main suggestions relate to biological studies, batch fabrication, and autonomy.

This millirobot succeeded at providing an understanding of myriapod locomotion at small scales; however, this effort would be greatly enhanced by studies on its biological counterpart. While undulatory gaits have been studied in actual centipedes,

many aspects of biological centipede locomotion remain a mystery, namely how they excel at effortlessly and quickly traversing uneven terrain. It can be argued that the major advances in the development of rigid body hexapod robots can be attributed to extensive studies performed on actual cockroaches and a similar methodology could be useful for miniature centipede robots. Hopefully the work presented here motivates these studies by demonstrating advantages of many legs and a flexible body.

The PC-MEMS process was used to fabricate this millirobot, with specific strategies being created to ease the layup of each segment and reduce manual alignment, including layered molds made of a tacky substrate and pin-aligned flexible circuitry. Pop-up fabrication has been demonstrated with other devices at this scale [59]; however, these techniques were not applied to this millirobot as the design was constantly changing over the course of this work. The future of this millirobot is dependent on the application of pop-up fabrication, including the integration of flexible circuitry into this process.

The millirobots used for the experiments in this thesis all featured an external power supply and controller. While it was possible to gain an understanding of centipede millirobot locomotion with a lightweight tether, autonomy is necessary for swarm robotics applications, which is the ultimate goal of miniature robots. Power and control electronics like those of a 1.7 g cockroach inspired robot with similar piezoelectric actuators [7] should be applied to this millirobot. The straight-line and turning strategies presented in Chapters 5 and 6, which reduce the number of drive signals necessary to control a millirobot with any number of legs to two, will facilitate this process, including the implementation of feedback control, and the experiments

in Chapter 8 give an indication of payload capacity.

Bibliography

[1] ©2011 IEEE. Reprinted, with permission, from K.L. Hoffman and R.J. Wood. Passive undulatory gaits enhance walking in a myriapod millirobot. *IEEE/RSJ International Conference on Intelligent Robots and Systems*, 2011.

[2] ©2012 IEEE. Reprinted, with permission, from K.L. Hoffman and R.J. Wood. Turning gaits and optimal undulatory gaits for a centipede-inspired millirobot. *IEEE RAS and EMBS International Conference on Biomedical Robotics and Biomechatronics*, 2012.

[3] C. Ades and E.N. Ramires. Asymmetry of leg use during prey handling in the spider *Scytodes globula* (Scytodidae). *Journal of Insect Behavior*, 15(4):563–570, 2002.

[4] B. Anderson, J. Shultz, and B. Jayne. Axial kinematics and muscle activity during terrestrial locomotion of the centipede Scolopendra heros. *Journal of Experimental Biology*, 198(5):1185–1195, 1995.

[5] P. Apontes and C.A. Brown. Between-sex variation in running speed and a potential cost of leg autotomy in the wolf spider *Pirata sedentarius*. *The American midland naturalist*, 154(1):115–125, 2005.

[6] D. Attenborough. Life in the undergrowth. 2005.

[7] A. Baisch, C. Heimlich, M. Karpelson, and R. Wood. HAMR3: An autonomous 1.7g ambulatory robot. *IEEE/RSJ International Conference on Intelligent Robots and Systems*, 2011.

[8] P. Birkmeyer, K. Peterson, and R.S. Fearing. DASH: A dynamic 16g hexapedal robot. *IEEE/RSJ International Conference on Intelligent Robots and Systems*, 2009.

[9] R. Blickhan and R.J. Full. Similarity in multilegged locomotion: bouncing like a monopode. *Journal of Comparative Physiology A: Neuroethology, Sensory, Neural, and Behavioral Physiology*, 173(5):509–517, 1993.

[10] J.C. Bongard and H. Lipson. Automated damage diagnosis and recovery for remote robotics. *IEEE International Conference on Robotics and Automation*, 2004.

[11] A.S. Boxerbaum, J. Oro, and R.D. Quinn. Introducing dagsi whegs: The latest generation of whegs robots, featuring a passive-compliant body joint. *IEEE International Conference on Robotics and Automation*, 2008.

[12] J. Buchli, M. Kalakrishnan, M. Mistry, P. Pastor, and S. Schaal. Compliant quadruped locomotion over rough terrain. *IEEE/RSJ International Conference on Intelligent Robots and Systems*, 2009.

[13] J.A. Cameron. Regeneration in *Scutigera* forceps. *Journal of Experimental Zoology*, 46(2):169–179, 1926.

[14] J.G. Cham, S.A. Bailey, J.E. Clark, R.J. Full, and M.R. Cutkosky. Fast and robust: Hexapedal robots via shape deposition manufacturing. *The International Journal of Robotics Research*, 21(10-11):869–882, 2002.

[15] V. Chen and R. Tedrake. *Passive dynamic walking with knees: a point foot model*. PhD thesis, Massachusetts Institute of Technology, 2007.

[16] C. Cho, B. Min, and D. Kim. A gait generation for an unlocked joint failure of the quadruped robot with balance weight. *Advances in Robotics*, pages 251–261, 2009.

[17] D.J. Christensen, U.P. Schultz, and K. Stoy. A distributed strategy for gait adaptation in modular robots. *IEEE International Conference on Robotics and Automation*, 2010.

[18] S.K.K. Chu and G.K.H. Pang. Comparison between different model of hexapod robot in fault-tolerant gait. *Systems, Man and Cybernetics, Part A: IEEE Transactions on Systems and Humans*, 32(6):752–756, 2002.

[19] from K.L. Hoffman ©2010 IEEE. Reprinted, with permission and R.J. Wood. Towards a multi-segment ambulatory microrobot.

[20] F. Delcomyn. Walking robots and the central and peripheral control of locomotion in insects. *Autonomous Robots*, 7(3):259–270, 1999.

[21] G.D. Edgecombe and G. Giribet. Evolutionary biology of centipedes (myriapoda: Chilopoda). *Annu. Rev. Entomol.*, 52:151–170, 2007.

[22] C. Ferrell. Failure recognition and fault tolerance of an autonomous robot. *Adaptive behavior*, 2(4):375–398, 1994.

[23] B.M. Finio, J.K. Shang, and R.J. Wood. Body torque modulation for a microrobotic fly. *IEEE International Conference on Robotics and Automation*, pages 3449–3456, 2009.

[24] H.C. Fründ. The occurrence and frequency of scars in centipedes. *8th International Congress on Myriapodology*, 10:269–275, 1992.

[25] Y Fukuoka, H Kimura, and A.H. Cohen. Adaptive dynamic walking of a quadruped robot on irregular terrain based on biological concepts. *The International Journal of Robotics Research*, 22(3-4):187–202, 2003.

[26] R.J. Full, R. Blickhan, and L.H. Ting. Leg design in hexapedal runners. *Journal of Experimental Biology*, 158(1):369–390, 1991.

[27] R.J. Full and M.S. Tu. Mechanics of a rapid running insect: two-, four-and six-legged locomotion. *Journal of Experimental Biology*, 156(1):215–231, 1991.

[28] C. Guffey. Leg autotomy and its potential fitness costs for two species of harvestmen (Arachnida, Opiliones). *Journal of Arachnology*, pages 296–302, 1998.

[29] C. Guffey. Costs associated with leg autotomy in the harvestmen *Leiobunum nigripes* and *Leiobunum vittatum* (Arachnida: Opiliones). *Canadian journal of zoology*, 77(5):824–830, 1999.

[30] K.L. Hoffman and R.J. Wood. Myriapod-like ambulation of a segmented microrobot. *Autonomous Robots*, 31(1):103–114, 2011.

[31] P. Holmes, R.J. Full, D. Koditschek, and J. Guckenheimer. The dynamics of legged locomotion: Models, analyses, and challenges. *Siam Review*, 48(2):207–304, 2006.

[32] A. Hoover, S. Burden, X.Y. Fu, S. Sastry, and R. Fearing. Bio-inspired design and dynamic maneuverability of a minimally actuated six-legged robot. *IEEE International Conference on Biomedical Robotics and Biomechatronics*, 2010.

[33] A.M. Hoover, E. Steltz, and R.S. Fearing. RoACH: An autonomous 2.4 g crawling hexapod robot. *IEEE/RSJ International Conference on Intelligent Robots and Systems*, 2008.

[34] B. Jimenez and A.J. Ikspeert. Centipede robot locomotion. Master's thesis, Ecole Polytechnique Federale de Lausanne, 2007.

[35] D.L. Jindrich and R.J. Full. Many-legged maneuverability: dynamics of turning in hexapods. *Journal of experimental biology*, 202(12):1603–1623, 1999.

[36] O.Y. Kanner and A.M. Dollar. Optimization of coupling ratio and kinematics of an underactuated robot leg for passive terrain adaptability. *Proceedings of the ASME International Design Engineering Technical Conferences, Mechanisms and Robotics Conference*, 2012.

[37] M. Karpelson, G.-Y. Wei, and R.J. Wood. Milligram-scale high-voltage power electronics for piezoelectric microrobots. *IEEE International Conference on Robotics and Automation*, 2009.

[38] D. Koh, J. Yang, and S. Kim. Centipede robot for uneven terrain exploration: Design and experiment of the flexible biomimetic robot mechanism. *IEEE RAS and EMBS International Conference on Biomedical Robotics and Biomechatronics*, 2010.

[39] N.J. Kohut, A.M. Hoover, K.Y. Ma, S.S. Baek, and R.S. Fearing. MEDIC: A legged millirobot utilizing novel obstacle traversal. *IEEE International Conference on Robotics and Automation*, 2011.

[40] J.Z. Kolter, M.P. Rodgers, and A.Y. Ng. A control architecture for quadruped locomotion over rough terrain. *IEEE International Conference on Robotics and Automation*, 2008.

[41] V.L. Krishnan, P.M. Pathak, S.C. Jain, and A.K. Samantaray. Reconfiguration of four-legged walking robot for actuator faults. *Proceedings of the Institution of Mechanical Engineers, Part I: Journal of Systems and Control Engineering*, 226(1):11–26, 2012.

[42] B. Li, S. Ma, J. Liu, and Y. Wang. Development of a shape shifting robot for search and rescue. *IEEE International Safety, Security and Rescue Robotics, Workshop*, pages 31–35, 2005.

[43] N. Lobontiu, M. Goldfarb, and E. Garcia. A piezoelectric-driven inchworm locomotion device. *Mechanism and Machine Theory*, 36(4):425–443, 2001.

[44] S.M. Manton. Habits of life and evolution of body design in arthropoda. *Journal of the Linnean Society of London, Zoology*, 44(295):58–72, 1958.

[45] S.M. Manton and M.J.P. Harding. The evolution of Arthropodan locomotory mechanisms - Part 3. The locomotion of the Chilopoda and Pauropoda. *Journal of the Linnean Society of London, Zoology*, 42(284):118–167, 1952.

[46] L. Matthey, L. Righetti, and A.J. Ijspeert. Experimental study of limit cycle and chaotic controllers for the locomotion of centipede robots. *IEEE/RSJ International Conference on Intelligent Robots and Systems*, 2008.

[47] K. Mostafa, C.S. Tsai, and I. Her. Alternative gaits for multiped robots with leg failures to retain maneuverability. *International Journal of Advanced Robotic Systems*, 7(4):31, 2010.

[48] T. Niwa, S. Inagaki, and T. Suzuki. Locomotion control of multi-legged robot based on follow-the-contact-point gait. *ICCAS-SICE*, pages 2247–2253, 2009.

[49] B.T. Nohara and T. Nishizawa. An Optimal Working Function Based on the Energetic Cost for Myriapod Robot Systems: How Many Legs Are Optimal for a Centipede? *Journal of Vibration and Control*, 11(10):1235, 2005.

[50] A.O. Pullin, N.J. Kohut, D. Zarrouk, and R.S. Fearing. Dynamic turning of 13 cm robot comparing tail and differential drive. *IEEE International Conference on Robotics and Automation*, 2012.

[51] R. Sahai, S. Avadhanula, R. Groff, E. Steltz, R. Wood, and R. Fearing. Towards a 3g crawling robot through the integration of microrobot technologies. *IEEE International Conference on Robotics and Automation*, 2006.

[52] U. Saranli, M. Buehler, and D.E. Koditschek. Rhex: A simple and highly mobile hexapod robot. *The International Journal of Robotics Research*, 20(7):616–631, 2001.

[53] J. Sastra, W.G. Bernal-Heredia, J. Clark, and M. Yim. A biologically-inspired dynamic legged locomotion with a modular reconfigurable robot. *DSCC ASME Dynamic Systems and Control Conference*, 2008.

[54] F. Seljanko. Proposal of recovery strategy from loss of leg incident for legged walking robot. *17th International Conference on Methods and Models in Automation and Robotics*, 2012.

[55] M. Sfakiotakis and D.P. Tsakiris. Undulatory and pedundulatory robotic locomotion via direct and retrograde body waves. *IEEE International Conference on Robotics and Automation*, 2009.

[56] J.C. Spagna, D.I. Goldman, P.C. Lin, D.E. Koditschek, and R.J. Full. Distributed mechanical feedback in arthropods and robots simplifies control of rapid running on challenging terrain. *Bioinspiration & biomimetics*, 2(1):9, 2007.

[57] D. Spenneberg, K. McCullough, and F. Kirchner. Stability of walking in a multilegged robot suffering leg loss. *IEEE International Conference on Robotics and Automation*, 2004.

[58] S. Sponberg and R.J. Full. Neuromechanical response of musculo-skeletal structures in cockroaches during rapid running on rough terrain. *Journal of Experimental Biology*, 211(3):433–446, 2008.

[59] P.S. Sreetharan, J.P. Whitney, M.D. Strauss, and R.J. Wood. Monolithic fabrication of millimeter-scale machines. *Journal of Micromechanics and Microengineering*, 22(5):055027, 2012.

[60] E. Steltz, M. Seeman, S. Avadhanula, and R.S. Fearing. Power electronics design choice for piezoelectric microrobots. *IEEE/RSJ International Conference on Intelligent Robots and Systems*, 2006.

[61] L.H. Ting, R. Blickhan, and R.J. Full. Dynamic and static stability in hexapedal runners. *Journal of Experimental Biology*, 197(1):251–269, 1994.

[62] J. Whitney, P. Sreetharan, K. Ma, and R.J. Wood. Pop-up book MEMS. *Journal of Micromechanics and Microengineering*, 21(11):115021–115027, 2011.

[63] J.P. Whitney. Piezoelectric actuator optimization matlab script. 2007.

[64] R.J. Wood. Design, fabrication, and analysis of a 3dof, 3cm flapping-wing mav. *IEEE/RSJ International Conference on Intelligent Robots and Systems*, 2007.

[65] R.J. Wood, S. Avadhanula, R. Sahai, E. Steltz, and R.S. Fearing. Microrobot design using fiber reinforced composites. *Journal of Mechanical Design*, 130(5):052304, 2008.

[66] R.J. Wood, E. Steltz, and R.S. Fearing. Nonlinear performance limits for high energy density piezoelectric bending actuators. *IEEE International Conference on Robotics and Automation*, 2005.

[67] R.J. Wood, E. Steltz, and R.S. Fearing. Optimal energy density piezoelectric bending actuators. *Sensors & Actuators: A. Physical*, 119(2):476–488, 2005.

[68] J.-M. Yang. Fault-tolerant gait planning for a hexapod robot walking over rough terrain. *Journal of Intelligent & Robotic Systems*, 54(4):613–627, 2009.

[69] J.M. Yang. Two-phase discontinuous gaits for quadruped walking machines with a failed leg. *Robotics and Autonomous Systems*, 56(9):728–737, 2008.

[70] Y. Zhang, M. Yim, C. Eldershaw, D. Duff, and K. Roufas. Phase automata: a programming model of locomotion gaits for scalable chain-type modular robots. *IEEE/RSJ International Conference on Intelligent Robots and Systems*, 2003.

Appendix A

Derivation of equations of motion

The horizontal plane dynamic equations are written in a modular fashion for a single segment, i, but can be expanded to a millirobot with n segments, where $i = 1, ..., n$. The equations of motion for the first and last segments differ in that there are only backbone connections to one other segment, eliminating half of the rotational and linear spring energy terms in the kinetic energy portion of the Lagrangian.

A.1 Kinematics

To derive the equations of motion, the kinematics for each segment are used. The coordinates of the rotational backbone flexures attached to the front of each segment (termed flexures a and b) are given by

$$x_{a,i} = x_{f,i} + c_{f,i} L_{leg} \cos(\alpha_i) + c_{f,i}(w_b - c_{f,i} w_{sa}) \cos(\theta_i) - c_{f,i} L_b \sin(\theta_i)$$
$$y_{a,i} = y_{f,i} + L_{leg} \sin(\alpha_i) + (w_b - c_{f,i} w_{sa}) \sin(\theta_i) + L_b \cos(\theta_i) \tag{A.1}$$

and

$$x_{b,i} = x_{f,i} + c_{f,i} L_{leg} \cos(\alpha_i) + c_{f,i}(w_b + c_{f,i} w_{sa}) \cos(\theta_i) - c_{f,i} L_b \sin(\theta_i)$$
$$y_{b,i} = y_{f,i} + L_{leg} \sin(\alpha_i) + (w_b + c_{f,i} w_{sa}) \sin(\theta_i) + L_b \cos(\theta_i) \tag{A.2}$$

written in terms of the state variables, θ_i (segment rotation) and α_i (leg rotation). $(x_{f,i}, y_{f,i})$ is the current stance foot position, $c_{f,i}$ indicates which foot is the stance foot, and w_b, w_{sa}, and L_{leg} are the segment width, sarrus linkage attachment point, and leg length, respectively. Additionally, the coordinates of the rotational backbone flexures attached to the posterior of each segment (termed flexures c and d) are given by

$$x_{c,i} = x_{f,i} + c_{f,i} L_{leg} \cos(\alpha_i) + c_{f,i}(w_b - c_{f,i} w_{sa}) \cos(\theta_i) + c_{f,i} L_b \sin(\theta_i)$$
$$y_{c,i} = y_{f,i} + L_{leg} \sin(\alpha_i) + (w_b - c_{f,i} w_{sa}) \sin(\theta_i) - L_b \cos(\theta_i) \tag{A.3}$$

and

$$x_{d,i} = x_{f,i} + c_{f,i} L_{leg} \cos(\alpha_i) + c_{f,i}(w_b + c_{f,i} w_{sa}) \cos(\theta_i) + c_{f,i} L_b \sin(\theta_i)$$
$$y_{d,i} = y_{f,i} + L_{leg} \sin(\alpha_i) + (w_b + c_{f,i} w_{sa}) \sin(\theta_i) - L_b \cos(\theta_i) \tag{A.4}$$

The coordinates given in Eq. A1 - A4 serve as the ends of the two sarrus linkages between each segment, so the square of the length of the sarrus linkages can be calculated as

$$S_{ac,i} = (x_{c,i} - x_{a,i+1})^2 + (y_{c,i} - y_{a,i+1})^2$$
$$S_{bd,i} = (x_{d,i} - x_{b,i+1})^2 + (y_{d,i} - y_{b,i+1})^2 \tag{A.5}$$

Where $S_{ac,i}$ is the sarrus linkage between flexures a and c posterior to segment i, and $S_{bd,i}$ is the sarrus linkage between flexures b and d posterior to segment i. while the respective sarrus linkage deflections are

$$ls_{ac,i} = \sqrt{S_{ac,i}} - l_{eq}$$
$$ls_{bd,i} = \sqrt{S_{bd,i}} - l_{eq} \tag{A.6}$$

with l_{eq} being the equilibrium sarrus linkage length.

The flexure locations in Eq. A1 - A4 can also be used to calculate the bending angles of the four rotational flexures between each segment

$$\gamma_{pac,i} = c_{f,i}\theta_i - asin\left(\frac{x_{a,i+1} - x_{c,i}}{\sqrt{S_{ac,i}}}\right)$$
$$\gamma_{pbd,i} = c_{f,i}\theta_i - asin\left(\frac{x_{b,i+1} - x_{d,i}}{\sqrt{S_{bd,i}}}\right)$$
$$\gamma_{aac,i+1} = c_{f,i+1}\theta_{i+1} + asin\left(\frac{x_{c,i} - x_{a,i+1}}{\sqrt{S_{ac,i}}}\right)$$
$$\gamma_{abd,i+1} = c_{f,i+1}\theta_{i+1} + asin\left(\frac{x_{d,i} - x_{b,i+1}}{\sqrt{S_{bd,i}}}\right) \tag{A.7}$$

A.2 Derivatives with respect to θ_i

The backbone torsional and linear springs are dependent on two of the state variables of the surrounding segments (θ and α), providing the coupling between segments. For the Euler-Lagrange method of formulating the dynamic equations, it is necessary to take the partial derivatives of the backbone spring deflections with respect to the state variables, which show up in the potential energy portion of the Lagrangian.

The y-coordinate derivatives of the backbone flexure locations (Eq. A1 - A4) with respect to θ_i are given by

$$\begin{aligned}
\frac{\delta y_{a,i}}{\delta \theta_i} &= (w_b - c_{f,i} w_{sa}) \cos(\theta_i) - L_b \sin(\theta_i) \\
\frac{\delta y_{b,i}}{\delta \theta_i} &= (w_b + c_{f,i} w_{sa}) \cos(\theta_i) - L_b \sin(\theta_i) \\
\frac{\delta y_{c,i}}{\delta \theta_i} &= (w_b - c_{f,i} w_{sa}) \cos(\theta_i) + L_b \sin(\theta_i) \\
\frac{\delta y_{d,i}}{\delta \theta_i} &= (w_b + c_{f,i} w_{sa}) \cos(\theta_i) + L_b \sin(\theta_i)
\end{aligned} \tag{A.8}$$

while the x-coordinate derivatives of the backbone flexure locations (Eq. A1 - A4) with respect to θ_i are

$$\begin{aligned}
\frac{\delta x_{a,i}}{\delta \theta_i} &= -c_{f,i}(w_b - c_{f,i} w_{sa}) \sin(\theta_i) - L_b \cos(\theta_i) \\
\frac{\delta x_{b,i}}{\delta \theta_i} &= -c_{f,i}(w_b + c_{f,i} w_{sa}) \sin(\theta_i) - L_b \cos(\theta_i) \\
\frac{\delta x_{c,i}}{\delta \theta_i} &= -c_{f,i}(w_b - c_{f,i} w_{sa}) \sin(\theta_i) + L_b \cos(\theta_i) \\
\frac{\delta x_{d,i}}{\delta \theta_i} &= -c_{f,i}(w_b + c_{f,i} w_{sa}) \sin(\theta_i) + L_b \cos(\theta_i)
\end{aligned} \tag{A.9}$$

These are used in the partial derivatives of the square of the sarrus linkage lengths with respect to θ_i, which are given according to

$$\begin{aligned}
\frac{\delta S_{ac,i-1}}{\delta \theta_i} &= -2(x_{c,i-1} - x_{a,i})\frac{\delta x_{a,i}}{\delta \theta_i} - 2(y_{c,i-1} - y_{a,i})\frac{\delta y_{a,i}}{\delta \theta_i} \\
\frac{\delta S_{bd,i-1}}{\delta \theta_i} &= -2(x_{d,i-1} - x_{b,i})\frac{\delta x_{b,i}}{\delta \theta_i} - 2(y_{d,i-1} - y_{b,i})\frac{\delta y_{b,i}}{\delta \theta_i} \\
\frac{\delta S_{ac,i}}{\delta \theta_i} &= 2(x_{c,i} - x_{a,i+1})\frac{\delta x_{c,i}}{\delta \theta_i} + 2(y_{c,i} - y_{a,i+1})\frac{\delta y_{c,i}}{\delta \theta_i} \\
\frac{\delta S_{bd,i}}{\delta \theta_i} &= 2(x_{d,i} - x_{b,i+1})\frac{\delta x_{d,i}}{\delta \theta_i} + 2(y_{d,i} - y_{b,i+1})\frac{\delta y_{d,i}}{\delta \theta_i}
\end{aligned} \tag{A.10}$$

where $S_{ac,i-1}$ and $S_{bd,i-1}$ are the square of the lengths of the sarrus linkages in front of segment i, and $S_{ac,i}$ and $S_{bd,i}$ are the square of the lengths of the sarrus linkages posterior to segment i. The partial derivatives of the sarrus linkage deflections with respect to θ_i are given by

$$\begin{aligned}
\frac{\delta l_{ac,i-1}}{\delta \theta_i} &= \frac{1}{2\sqrt{S_{ac,i-1}}}\frac{\delta S_{ac,i-1}}{\delta \theta_i} \\
\frac{\delta l_{bd,i-1}}{\delta \theta_i} &= \frac{1}{2\sqrt{S_{bd,i-1}}}\frac{\delta S_{bd,i-1}}{\delta \theta_i} \\
\frac{\delta l_{ac,i}}{\delta \theta_i} &= \frac{1}{2\sqrt{S_{ac,i}}}\frac{\delta S_{ac,i}}{\delta \theta_i} \\
\frac{\delta l_{bd,i}}{\delta \theta_i} &= \frac{1}{2\sqrt{S_{bd,i}}}\frac{\delta S_{bd,i}}{\delta \theta_i}
\end{aligned} \tag{A.11}$$

The four rotational flexures anterior to segment i and four rotational flexures posterior to segment i are dependent on θ_i. The derivatives of the rotational backbone flexures anterior to segment i with respect to θ_i are given by

$$\frac{\delta\gamma_{pac,i-1}}{\delta\theta_i} = \frac{-1}{\sqrt{1-\left(\frac{x_{a,i}-x_{c,i-1}}{\sqrt{S_{ac,i-1}}}\right)^2}}\left(\frac{x_{c,i-1}-x_{a,i}}{2S_{ac,i-1}^{3/2}}\frac{\delta S_{ac,i-1}}{\delta\theta_i}+\frac{1}{\sqrt{S_{ac,i-1}}}\frac{\delta x_{a,i}}{\delta\theta_i}\right)$$
$$\frac{\delta\gamma_{pbd,i-1}}{\delta\theta_i} = \frac{-1}{\sqrt{1-\left(\frac{x_{b,i}-x_{d,i-1}}{\sqrt{S_{bd,i-1}}}\right)^2}}\left(\frac{x_{d,i-1}-x_{b,i}}{2S_{bd,i-1}^{3/2}}\frac{\delta S_{bd,i-1}}{\delta\theta_i}+\frac{1}{\sqrt{S_{bd,i-1}}}\frac{\delta x_{b,i}}{\delta\theta_i}\right) \quad \text{(A.12)}$$

and

$$\begin{aligned}\frac{\delta\gamma_{aac,i}}{\delta\theta_i} = \quad & c_{f,i} \\ & + \frac{1}{\sqrt{1-\left(\frac{x_{c,i-1}-x_{a,i}}{\sqrt{S_{ac,i-1}}}\right)^2}}\left(\frac{x_{a,i}-x_{c,i-1}}{2S_{ac,i-1}^{3/2}}\frac{\delta S_{ac,i-1}}{\delta\theta_i}-\frac{1}{\sqrt{S_{ac,i-1}}}\frac{\delta x_{a,i}}{\delta\theta_i}\right) \\ \frac{\delta\gamma_{abd,i}}{\delta\theta_i} = \quad & c_{f,i} \\ & + \frac{1}{\sqrt{1-\left(\frac{x_{d,i-1}-x_{b,i}}{\sqrt{S_{bd,i-1}}}\right)^2}}\left(\frac{x_{b,i}-x_{d,i-1}}{2S_{bd,i-1}^{3/2}}\frac{\delta S_{bd,i-1}}{\delta\theta_i}-\frac{1}{\sqrt{S_{bd,i-1}}}\frac{\delta x_{b,i}}{\delta\theta_i}\right)\end{aligned} \quad \text{(A.13)}$$

and the derivatives of the rotational backbone flexure deflections posterior to segment i with respect to θ_i are given by

$$\frac{\delta\gamma_{pac,i}}{\delta\theta_i} = c_{f,i} - \frac{1}{\sqrt{1-\left(\frac{x_{a,i+1}-x_{c,i}}{\sqrt{S_{ac,i}}}\right)^2}}\left(\frac{x_{c,i}-x_{a,i+1}}{2S_{ac,i}^{3/2}}\frac{\delta S_{ac,i}}{\delta\theta_i} - \frac{1}{\sqrt{S_{ac,i}}}\frac{\delta x_{c,i}}{\delta\theta_i}\right)$$
$$\frac{\delta\gamma_{pbd,i}}{\delta\theta_i} = c_{f,i} - \frac{1}{\sqrt{1-\left(\frac{x_{b,i+1}-x_{d,i}}{\sqrt{S_{bd,i}}}\right)^2}}\left(\frac{x_{d,i}-x_{b,i+1}}{2S_{bd,i}^{3/2}}\frac{\delta S_{bd,i}}{\delta\theta_i} - \frac{1}{\sqrt{S_{bd,i}}}\frac{\delta x_{d,i}}{\delta\theta_i}\right) \quad \text{(A.14)}$$

and

$$\frac{\delta\gamma_{aac,i+1}}{\delta\theta_i} = \frac{1}{\sqrt{1-\left(\frac{x_{c,i}-x_{a,i+1}}{\sqrt{S_{ac,i}}}\right)^2}}\left(\frac{x_{a,i+1}-x_{c,i}}{2S_{ac,i}^{3/2}}\frac{\delta S_{ac,i}}{\delta\theta_i} + \frac{1}{\sqrt{S_{ac,i}}}\frac{\delta x_{c,i}}{\delta\theta_i}\right)$$
$$\frac{\delta\gamma_{abd,i+1}}{\delta\theta_i} = \frac{1}{\sqrt{1-\left(\frac{x_{d,i}-x_{b,i+1}}{\sqrt{S_{bd,i}}}\right)^2}}\left(\frac{x_{b,i+1}-x_{d,i}}{2S_{bd,i}^{3/2}}\frac{\delta S_{bd,i}}{\delta\theta_i} + \frac{1}{\sqrt{S_{bd,i}}}\frac{\delta x_{d,i}}{\delta\theta_i}\right) \quad \text{(A.15)}$$

A.3 Derivatives with respect to α_i

Similar to the procedure for θ_i in Sec. A.2, the derivatives of the backbone linear and rotational flexure deflections were taken with respect to α_i. The derivatives of the backbone flexure locations with respect to α_i are given by

$$\begin{aligned}
\frac{\delta y_{a,i}}{\delta \alpha_i} &= L_{leg}\cos(\alpha_i) \\
\frac{\delta y_{b,i}}{\delta \alpha_i} &= L_{leg}\cos(\alpha_i) \\
\frac{\delta y_{c,i}}{\delta \alpha_i} &= L_{leg}\cos(\alpha_i) \\
\frac{\delta y_{d,i}}{\delta \alpha_i} &= L_{leg}\cos(\alpha_i)
\end{aligned} \tag{A.16}$$

and

$$\begin{aligned}
\frac{\delta x_{a,i}}{\delta \alpha_i} &= -c_{f,i}L_{leg}\sin(\alpha_i) \\
\frac{\delta x_{b,i}}{\delta \alpha_i} &= -c_{f,i}L_{leg}\sin(\alpha_i) \\
\frac{\delta x_{c,i}}{\delta \alpha_i} &= -c_{f,i}L_{leg}\sin(\alpha_i) \\
\frac{\delta x_{d,i}}{\delta \alpha_i} &= -c_{f,i}L_{leg}\sin(\alpha_i)
\end{aligned} \tag{A.17}$$

The derivatives of the square of the sarrus linkage lengths are given by

$$\begin{aligned}
\frac{\delta S_{ac,i-1}}{\delta \alpha_i} &= -2(x_{c,i-1} - x_{a,i})\frac{\delta x_{a,i}}{\delta \alpha_i} - 2(y_{c,i-1} - y_{a,i})\frac{\delta y_{a,i}}{\delta \alpha_i} \\
\frac{\delta S_{bd,i-1}}{\delta \alpha_i} &= -2(x_{d,i-1} - x_{b,i})\frac{\delta x_{b,i}}{\delta \alpha_i} - 2(y_{d,i-1} - y_{b,i})\frac{\delta y_{b,i}}{\delta \alpha_i} \\
\frac{\delta S_{ac,i}}{\delta \alpha_i} &= 2(x_{c,i} - x_{a,i+1})\frac{\delta x_{c,i}}{\delta \alpha_i} + 2(y_{c,i} - y_{a,i+1})\frac{\delta y_{c,i}}{\delta \alpha_i} \\
\frac{\delta S_{bd,i}}{\delta \alpha_i} &= 2(x_{d,i} - x_{b,i+1})\frac{\delta x_{d,i}}{\delta \alpha_i} + 2(y_{d,i} - y_{b,i+1})\frac{\delta y_{d,i}}{\delta \alpha_i}
\end{aligned} \tag{A.18}$$

which are used to find the derivatives of the sarrus linkage deflection with respect to α_i according to

$$\begin{aligned}
\frac{\delta l_{ac,i-1}}{\delta \alpha_i} &= \frac{1}{2\sqrt{S_{ac,i-1}}} \frac{\delta S_{ac,i-1}}{\delta \alpha_i} \\
\frac{\delta l_{bd,i-1}}{\delta \alpha_i} &= \frac{1}{2\sqrt{S_{bd,i-1}}} \frac{\delta S_{bd,i-1}}{\delta \alpha_i} \\
\frac{\delta l_{ac,i}}{\delta \alpha_i} &= \frac{1}{2\sqrt{S_{ac,i}}} \frac{\delta S_{ac,i}}{\delta \alpha_i} \\
\frac{\delta l_{bd,i}}{\delta \alpha_i} &= \frac{1}{2\sqrt{S_{bd,i}}} \frac{\delta S_{bd,i}}{\delta \alpha_i}
\end{aligned} \tag{A.19}$$

Similarly, the derivatives of the rotational backbone flexure deflections with respect to α_i are given by the following

$$\begin{aligned}
\frac{\delta \gamma_{pac,i-1}}{\delta \alpha_i} &= \frac{-1}{\sqrt{1 - \left(\frac{x_{a,i} - x_{c,i-1}}{\sqrt{S_{ac,i-1}}} \right)^2}} \left(\frac{x_{c,i-1} - x_{a,i}}{2S_{ac,i-1}^{3/2}} \frac{\delta S_{ac,i-1}}{\delta \alpha_i} + \frac{1}{\sqrt{S_{ac,i-1}}} \frac{\delta x_{a,i}}{\delta \alpha_i} \right) \\
\frac{\delta \gamma_{pbd,i-1}}{\delta \alpha_i} &= \frac{-1}{\sqrt{1 - \left(\frac{x_{b,i} - x_{d,i-1}}{\sqrt{S_{bd,i-1}}} \right)^2}} \left(\frac{x_{d,i-1} - x_{b,i}}{2S_{bd,i-1}^{3/2}} \frac{\delta S_{bd,i-1}}{\delta \alpha_i} + \frac{1}{\sqrt{S_{bd,i-1}}} \frac{\delta x_{b,i}}{\delta \alpha_i} \right)
\end{aligned} \tag{A.20}$$

$$\frac{\delta\gamma_{aac,i}}{\delta\alpha_i} = \frac{1}{\sqrt{1-\left(\frac{x_{c,i-1}-x_{a,i}}{\sqrt{S_{ac,i-1}}}\right)^2}}\left(\frac{x_{a,i}-x_{c,i-1}}{2S_{ac,i-1}^{3/2}}\frac{\delta S_{ac,i-1}}{\delta\alpha_i} - \frac{1}{\sqrt{S_{ac,i-1}}}\frac{\delta x_{a,i}}{\delta\alpha_i}\right)$$

$$\frac{\delta\gamma_{abd,i}}{\delta\alpha_i} = \frac{1}{\sqrt{1-\left(\frac{x_{d,i-1}-x_{b,i}}{\sqrt{S_{bd,i-1}}}\right)^2}}\left(\frac{x_{b,i}-x_{d,i-1}}{2S_{bd,i-1}^{3/2}}\frac{\delta S_{bd,i-1}}{\delta\alpha_i} - \frac{1}{\sqrt{S_{bd,i-1}}}\frac{\delta x_{b,i}}{\delta\alpha_i}\right) \tag{A.21}$$

$$\frac{\delta\gamma_{pac,i}}{\delta\alpha_i} = \frac{1}{\sqrt{1-\left(\frac{x_{a,i+1}-x_{c,i}}{\sqrt{S_{ac,i}}}\right)^2}}\left(\frac{x_{c,i}-x_{a,i+1}}{2S_{ac,i}^{3/2}}\frac{\delta S_{ac,i}}{\delta\alpha_i} - \frac{1}{\sqrt{S_{ac,i}}}\frac{\delta x_{c,i}}{\delta\alpha_i}\right)$$

$$\frac{\delta\gamma_{pbd,i}}{\delta\alpha_i} = \frac{1}{\sqrt{1-\left(\frac{x_{b,i+1}-x_{d,i}}{\sqrt{S_{bd,i}}}\right)^2}}\left(\frac{x_{d,i}-x_{b,i+1}}{2S_{bd,i}^{3/2}}\frac{\delta S_{bd,i}}{\delta\alpha_i} - \frac{1}{\sqrt{S_{bd,i}}}\frac{\delta x_{d,i}}{\delta\alpha_i}\right) \tag{A.22}$$

$$\frac{\delta\gamma_{aac,i+1}}{\delta\alpha_i} = \frac{1}{\sqrt{1-\left(\frac{x_{c,i}-x_{a,i+1}}{\sqrt{S_{ac,i}}}\right)^2}}\left(\frac{x_{a,i+1}-x_{c,i}}{2S_{ac,i}^{3/2}}\frac{\delta S_{ac,i}}{\delta\alpha_i} + \frac{1}{\sqrt{S_{ac,i}}}\frac{\delta x_{a,i}}{\delta\alpha_i}\right)$$

$$\frac{\delta\gamma_{abd,i+1}}{\delta\alpha_i} = \frac{1}{\sqrt{1-\left(\frac{x_{d,i}-x_{b,i+1}}{\sqrt{S_{bd,i}}}\right)^2}}\left(\frac{x_{b,i+1}-x_{d,i}}{2S_{bd,i}^{3/2}}\frac{\delta S_{bd,i}}{\delta\alpha_i} + \frac{1}{\sqrt{S_{bd,i}}}\frac{\delta x_{b,i}}{\delta\alpha_i}\right) \tag{A.23}$$

A.4 Derivatives of the Lagrangian and work transfer

As discussed in Chapter 3, the Euler-Lagrange method was used to formulate the equations of motion for the millirobot. The Lagrangian, L, is given by

$$\begin{aligned} L = \quad & \sum_{i=1}^{n} (\frac{1}{2}(I_{cm} + mw_b^2){\dot{\theta}_i}^2 + \frac{1}{2}mL_{leg}^2{\dot{\alpha}_i}^2 + mw_b L_{leg}\dot{\alpha}_i\dot{\theta}_i \cos(\theta_i - \alpha_i) \\ & -\frac{1}{2}k_a\frac{1}{T_h^2}(\alpha_i - \theta_i)^2) - \frac{1}{2}\sum_{i=1}^{n-1}\left(k_l({\Delta l_{ac,i}}^2 + {\Delta l_{bd,i}}^2)\right) \\ & -\frac{1}{2}\sum_{i=1}^{n-1}\left(k_t(\gamma_{a,i}^2 + \gamma_{b,i}^2 + \gamma_{c,i}^2 + \gamma_{d,i}^2)\right) \end{aligned} \tag{A.24}$$

where the first three terms are a result of the segment kinetic energy, the fourth term is the actuator potential energy, and the last two terms are the sum of the linear and rotational backbone spring energies, respectively. In using the Euler-Lagrange formulation, it is necessary to take the partial derivative of L with respect to each of the state variables for a single segment: θ_i, α_i, $\dot{\theta}_i$, and $\dot{\alpha}_i$. I_{cm} and m are the segment inertia about the COM and segment mass, respectively. These partial derivatives are given by the following

$$\begin{aligned}\frac{\delta L}{\delta \theta_i} = \quad & -mw_b L_{leg}\dot{\theta}_i\dot{\alpha}_i \sin(\theta_i - \alpha_i) - k_l ls_{ac,i-1}\frac{\delta l_{ac,i-1}}{\delta \theta_i} - k_l ls_{bd,i-1}\frac{\delta l_{bd,i-1}}{\delta \theta_i} \\ & -k_t\gamma_{aac,i}\frac{\delta \gamma_{aac,i}}{\delta \theta_i} - k_t\gamma_{abd,i}\frac{\delta \gamma_{abd,i}}{\delta \theta_i} - k_t\gamma_{pac,i-1}\frac{\delta \gamma_{pac,i-1}}{\delta \theta_i} \\ & -k_t\gamma_{pbd,i-1}\frac{\delta \gamma_{pbd,i-1}}{\delta \theta_i} - k_l ls_{ac,i}\frac{\delta l_{ac,i}}{\delta \theta_i} - k_l ls_{bd,i}\frac{\delta l_{bd,i}}{\delta \theta_i} \\ & -k_t\gamma_{aac,i+1}\frac{\delta \gamma_{aac,i+1}}{\delta \theta_i} - k_t\gamma_{abd,i+1}\frac{\delta \gamma_{abd,i+1}}{\delta \theta_i} - k_t\gamma_{pac,i}\frac{\delta \gamma_{pac,i}}{\delta \theta_i} \\ & -k_t\gamma_{pbd,i}\frac{\delta \gamma_{pbd,i}}{\delta \theta_i} + k_a\frac{1}{T_h^2}(\alpha_i - \theta_i)\end{aligned} \tag{A.25}$$

$$\begin{aligned}\frac{\delta L}{\delta \alpha_i} = \quad & mw_b L_{leg}\dot{\theta}_i\dot{\alpha}_i \sin(\theta_i - \alpha_i) - k_l ls_{ac,i-1}\frac{\delta l_{ac,i-1}}{\delta \alpha_i} - k_l ls_{bd,i-1}\frac{\delta l_{bd,i-1}}{\delta \alpha_i} \\ & -k_t\gamma_{aac,i}\frac{\delta \gamma_{aac,i}}{\delta \alpha_i} - k_t\gamma_{abd,i}\frac{\delta \gamma_{abd,i}}{\delta \alpha_i} - k_t\gamma_{pac,i-1}\frac{\delta \gamma_{pac,i-1}}{\delta \alpha_i} \\ & -k_t\gamma_{pbd,i-1}\frac{\delta \gamma_{pbd,i-1}}{\delta \alpha_i} - k_l ls_{ac,i}\frac{\delta l_{ac,i}}{\delta \alpha_i} - k_l ls_{bd,i}\frac{\delta l_{bd,i}}{\delta \alpha_i} \\ & -k_t\gamma_{aac,i+1}\frac{\delta \gamma_{aac,i+1}}{\delta \alpha_i} - k_t\gamma_{abd,i+1}\frac{\delta \gamma_{abd,i+1}}{\delta \alpha_i} - k_t\gamma_{pac,i}\frac{\delta \gamma_{pac,i}}{\delta \alpha_i} \\ & -k_t\gamma_{pbd,i}\frac{\delta \gamma_{pbd,i}}{\delta \alpha_i} - k_a\frac{1}{T_h^2}(\alpha_i - \theta_i)\end{aligned} \tag{A.26}$$

$$\frac{\delta L}{\delta \dot{\theta}_i} = (I_{cm} + mw_b^2)\dot{\theta}_i + mw_b L_{leg}\dot{\alpha}_i \cos(\theta_i - \alpha_i) \tag{A.27}$$

$$\frac{\delta L}{\delta \dot{\alpha}_i} = mL_{leg}^2\dot{\alpha}_i + mw_b L_{leg}\dot{\theta}_i \cos(\theta_i - \alpha_i) \tag{A.28}$$

While the Lagrangian includes the conservative energy terms, the energy transfer with the environment is given by

$$W = \sum_{i=1}^{n} \tau_i(\alpha_i - \theta_i) - b_a \frac{1}{T_h^2}(\alpha_i - \theta_i)(\dot{\alpha}_i - \dot{\theta}_i) \tag{A.29}$$

where τ_i is the torque input from the actuators at the hip joint, and b_a is the actuator damping constant, mapped through the four-bar transmission with transmission ratio T_h. Taking the partial derivatives of the work transfer with respect to θ_i and α_i gives

$$\frac{\delta W}{\delta \theta_i} = -\tau_i + b_a \frac{1}{T_h^2}(\dot{\alpha}_i - \dot{\theta}_i) \tag{A.30}$$

and

$$\frac{\delta W}{\delta \alpha_i} = \tau_i - b_a \frac{1}{T_h^2}(\dot{\alpha}_i - \dot{\theta}_i) \tag{A.31}$$

A.5 Angular acceleration

The partial derivatives of the Lagrangian with respect to the state variables given in Sec. A.4 can be plugged into the Euler-Lagrange equation

$$\frac{\delta L}{\delta q_i} - \frac{d}{dt}\frac{\delta L}{\delta \dot{q}_i} = -\frac{\delta W}{\delta q_i} \tag{A.32}$$

This gives two coupled, second-order differential equations, which can be solved for

the angular acceleration of the segment

$$\begin{aligned}\ddot{\theta}_i = \quad & \frac{1}{I_{cm} + m w_b^2 (1 - \cos(\theta_i - \alpha_i)^2)} \Big(\frac{\delta L}{\delta \theta_i} - \tau_i \\ & + \frac{b_a}{T_h^2}(\dot{\theta}_i - \dot{\alpha}_i) + m w_b L_{leg} \dot{\alpha}_i (\dot{\theta}_i - \dot{\alpha}_i) \sin(\theta_i - \alpha_i) \\ & - \frac{w_b}{L_{leg}} \cos(\theta_i - \alpha_i) \Big(\frac{\delta L}{\delta \alpha_i} + \tau_i + \frac{b_a}{T_h^2}(\dot{\alpha}_i - \dot{\theta}_i) \Big) \\ & - m w_b^2 \dot{\theta}_i (\dot{\theta}_i - \dot{\alpha}_i) \sin(\theta_i - \alpha_i) \cos(\theta_i - \alpha_i) \Big) \end{aligned} \tag{A.33}$$

and the angular acceleration of the leg

$$\begin{aligned}\ddot{\alpha}_i = \quad & \frac{1}{m L_{leg}^2} \left(\frac{\delta L}{\delta \alpha_i} + \tau_i - \frac{b_a}{T_h^2}(\dot{\theta}_i - \dot{\alpha}_i) \right) + \frac{w_b}{L_{leg}} \dot{\theta}_i (\dot{\theta}_i - \dot{\alpha}_i) \sin(\theta_i - \alpha_i) \\ & - \frac{w_b}{L_{leg}} \ddot{\theta}_i \cos(\theta_i - \alpha_i) \end{aligned} \tag{A.34}$$

A.6 Stance changes

As described in Chapter 3, collisions during stance changes are modeled as inelastic and instantaneous as the previous swing foot changes to a stance foot by being pinned with respect to ground. This derivation is based on the method in [15]. Since the only external forces acting on the segment and leg system (System A in Fig. A.1) during stance change occur at the new stance foot, the angular momentum about the new stance foot is conserved. This is given according to

$$\frac{1}{3}w_b^2\dot{\theta}_{i,fin} + (x_i - x_{f,i})\dot{y}_{i,fin} + (y_i - y_{f,i})\dot{x}_{i,fin}$$
$$= \frac{1}{3}w_b^2\dot{\theta}_{i,init} + (x_i - x_{f,i})\dot{y}_{i,init} + (y_i - y_{f,i})\dot{x}_{i,init} \quad \text{(A.35)}$$

where $(x_{f,i}, y_{f,i})$ is the new stance foot position calculated based on kinematics, the subscript fin denotes values at the end of the previous step, and the subscript $init$ denotes the new values. Note that this equation is simplified due to the legs being massless and, therefore, not contributing to the angular momentum.

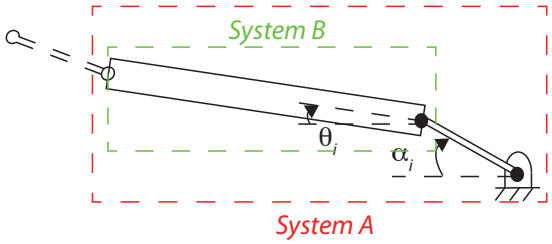

Figure A.1: During stance change, the angular momentum of System A is conserved about the new stance foot, while the angular momentum of System B is conserved about the new hip joint.

Additionally, by isolating the segment (System B in Fig. A.1), the only external forces acting on the segment occur at the hip joint, so the angular momentum of the segment alone is conserved about the new hip joint, resulting in

$$\frac{1}{3}w_b^2\dot{\theta}_{i,fin} + (x_i - x_{s,i})\dot{y}_{i,fin} + (y_i - y_{s,i})\dot{x}_{i,fin}$$
$$= \frac{1}{3}w_b^2\dot{\theta}_{i,init} + (x_i - x_{s,i})\dot{y}_{i,init} + (y_i - y_{s,i})\dot{x}_{i,init} \quad \text{(A.36)}$$

By writing $\dot{x}_i$ and $\dot{y}_i$ in terms of the state variables, Eq. A.35 and A.36 can be solved for the new body and leg angular velocities

$$\dot{\theta}_{i,init} = \frac{1}{\left(K_{ee} - J_{ee}\frac{H_{ee}}{G_{ee}}\right)}\left(D_{ee} - J_{ee}\frac{A_{ee}}{G_{ee}}\right) \tag{A.37}$$

and

$$\dot{\alpha}_{i,init} = \frac{A_{ee}}{G_{ee}} - \frac{H_{ee}}{G_{ee}}\dot{\theta}_{i,init} \tag{A.38}$$

where

$$\begin{aligned}
A_{ee} &= \frac{1}{3}w_b^2\dot{\theta}_{i,fin} + (x_{i,fin} - x_{f,i})\dot{y}_{i,fin} + (y_{i,fin} - y_{f,i})\dot{x}_{i,fin} \\
B_{ee} &= x_{i,init} - x_{f,i} \\
C_{ee} &= y_{i,init} - y_{f,i} \\
D_{ee} &= \frac{1}{3}w_b^2\dot{\theta}_{i,fin} + (x_{i,fin} - x_{s,i})\dot{y}_{i,fin} + (y_{i,fin} - y_{s,i})\dot{x}_{i,fin} \\
E_{ee} &= x_{i,init} - x_{s,i} \\
F_{ee} &= y_{i,init} - y_{s,i} \\
G_{ee} &= B_{ee}L_{leg}\cos(\alpha_{i,fin}) - c_{f,i}C_{ee}L_{leg}\sin(\alpha_{i,fin}) \\
H_{ee} &= B_{ee}w_b\cos(\theta_{i,fin}) - c_{f,i}C_{ee}w_b\sin(\theta_{i,fin}) + \frac{1}{3}w_b^2 \\
J_{ee} &= E_{ee}L_{leg}\cos(\alpha_{i,fin}) - c_{f,i}F_{ee}L_{leg}\sin(\alpha_{i,fin}) \\
K_{ee} &= E_{ee}w_b\cos(\theta_{i,fin}) - c_{f,i}F_{ee}w_b\sin(\theta_{i,fin}) + \frac{1}{3}w_b^2
\end{aligned} \tag{A.39}$$